Giant magnetoresistance effects in granular systems with gel matrices

Dissertation

Judith Meyer

Universität Bielefeld

Department of Physics

Thin Films and Physics of Nanostructures

Declaration

I hereby confirm that I wrote this thesis by myself and used none but the indicated resources.

Bielefeld, November 2013

(Judith Meyer)

Reviewers

Prof. Dr. Andreas Hütten

Prof. Dr. Thomas Huser

Contents

Publications and conferences

Publications

2013 J. Meyer, T. Rempel, M. Schäfers, F. Wittbracht, C. Müller, A. V. Patel and A. Hütten, Giant magnetoresistance effects in gel-like matrices, *Smart Mater. Struct.*, volume 22(2), pp. 025032

2013 A. Regtmeier, J. Meyer, N. Mill, M. Peter, A. Weddemann, J. Mattay and A. Hütten, Influence of nanoparticular impurities on the magnetic anisotropy of self-assembled magnetic Co-nanoparticles, *J. Magn. Magn. Mater.*, volume 326, pp. 112-115

2013 A. Weddemann, J. Meyer, A. Regtmeier, I. Janzen, D. Akemeier and A. Hütten, Hydrogen-plasma-induced magnetocrystalline anisotropy ordering in self-assembled magnetic nanoparticle monolayers. *Beilstein J. Nanotechnol.*, volume 4, pp. 164-172

2013 A. Weddemann, J. Meyer and A. Hütten, Numerical Study of Nanoscaled Granular Giant Magnetoresistance Sensors for the Limit Case of Dipolar Coupled Nanoparticles. *JBAP*, volume 2(2), pp. 60-67

2013 J. Meyer, M. Schäfers, T. Rempel and A. Hütten, AC-granular magnetoresistance effects in systems with organic matrices, *Nanotech 2013 Conference Proceedings*, CRC Press, volume 1, pp. 669

2013 C. Wang et al., Heusler nanocrystals for spintronics, magnetic shape memory alloys, and thermoelectrics, submitted to *JVST B*

2013 B. Eickenberg, J. Meyer, L. Helmich, D. Kappe, A. Auge, A. Weddemann, F. Wittbracht and A. Hütten. Lab-on-a-Chip Magneto-Immunoassays: How to Ensure Contact between Superparamagnetic Beads and the Sensor Surface, *Biosensors*, volume 3, pp. 327-340

Oral presentations

2012 J. Meyer, M. Schäfers and A. Hütten, *Giant Magnetoresistance Effects in jelly-like Structures*, DPG Spring Meeting, Berlin

2012 J. Meyer, M. Schäfers, F. Wittbracht and A. Hütten, *Giant Magnetoresistance Effects in Gel Structures*, Intermag Conference, Vancouver

2013 J. Meyer, M. Schäfers, T. Rempel and A. Hütten, *Giant Magnetoresistance Effects in Organic Matrices*, Fifth Seeheim Conference on Magnetism 2013, Frankfurt

Poster presentations

2013 J. Meyer, M. Schäfers, T. Rempel and A. Hütten, *Granular GMR effects in systems with organic matrix*, 526. WE-Heraeus-Seminar on Functional Magnetic Nanomembranes, Bad Honnef

2013 J. Meyer, M. Schäfers, T. Rempel and A. Hütten, *Granular GMR effects in systems with organic matrix*, DPG Spring Meeting, Regensburg

2013 J. Meyer, M. Schäfers, T. Rempel and A. Hütten, *Granular GMR effects in systems with organic matrix*, Nanotech Conference, Washington, DC

1 Introduction

The giant magnetoresistance effect (GMR effect) was found in 1988 in a Fe/Cr/Fe stack by Grünberg et al. and independently from that by Fert et al. in a Fe/Cr multilayer system [1, 2]. For their discovery both were awarded the Nobel Prize in 2007. Although, this effect was originally studied in magnetic multilayer systems, it was also reported within granular systems in 1992 by several research groups that used samples consisting of magnetic particles embedded in a metallic matrix [3, 4]. Magnetic field sensors based on the GMR effect have found a wide range of application, e.g. in magnetic read heads that were first introduced in hard disks by *IBM* in 1997 [5]. They are also applicable in biosensor technology, where the magnetic stray fields of nanoparticles attached to macromolecular analytes such as DNA or proteins in solution, allow for their detection by a GMR device. So-called lab-on-a-chip devices even make it possible to carry out complete immuno assay procedures, i.e. the determination of an analyte concentration, on the area of a chip of only few cm^2 [6, 7]. Magnetoresistive sensors commonly employed for these uses, however, are prepared by sputtering or metallurgical procedures and require well controlled lithography steps. Altogether, this results in time-consuming manufacturing processes and increased production costs, which is why a more cost-effective alternative is preferable. In contrast to conventional granular systems, we have chosen non-magnetic conductive gels as innovative type of matrix for granular GMR systems. Those gels comprise types derived from seaweeds, a product which is cheap and abundant in supply. Moreover, the use of gel allows for the realization of a granular GMR sensor by printing technology without the employment of photo- or e-beam lithography. As a result the fabrication of such sensors could be realized more rapidly and less expensive compared to conventional devices. The mechanical flexibility and formability of the matrix material might additionally enlarge the fields of application.

The scope of this work is to investigate the possibility of gel matrices as an alternative to common matrices of granular GMR systems. A brief theoretical introduction into the underlying phenomena of magnetism and magnetoresistance effects is given in chapter 2. The properties of the particles and gels employed in this work as well as the sample preparation is described in chapter 3, while the experimental setups and methods are summarized in chapter 4. The first gels tested were hydrogels. The corresponding magneto-transport measurements for Co- as well as for Heusler-based nanoparticles are presented in chapter 5. The large effect amplitudes recorded at room temperature exceed by far the values known for conventional GMR systems and will guarantee high sensor sensitivity. Gels featur-

ing a liquid-solid transition provide the possibility to deliberately arrange particle superstructures within the sample (chapter 6). The influence of the latter on the GMR effect was examined. The conductance and transport mechanisms in gel have been investigated by IV characteristics and temperature dependent measurements as presented in chapter 7. Electrolysis effects occurring in the matrix when applying direct current negatively affect the voltage stability and could be suppressed by the use of alternating current (AC). Important progress in terms of reproducibility of the GMR effect height in the considered gel systems was thus attained by performing transport measurements with AC (chapter 8). The basic concepts behind a granular-gel sensor as an application of the gel systems and its realization are elucidated in chapter 9. Finally, an idea to experimentally determine the spin diffusion length in gel and the first steps of its realization are discussed. As it will enhance the understanding of the spin transport in gel, it is worth to be included into future work.

2 Magnetism and magnetoresistance effects

The source of material magnetism lies in permanent magnetic moments that originate from electrons in not fully occupied shells of the atoms, e.g. in the 3d shell in the case of the elements of the iron group or in the 4f shell in the case of rare earths [8]. The contribution of the weak momentum of the nucleus can generally be neglected. The magnetization $\boldsymbol{M}$ of a solid is the number of magnetic moments per volume V [8]:

$$\boldsymbol{M} = \sum_i \frac{\boldsymbol{m_i}}{V} \ . \tag{2.1}$$

The magnetic susceptibility χ is a measure of the magnetic response of a material exposed to an external magnetic field [9]. More precisely, χ is the proportionality constant between the magnetization and the applied magnetic field $\boldsymbol{H}$

$$\boldsymbol{M} = \chi \boldsymbol{H} \quad \rightarrow \quad \chi = \frac{\mathrm{d}\boldsymbol{M}}{\mathrm{d}\boldsymbol{H}} \ . \tag{2.2}$$

The dependency of the magnetic flux $\boldsymbol{B}$ on the magnetization and the magnetic field yields the magnetic permeability μ_r, a magnitude for the transmissibility of a substance for magnetic fields. It can be associated with the susceptibility as follows

$$\boldsymbol{B} = \mu_0 \mu_r \boldsymbol{H} = \mu_0 \left(\boldsymbol{H} + \boldsymbol{M}\right) = \mu_0 \left(\boldsymbol{H} + \chi \boldsymbol{H}\right) = \mu_0 (1 + \chi) \boldsymbol{H} \ , \tag{2.3}$$

where μ_0 is the vacuum permeability.

2.1 Types of magnetism

In general, material can be classified by its magnetic properties into weak magnetic material such as dia- and paramagnetic material and strong magnetic material such as ferromagnetic (fm)-, ferrimagnetic- and antiferromagnetic material. The following discussion is mainly based on [8–10].

2.1.1 Diamagnetism and paramagnetism

In the absence of an external magnetic field, dia- and paramagnetic materials exhibit zero magnetization. Diamagnetism is a property of all materials. Since the diamagnetic contribution to a material's response to a magnetic field, however, is always very small, it becomes negligible, if a material shows another form of magnetism. Diamagnetic materials have a susceptibility $\chi < 0$. When exposed to an inhomogenous magnetic field, they are expelled as induced magnetic fields tend to oppose the change which created them. Compared to the applied magnetic field, the magnetic field inside the material is reduced. Paramagnetic materials feature permanent magnetic moments. Subjected to an external magnetic field, they experience a magnetization proportional to the applied field. Paramagnets are attracted by inhomogenous magnetic fields and have a susceptibility $\chi > 0$.

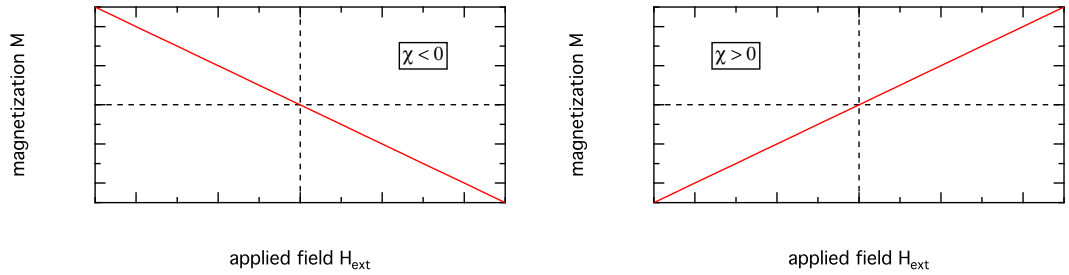

Figure 2.1: The magnetization M is shown in dependency of an external magnetic field H_{ext} for a diamagnet with susceptibility $\chi < 0$ (a) and a paramagnet with $\chi > 0$ (b).

2.1.2 Ferromagnetism

Strong magnetic materials feature so-called domains, ordered regions of uniform magnetization that are separated by boundaries called domain walls. An external magnetic field does alter the structure of domains, but not the value of the saturation magnetization inside. Due to this fact, a ferromagnet (FM) can appear non magnetic below the Curie temperature, if the magnetizations of the various domains are orientated in such a way that the specimen as a whole exhibits no net magnetization [11]. Below the Curie temperature (for FMs) and the Néel temperature (for antiferro- and ferrimagnets), spontaneous (zero-field) magnetization takes place. This long-range ordering below the characteristic temperatures originates from quantum-mechanical exchange interactions and disappears as a result of thermal agitation above the characteristic temperatures [8]. The carriers of magnetic moments are usually sketched out as magnetic dipoles. Figure 2.2 illustrates

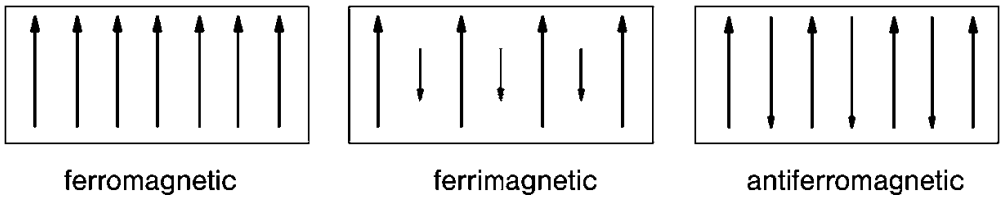

Figure 2.2: The arrangement of the magnetic dipoles below the respective ordering temperature are sketched out for the most common strong magnetic materials [10]. While dipoles in FMs are equal in size and aligned parallel to each other, equal moments are aligned antiparallel for antiferromagnets and moments unequal in size are aligned antiparallel to each other in the case of ferrimagnets.

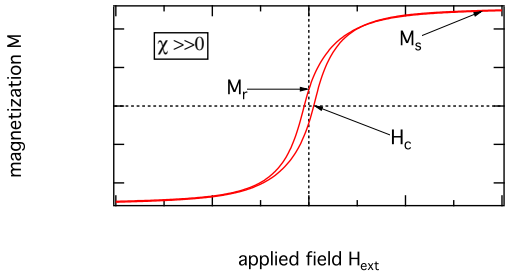

Figure 2.3: The figure shows a typical magnetization hysteresis curve of a FM with susceptibility $\chi \gg 0$. The data were experimentally taken for Co by AGM at room temperature. The saturation magnetization M_s, the remanence magnetization M_r and the coercive field H_c are marked.

the different magnetic orderings of the dipoles in FMs and other strong magnetic materials below their characteristic temperatures [10]. A FM below the Curie temperature features dipoles that are equal in size and aligned parallel to each other. Considered on larger length scales, the fm specimen converts into a multi-domain state in which each of the single domains is homogeneously magnetized. In antiferromagnets, moments of equal size are aligned antiparallel to each other, while several unequal moments are aligned in opposing orientation in ferrimagnets. In transition metals, ferromagnetism is based on unpaired electrons in partially filled 3d bands [9]. Typical FMs at room temperature are iron, cobalt or nickel. Figure 2.3 displays an exemplary magnetization curve of Co measured with an alternating gradient magnetometer (AGM) at room temperature. The fm susceptibility holds $\chi \gg 0$. FMs tend to keep their magnetization to some extent after being exposed to an external magnetic field, which is reflected in a hysteresis of the magnetization curve. The magnetization increases with applied magnetic field H_{ext} until all dipoles are aligned and the saturation magnetization M_s is reached. The fraction of the saturation magnetization that is retained after removing the driving magnetic field, is known as remanence magnetization M_r. A certain material-dependent magnetic field, denoted as coercive field H_c, in the opposite direction is necessary

to reduce the magnetization of the material to zero. When the magnetic field decreases further, the negative saturation magnetization is reached. Changing the direction of the external magnetic field once more, finally leads to a full hysteresis curve. The included area describes the work of the reversal of magnetization of the material.

2.1.3 Superparamagnetism

When the size of magnetic materials is reduced, the number of magnetic domain walls decreases, too. Below a critical size D_s the formation of those walls becomes energetically less favorable than the existence of the larger stray field of a single domain state [12,13]. Magnetic nanoparticles hence are mostly single-domain. For Co nanoparticles, e.g. D_s is known to be about 70 nm [14]. The particle size D_s features the highest coercive field (see figure 2.4). With shrinking particle size, the size of the coercive field decreases further which is associated with the reduction of the number of the exchange coupled spins.
The energy ΔE, which is necessary to change the magnetization of a single-domain particle, is proportional to the effective anisotropy constant K and the particle volume V [15]:

$$\Delta E \propto K \cdot V \ . \tag{2.4}$$

Below the critical size D_{sp}, the thermal energy $k_\mathrm{B}T$ is sufficient to provide this amount of energy and the particles become superparamagnetic. Their magnetic moments alternate between the easy axes. Just as for FMs, the magnetization curve exhibits a saturation magnetization, but no hysteresis. For the case of non-interacting particles with the volume distribution function $P(V)$, the magnetization process can be described as follows

$$M\left(H,T\right) = M_s \left(\int_0^\infty P(V) L \left(\frac{V \mu_0 m H}{k_\mathrm{B} T} \right) \mathrm{d}V \right) \ , \tag{2.5}$$

where L is the Langevin function

$$L\left(\frac{\mu_0 m(V) H}{k_\mathrm{B}T}\right) = \coth\left(\frac{\mu_0 m H}{k_\mathrm{B}T}\right) - \left(\frac{k_\mathrm{B}T}{\mu_0 m H}\right) \tag{2.6}$$

with μ_0 the vacuum permeability, m the magnetic moment, V the particle volume, H the applied magnetic field and $k_\mathrm{B}T$ the thermal energy [16].

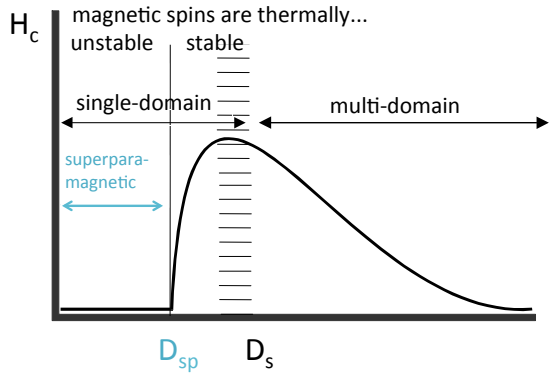

Figure 2.4: The intrinsic coercitivity is plotted as a function of size of the magnetic particles. (Figure modeled after [12]).

The probability for a thermally activated switching process of the magnetization is defined by

$$P(t_{meas}) = 1 - \exp\left(-\frac{t_{meas}}{\tau}\right), \tag{2.7}$$

where t_{meas} is the time of measurement and τ the thermal relaxation time. According to Néel and Brown it is given by [17]

$$\tau = \tau_0 \cdot \exp\left(\frac{\Delta E}{k_\mathrm{B}T}\right) = \tau_0 \cdot \exp\left(\frac{KV}{k_\mathrm{B}T}\right), \tag{2.8}$$

with energy barrier ΔE, anisotropy constant K and particle volume V. τ_0 is the characteristic time constant with $\tau_0 = \frac{1}{2\pi f_0}$ and f_0 the Lamor frequency. Generally, τ_0 is in the range of 10^{-12} to 10^{-10} s for nanoparticles [18]. Implying a characteristic measurement time of 100 s, for instance, the critical particle diameter D_{sp} for a spherical particle with uniaxial anisotropy can be calculated using equation 2.8 [9]

$$V = \frac{4\pi}{3}\left(\frac{D_{sp}}{2}\right)^3 = 25\,\frac{k_\mathrm{B}T}{K}. \tag{2.9}$$

2.2 Magnetic couplings

The interaction between magnetic particles plays a key role in the explanation of collective magnetism and forms the basis of spin-dependent transport phenomena. The stray-field coupling and the interlayer exchange coupling will be briefly presented.

2.2.1 Stray-field or dipole-dipole coupling

It is sufficient to model the particles with homogeneously magnetized spheres of radius R and magnetic moment $\boldsymbol{m}_{part}$ in many approaches investigating the interactions between small magnetic nanoparticles (compare figure 2.5). The stray-field created by a fm nanoparticle is given by the following dipolar expression

$$\boldsymbol{H}_{part}(\boldsymbol{r}) = \frac{1}{4\pi}\left(\frac{3\langle \boldsymbol{m}_{part}, \boldsymbol{r}\rangle \boldsymbol{r}}{r^5} - \frac{\boldsymbol{m}_{part}}{r^3}\right), \tag{2.10}$$

where $\langle \cdot, \cdot \rangle$ denotes the Euclidian inner product and $\boldsymbol{r}$ the distance vector from the center of the particle [19]. When a particle assembly is considered, the magnetic field acting on a single particle i is given by the superposition of the single stray fields H_{part} of the particles j in its vicinity and a possible contribution of an external magnetic field H_{ext} that can often be assumed homogenous

$$H^i = \sum_j H^i_{part,j} + H_{ext}. \tag{2.11}$$

As a result of this field, the particle i undergoes a force

$$\boldsymbol{F} = \nabla\left(\boldsymbol{m} \cdot \boldsymbol{H}^i\right) \tag{2.12}$$

that causes an alignment of the moments of additionally particles in the direction of the magnetic field lines of the first particle [20]. On that score, an arrangement of the particles in chains with identical direction of the single magnetic moments within the chain and an antiparallel alignment of neighboring particle chains is favored by the dipolar coupling.

2.2.2 Interlayer exchange coupling

The phenomenon of interlayer exchange coupling is observed between the magnetizations of two fm layers separated by a non-magnetic spacer layer and is the result of the direct exchange between the d electrons of the FM through the electron gas of the s electrons of the non-magnetic spacer. It was first described by Grünberg as an interaction that favored antiparallel alignment of the moments in successive magnetic layers of repeated Fe/Cr/Fe stacks [22]. Later, it actually was shown by Parkin et al. that the coupling strength of this interactions oscillates as a function of spacer layer thickness[1] [23]. The interlayer coupling energy per unit area can be expressed as

[1] i.e. an oscillation between parallel and antiparallel alignment of the magnetizations

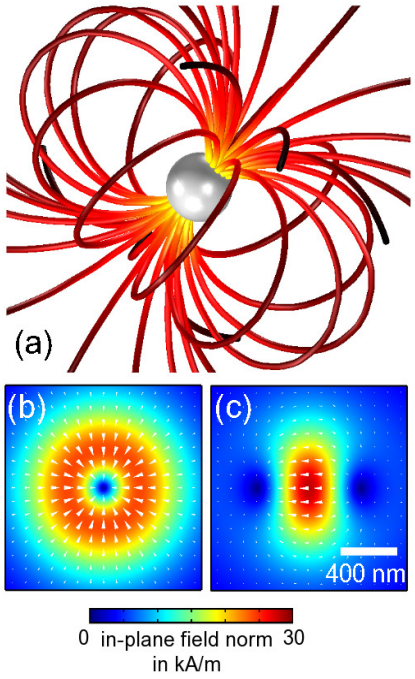

Figure 2.5: The stray field of a nanoparticle approximated by a homogeneously magnetized sphere is displayed (a). In (b) and (c) the streamline plots of the inplane components of the magnetization perpendicular and parallel to plane are shown. (Figure taken from [21].)

$$E = -J_1 \cos\theta - J_2 \cos^2\theta \tag{2.13}$$

with θ the angle between the magnetizations of the magnetic layers, J_1 the bilinear- and J_2 the biquadratic coupling constant. These coupling parameters determine the strength and type of the coupling depending on their magnitude and sign [24]. If the term J_1 dominates, the coupling is fm for a positive J_1 and antiferromagnetic for a negative J_1, respectively. A fm coupling favors a parallel alignment and an antiferromagnetic coupling an antiparallel alignment of the magnetization directions of the fm layers. In the same way, if the term with J_2 dominates and is negative, a 90°-coupling is obtained, where the magnetizations of the two fm layers are oriented perpendicular to each other.
Various models have been devised to describe the oscillatory coupling such as the free electron theory and the tight binding model [25, 26]. The free electron theory that yields a good approximation for the weak coupling limit is based on the RKKY (Ruderman-Kittel-Kasuya-Yosida) theory, but cannot explain the long period oscillations. These, however, are consistent with the tight binding model which includes the lattice structure in its calculation and emphasizes the importance of the roughness between layers for the coupling. The oscillatory coupling applies, for instance, to spin valves to emphasize the pinning effect of one fm layer.

2.3 Magnetoresistances

The phenomenon that some materials or systems of materials change their resistivity in response to an applied magnetic field, is known as magnetoresistance (MR). The fact that all conductors exhibit a weak MR effect emerges from the cyclic motion of electrons in a magnetic field. It was found in 1856 by William Thomson (Lord Kelvin) [27] and was later called ordinary magnetoresistance (OMR). Since the effect amplitude of OMR is too feeble to be used in sensors, it was not before the discovery of large magnetoresistive effects such as the anisotropic magnetoresistance (AMR) [28] that the development of solid-state magnetic sensors could replace more expensive wire-wound sensors in a variety of applications. Advances in thin film deposition technology have allowed researchers to create nanostructured multilayer devices with successively larger giant magnetoresistance (GMR) - [1, 2] and tunneling magnetoresistance (TMR) [29, 30], effects that have led to breakthroughs in electronic and computer technologies.

2.3.1 Anisotropic magnetoresistance (AMR)

AMR effects can be obtained in fm metals and alloys. In contrast to OMR, this effect is anisotropic, which means that $\Delta\rho_{\parallel}$ increases with field, whereas $\Delta\rho_T$ decreases with field. More precisely, the resistivity ρ depends on the angle Θ between the direction of the magnetization and the current density [31, 32]

$$\rho = \rho_0 + \Delta\rho_{AMR} \cdot \cos^2\Theta \ , \tag{2.14}$$

where ρ_0 is the resistivity for zero magnetic field and $\Delta\rho_{AMR}$ is the difference in the resistivity of the parallel and the perpendicular configuration. The physical reason of the AMR effect lies in the spin orbit coupling giving rise to an enhanced spin-flip scattering [33]. With the change of the direction of the magnetic field, the electron cloud about each nucleus deforms slightly leading to a change in electron orbit orientation with respect to the current direction. For field orientated transverse to the current, the electron orbits are in plane leading to a small cross-section for the scattering of the conduction electrons and hence a small resistance. However, for magnetic fields applied parallel to the current, the electronic orbits are situated perpendicular to the current which results in an increased scattering cross-section and thus to an increase in the resistance. Typical AMR ratios for transition metal FMs and their alloys range up to a few percent [31].

2.3.2 Giant magnetoresistance (GMR)

The GMR effect was originally discovered in 1988 in antiferromagnetically coupled multilayer systems consisting of thin layers of magnetic metals separated by a non-

magnetic metal layer [1, 2]. More precisely, much larger MR effect values were found for single crystalline (100)-oriented Fe/Cr/Fe sandwiches and (100)-oriented Fe/Cr multilayers than might have been accounted for the individual Fe layers. In contrast to the AMR effect, the GMR effect depends on the relative orientation of the magnetizations of the layers and not on the current direction. When an external magnetic field causes the magnetizations of the fm layers to switch from an antiparallel into a parallel orientation a change in the electrical resistance can be observed. The GMR ratio, briefly called GMR, is defined by the relative change of resistance from the parallel to the antiparallel direction of magnetization of the fm layers:

$$GMR = \frac{\Delta R}{R_{min}} = \frac{R_{max} - R_{min}}{R_{min}} \tag{2.15}$$

where R_{min} is the minimal resistance obtained in magnetic saturation and R_{max} the maximal resistance for zero external magnetic field. In this work, GMR is often simply denoted by $\Delta R/R$. Possible values of observed effect amplitudes reach up to 100 % [34]. Compared to AMR-effect amplitudes in FMs, for instance, this is about two orders of magnitude larger.

Phenomenological theory of GMR

The physical origin of GMR has been explained in terms of spin-dependent scattering of conduction electrons and can be understood within the Mott two-current model as a first approximation for GMR in multilayers [35]. The probability of spin-flip scattering processes in metals is normally very small compared to the probability of processes in which the spin is conserved. According to Mott, the electrical conduction in metals hence can be expressed as the sum of two largely independent conduction channels corresponding to the contributions of the spin-up and the spin-down electrons, respectively. Furthermore, Mott argues that in fm metals the scattering rates of the spin-up and spin-down electrons are different, depending on the magnetization of the scattering centers. More precisely, the band structure in a FM is exchange-split. This means that the density of states and hence the scattering rates as well as the resistances are not the same for electrons of different spin at the Fermi energy. Figure 2.6 illustrates the situation for a multilayer. If the spin of the conduction electrons is parallel to the magnetization of the fm layer, they pass through the structure almost without scattering, whereas electrons with spin antiparallel to the magnetization are strongly scattered. As conduction occurs in parallel for the two spin channels, the total resistance of the parallel-aligned magnetic layers is mainly determined by the highly-conductive spin-up electrons and appears to be low (compare figure 2.6). For the antiparallel-aligned layers, both the spin-up and spin-down electrons are scattered strongly within one of the fm layers resulting in a large total resistance of the multilayer.

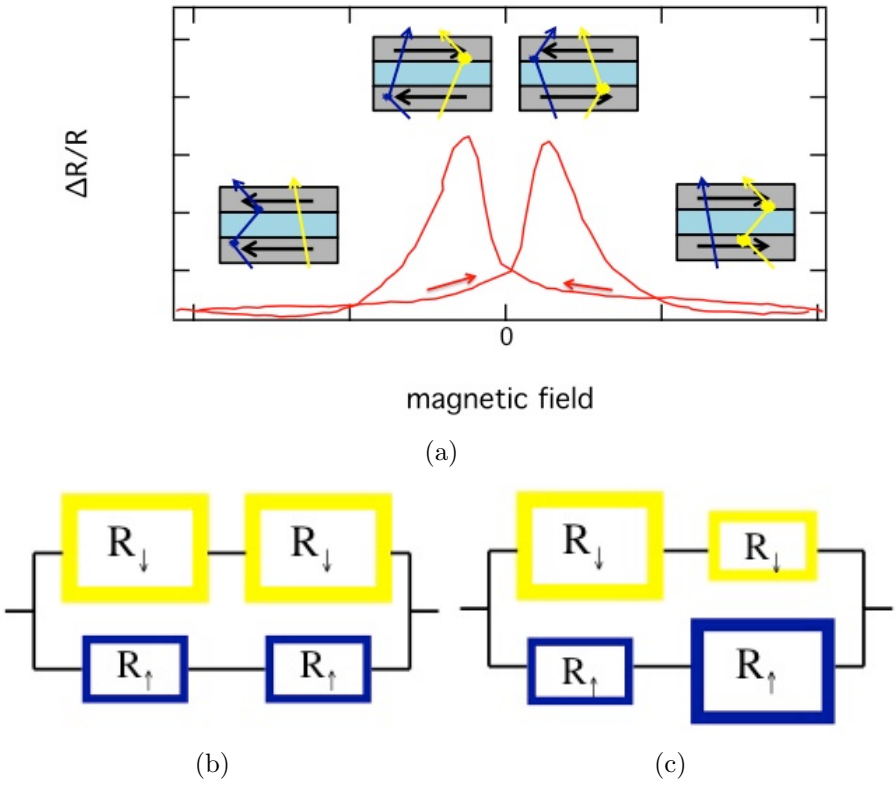

Figure 2.6: Subfigure (a) qualitatively displays a GMR measurement of a trilayer with two fm layers (grey) separated by a non-magnetic spacer layer (light blue). The red arrows indicate the direction of the curve progression under the changing external magnetic field. The black arrows give the directions of the magnetizations, the blue and yellow arrows the trajectories of the spin-up and spin-down electrons, respectively. Note that here spin-up means parallel alignment to the magnetization in right direction. Conduction electrons are strongly scattered when their spin is aligned antiparallel to the magnetization of the magnetic layer. A simple resistor network model illustrates the corresponding circuit for the parallel (b) and antiparallel (c) configuration of the fm layers. Each conduction channel is represented by a series connection of two resistances resulting from the spin-dependent scattering probability. The values of the resistances are symbolized by different sizes of the rectangles. (Sketches based on [36]).

Current-in-plane (CIP) and current-perpendicular-to-plane (CPP) GMR

A GMR device can work in two configurations referred to as current-in-plane (CIP) and current-perpendicular-to-plane (CPP), respectively (see figure 2.7). The CIP configuration, however, is the more convenient one due to resistivity measurements in CPP geometry are more sophisticated to realize. As the thickness of the GMR stack is usually orders of magnitude smaller than its length, the resistances to be measured are very small and, therefore, require special techniques for a precise measurement. The physical explanation of GMR in CIP geometry is different to

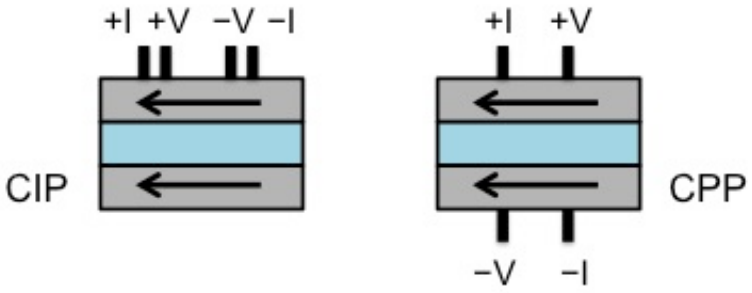

Figure 2.7: The two configurations in which a GMR device can work, namely current-in-plane (CIP) and current-perpendicular-to-plane (CPP), are illustrated.

that of GMR in CPP geometry [12]. Alternatively to the resistor model used above, the CPP-GMR device can be analyzed by means of the spin accumulation as stressed by the Valet-Fert model [37]. In the limit, in which the FMs are half-metallic, the first electrode supplies a spin polarized current of e.g. type spin-up, which generates a spin accumulation in the nonmagnetic spacer layer. The spin diffusion or spin relaxation refers to the distance, over which electrons remain spin polarized. For the case that the thickness of the middle layer is comparable with or smaller than the spin-diffusion length λ_s, the spin accumulation reaches the second FM. This FM acts as a spin filter and only spins of the required orientation - depending on the magnetization direction - can pass. For this reason, it is evident that λ_s is the critical length scale for a CPP-GMR device. For CIP geometry, however, where the current flows parallel to the layers, no spin accumulation is generated and the GMR effect rather arises from the different mobilities of the spin-up as well as spin-down electrons and the successive momentum scattering the conduction electrons undergo in the different magnetic layers. For magnetization directions parallel, one spin type is heavily scattered in both layers, whereas the other spin type experiences a high mobility. For antiparallel magnetization, on the other hand, neither spin type has a high mobility as both are scattered in one of the layers. Due to this explanation, it becomes clear that the relevant length scale for CIP GMR is not λ_s as for CPP GMR, but rather the mean free path.

Spin-diffusion lengths can significantly exceed the mean free path. Compared to CPP-GMR multilayers, CIP multilayers thus must use smaller spacers of 10 $\AA$ or less [12].

Granular GMR

In 1992, the GMR effect was independently reported within granular systems by several research groups that used samples based on magnetic particles embedded in metallic matrices [3,4]. Just as for multilayers, the Mott two-current model provides an explanation for the physical origin of the GMR effect in granular materials [38]. In granular systems, the maximal resistance $R_{\uparrow\uparrow}$ is given by the statistical distribution of the magnetic moments of the single granules. As illustrated in figure 2.8, this resistance decreases with increasing external magnetic field. When the magnetic moments of all granules are aligned, the resistance reaches its minimum $R_{\uparrow\uparrow}$. The GMR exhibited by granular systems can be understood as a mixture of CIP and CPP GMR for geometrical reasons [39]. Therefore, both characteristic length scales for these two phenomena are involved in granular GMR.

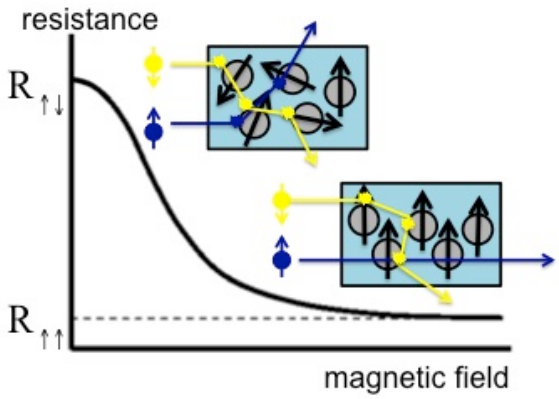

Figure 2.8: The resistance of a granular GMR system is plotted versus the external magnetic field. At zero field, the magnetic moments of the single granules are statistically distributed. Both spin-up and spin-down electrons are strongly scattered resulting in a high resistance $R_{\uparrow\downarrow}$. For a high field, however, the magnetic moments of all particles are aligned and the minimum resistance $R_{\uparrow\uparrow}$ is reached.

2.3.3 Tunneling magnetoresistance (TMR)

Spin-tunnel junctions consist of two fm electrodes that are separated by an electrical insulating barrier in the nanometer regime. Depending on the relative alignment

of the fm electrode magnetizations, large changes in the tunnel resistance can be measured (see figure 2.9) [30]. The discovery of TMR dates back to the work of Julliére in 1975 [40]. TMR effects generally are larger than effects of GMR devices. With R_P the resistance for parallel and R_{AP} the resistance for antiparallel alignment of the electrodes, the TMR ratio can be defined by [41]

$$TMR = \frac{R_{AP} - R_P}{R_P} \ . \tag{2.16}$$

Simplistically, the model of Julliére explains the TMR effect with an unequal distribution of spin-up- and spin-down-electron states in the magnetic metals due to the spin splitting at the Fermi level and a tunnel current that is proportional to the spin-state densities on each side of the tunnel barrier. Due to the spin polarization of the electrons at the Fermi level and under the assumption that the spin is conserved in the process of tunneling, the resistance can be considered as a parallel connection of two independent spin channels [42]. In the following, the electrons with spin parallel to the magnetization will be referred to as majority- and the electrons with spin antiparallel to the magnetization will be referred to as minority electrons. For a parallel orientation of the magnetizations of the two FMs, there are vacant states for both spin types at both sides of the barrier, few for the minority and many for the majority electrons. This means that the minority spins from one FM can tunnel to the minority spin states in the other FM and consequently for the majority spin electrons. A high tunnel current proportional to the spin-state densities flows:

$$I_p \propto n^{\uparrow}_{FM1} n^{\uparrow}_{FM2} + n^{\downarrow}_{FM1} n^{\downarrow}_{FM2} \ . \tag{2.17}$$

The resulting total resistance is smaller than in the case of an antiparallel magnetization, where there are sufficient vacant spin states for the majority, but not for the minority electrons. Only a weak tunnel current can be measured:

$$I_{ap} \propto n^{\uparrow}_{FM1} n^{\downarrow}_{FM2} + n^{\downarrow}_{FM1} n^{\uparrow}_{FM2} \ . \tag{2.18}$$

With P_1 and P_2 the spin polarizations of the two fm electrodes, it is also possible to express this ratio by

$$TMR = \frac{I_p - I_{ap}}{I_{ap}} = \frac{2P_1P_2}{1 - P_1P_2} \ . \tag{2.19}$$

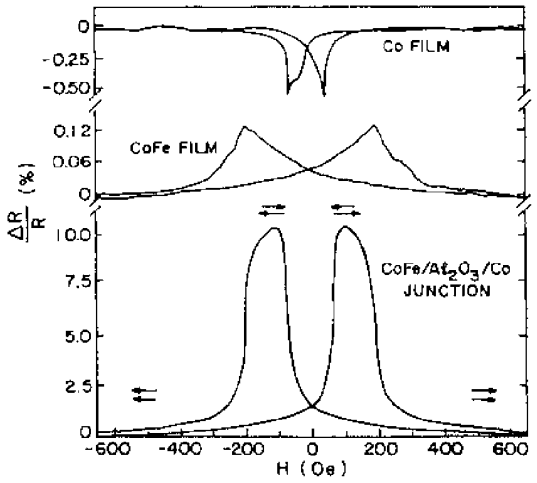

Figure 2.9: The tunnelling magnetoresistance of a $CoFe/Al_2O_3/Co$ trilayer, experimentally measured in plane at 295 K, is plotted as a function of magnetic field H. The arrows indicate the directions of magnetization in the two films. Furthermore, the variation of resistance in a CoFe and a Co film is given. (Figure taken from [30]).

TMR behavior has also been found in granular systems involving fm metal clusters in an insulating matrix, if the insulating barriers are low and the clusters numerous enough [43–47].

3 Properties of particles and gels

This chapter gives an overview of the properties and characteristics of the nanoparticles and gels employed in this work. Furthermore, the sample preparation is illustrated.

3.1 Particles

3.1.1 Co nanoparticles

The Co nanoparticles employed in this work are commercially available and were purchased from the company *TurboBeads* [48]. The particles are carbon coated and were prepared by a modified flame synthesis method [49, 50], in which the deposition of the carbon shell is achieved by adding acetylene to the nanoparticle-forming process. Figure 3.1 (a) displays a transmission-electron-microcopy (TEM) image of an individual Co nanoparticle. The single carbon layers of the shell with a total thickness of about 1 nm are visible. TEM was also used to determine the

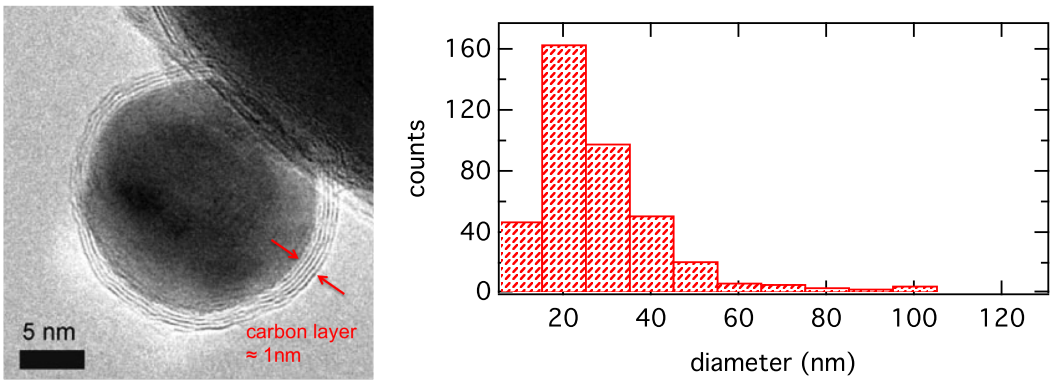

(a) (b)

Figure 3.1: A TEM image of a carbon coated Co nanoparticle is shown [50]. The single carbon layers of the shell are visible. The corresponding size distribution was obtained by TEM measurement (b).

size distribution of the nanoparticles (see figure 3.1). The particles with different diameters were counted from an image detail of few micrometers. The particle sizes are broadly distributed. A statistical analysis resulted in a mean particle

diameter of (17.9 ± 18.7) nm. AGM measurements at room temperature revealed a fm behavior with a coercive field of about 200 Oe (see figure 4.7).

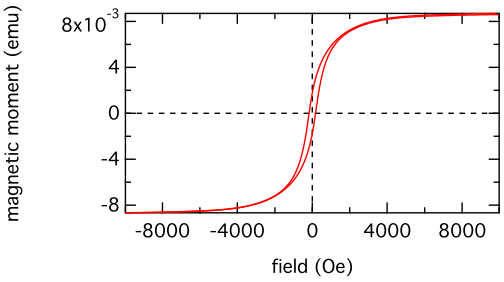

Figure 3.2: AGM measurements of the carbon coated Co nanoparticles were performed at room temperature. The coercive field is about 200 Oe.

3.1.2 Heusler-based nanoparticles

Heusler alloys, discovered in 1903 [51] refer to intermetallic compounds with the formula X_2YZ featuring a $L2_1$-crystal structure. X and Y normally are transition metals and Z is a main group element. The triumphant advance of Heusler compounds can mainly be attributed to their unique bandstructure enabling the realization of different physical properties such as ferromagnetism, semi- and superconductivity in one material class [52]. Though the combining elements are nonmagnetic, most of the Heusler compounds are fm. Besides, the majority of the Co_2YZ Heusler compounds with perfectly $L2_1$-ordered crystal structures are predicted as half metallic FMs. The concept of half metallic FMs implies a 100% spin polarization at the Fermi energy due to a finite density of states at the Fermi level in one and a gap in the other spin direction [53]. This fact makes them promising candidates for spintronic devices (compare equation 2.19) [52]. Among the various Heulser compound nanoparticles, Co-based Heusler particles (Co_2FeZ with $Z = Al, Si, Ga, Ge$) seem to be the most favorable types because of their high spin polarization, magnetization and Curie temperature [54, 55].
Recently, the successful synthesis of ternary Co_2FeGa Heusler nanoparticles from precursors was reported and their size-related structures and magnetic properties were analyzed [56–58]. The Heusler-based particles employed in this work are of type Co_2FeGa [59, 60]. The size distribution of the particles obtained by TEM revealed a mean diameter of (8.7 ± 0.2) nm (figure 3.3 (a)). AGM measurements at room temperature confirmed a fm and - due to the small hysteresis with an coercive field of about 150 Oe - soft magnetic behavior (see figure 3.3 (b)). The particles feature a carbon shell and were synthesized in the presence of silica supports by a modified impregnation-calcination method [58]. In this technique, silica spheres are added to the precursor salts dispersed in methanol. After the removal of the methanol by a rotary evaporator, the obtained solid is dried, grounded to a powder and annealed under H_2-atmosphere. In general, a well-ordered $L2_1$ or B2 structure is required for a high degree of spin polarization. Figure 3.4 displays the anomalous X-ray diffraction (XRD) data measured after the synthesis

of the Co_2FeGa nanoparticles for different excitation energies that were chosen close to the K-absorption edges of cobalt and iron [57]. The (111)- and (200)-superstructure reflections are evident and proof the $L2_1$ structure of the particles. The lattice parameter at room temperature was determined by Rietveld refinement to $a = 0.573\,\text{nm}$, which is slightly smaller than the value for polycrystalline bulk material [61]. This difference may be explained by increased intrinsic pressure in the nanoparticles caused by the comparably high ratio of surface to bulk atoms [61]. The anomalous XRD data additionally confirm a chemical purity and crystalline quality of the Heusler nanoparticles as can be concluded from the sharpness of the (200) reflection. Figure 3.4 displays a high resolution TEM image of a single 18 nm Co_2FeGa nanoparticle and the corresponding Fourier transformation. At the given resolution, the data agree with the results of the anomalous XRD measurements.

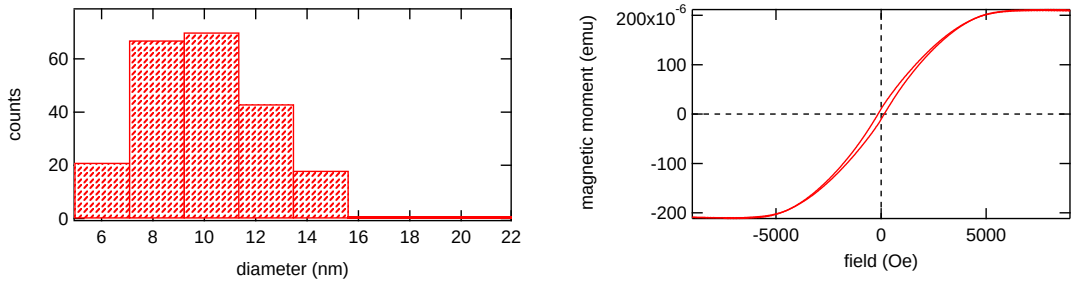

(a) (b)

Figure 3.3: Subfigure (a) gives the size distribution of the Heusler-based nanoparticles of type Co_2FeGa. A statistical analysis revealed a mean diameter of $(8.7 \pm 0.2)\,\text{nm}$. The corresponding AGM measurement at room temperature is shown in subfigure (b). The coercive field H_c is located at about 150 Oe.

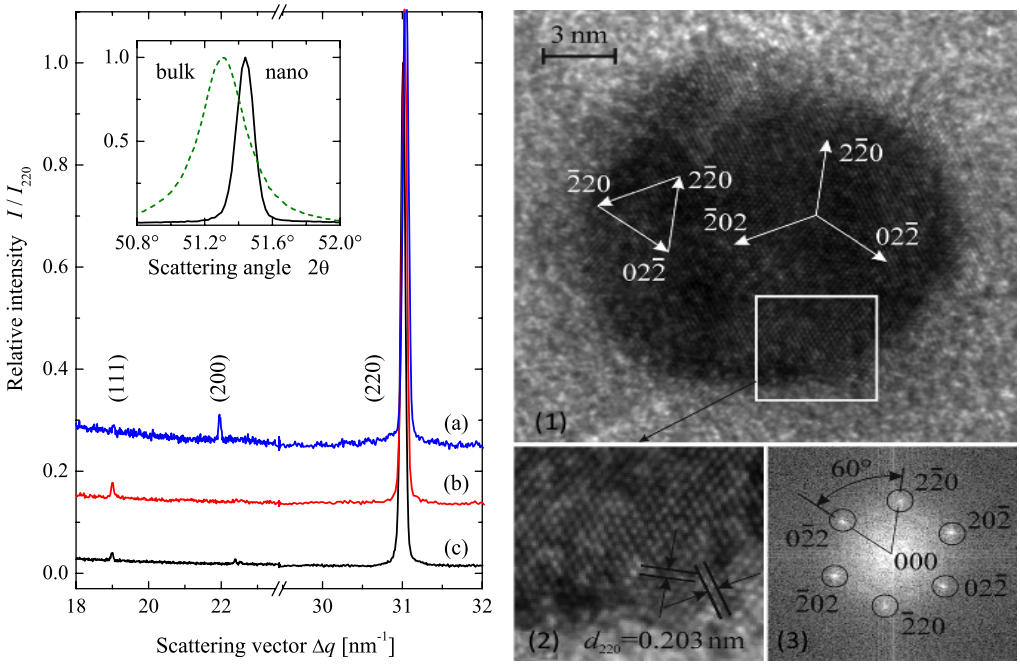

(a) (b)

Figure 3.4: The high resolution diffraction patterns of the Co_2FeGa nanoparticles (a) were taken by anomalous XRD at excitation energies close to the Co (a) or Fe (b) absorption K-edges using photon energies of 7.7077 keV or 7.112 keV, respectively, and the off resonant diffraction data (c) at hν = 7.05 keV [57]. The inset shows the (2 2 0) reflections taken from bulk material compared to the nanoparticles (7.05 keV). The broadening of the bulk reflection is a result of the sample preparation [57]. A high resolution image of the Co_2FeGa nanoparticles was taken by TEM (b). A particle with a diameter of 18 nm (1), a part of the nanoparticle on enlarged scale (2) and the Fourier transform of the image (3) are shown [57].

3.2 Gels

Even though gels [1] had already been studied in the 19th century [62], there is no precise and generally accepted definition due to the broad variety of existing gel structures and their wide range of characteristics. The term gel refers to elastic and cohesive structures, which are produced by a specific reaction called sol-gel transition. The gel-forming molecules are arranged in three dimensional netlike structures. In general, a distinction is made between main valence gels (e.g. silicon gels) and secondary valence gels (e.g. agarose gel) [63]. While the network of the main valence gels is based on dipole-dipole interaction, hydrogen bonds or Coulomb forces, it is based on covalent bonds in the case of secondary valence gels [63]. The cavities inbetween the network can be filled with a liquid as in the case of a Lyogel (e.g. hydrogel in case of water) or with gas as in the case of a Xerogel. Physical and chemical properties of the gel are largely influenced by the geometry of the net and the properties of the dispersed phase.

3.2.1 Silicon gel

Starting from a colloidal solution (sol) the sol-gel chemical process promotes the gel formation through the hydrolysis and condensation reactions of inorganic alkoxide monomers [64]. Most popular precursors synthesizing these colloids are metal alkoxides as they react readily with water. More precisely, alkoxysilanes, such as tetramethoxysilane (TMOS) and tetraethoxysilane (TEOS) are the most widely used metal precursors. The silica-based gels employed in this work, which for ease of reference will be referred to as matrix A in the following, were provided by the *FH Bielefeld* [65]. The gels were prepared using a tetra(n-propylamine)silane (Si-N) precursor [66, 67]. Its sol-gel process is sketched out in figure 3.5.

[1] short form derived from gelatine

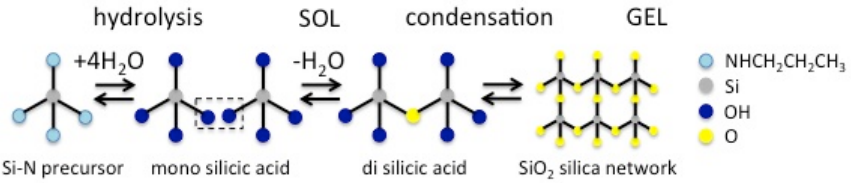

Figure 3.5: The sol-gel process of the tetra(n-propylamine)silane $Si(NHPr_4)$ precursor is modeled after [67]. In contrast to conventional sol-gel processes with silicon alkoxides, the hydrolysis and condensation for this precursor takes place at room temperature and does neither need organic solvents nor catalysts such as acid and bases [66, 68].

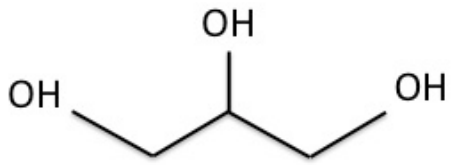

Figure 3.6: The chemical structure of glycerin is sketched out.

glycerin (%)	0	20	40	50	60	67	80	90
viscosity η (10^{-3}Pas) @ 20°C	1.005	1.76	3.72	6.00	10.8	17.7	60.1	219

Table 3.1: The viscosities η of water-glycerin mixtures for different concentrations of glycerin are given [70].

3.2.2 Electrode gel

The electrode gel (denoted as matrix B in the following) used in this work is a highly conductive electrode gel (*CV-Tronic Elektroden-Gel*) customary in electromedical applications and monitoring devices. Electrode gels refer to hydrogels composed of cross-linked polymers and are commercially available from a varied range of suppliers. According to the manufacturer, ingredients are the following: Aqua, glycerin, carbomer, sodium hydroxide, elektrolyt, propylene glycol, benzyl alcohol, methylchloroisothiazolinone, methylisothiazolinone [69].

3.2.3 Water-glycerin mixture

Glycerin is a simple polyol compound (figure 3.6), which is soluble in water at every concentration due to its three hydroxyl groups. Table 3.1 gives the viscosity for water-glycerin mixtures at different glycerin concentrations. A 2:1 mixture of glycerin and water (matrix C) was prepared to obtain a gel-like matrix at suitable viscosity.

3.2.4 Alginate gel

Alginates refer to the salts of alginic acid, which can be found as intracellular material in brown algae [71] and consist of an insoluble mixture of calcium, magnesium, sodium and potassium salts [72]. It is composed of two distinct types of monosaccharides, namely, 1,4-linked β-D-mannuronic acid (M) and 1, 4-linked α-L-guluronic acid (G) (figure 3.7). The ratio between those two acids varies not only from source to source, but also within a single alga. The monosaccharides are

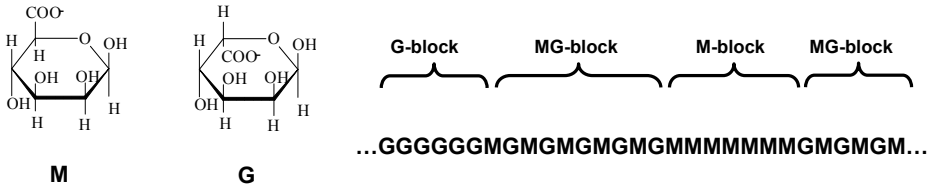

Figure 3.7: The chemical structure of alginates is illustrated [74]. Alginates are composed of 1,4-linked β-D-mannuronic acid (M) and 1, 4-linked α-L-guluronic acid (G). The relative amount of both polymers as well as their sequential arrangement varies widely.

distributed along the polymer in a pattern of blocks where homopolymeric blocks of G type (G-blocks), homopolymeric blocks of M type (M- blocks) and blocks with alternating sequence of M and G units (MG-blocks) can co-exist (figure 3.7). In the presence of divalent ions such as calcium (Ca^{2+}), alginate is a cold setting gelling agent with a gel forming process that takes place rapidly and under mild (physiological) conditions [73]. When alginate e.g. is added to a solution of calcium chloride, the sodium ions (Na^{+}) are exchanged with the calcium ions (Ca^{2+}) according to the following reaction

$$2\mathrm{Na(alginate)} + \mathrm{CaCl_2} \rightarrow 2\mathrm{NaCl} + \mathrm{Ca(alginate)}. \tag{3.1}$$

This results in a cross linking of the polymers. Once polymerized, this gel cannot be re-liquified. The generated hydrogels (matrix D) are thermally stable over a range of roughly $0 - 100°\mathrm{C}$. However, even at room temperature the alginic acid in the gels depolymerizes at some time leading to a loss in viscosity. If refrigerated ($5°\mathrm{C}$), alginate gels are stable for about one year.

3.2.5 Agarose gel

Agarose is extracted from seaweeds and represents the basic gel-forming component of commercial agar [71]. It is a linear polysaccharide with repeating agarbiose units consisting of alternating residues of 1,3-linked β-D-galactose and 1,4-linked 3,6-anhydro-α-L-galactose (L-galactose anhydride) (see figure 3.8 (b)). Agarose gel (matrix E) is prepared by boiling up agarose in a buffer. The most common type is the TAE buffer, a solution containing a mixture of tris base, acetic acid and ethylenediaminetetraacetic acid (EDTA). Boiling and subsequent cool down below the gelling temperature leads to interweaving of the long unbranched agarose molecules and the polymerization to a gel matrix (see figure 3.9). The reticule of agarose gel thereby is formed by hydrogen bonds, which make this biogel thermoreversible, i.e. within a limited temperature interval it exhibits a reversible transi-

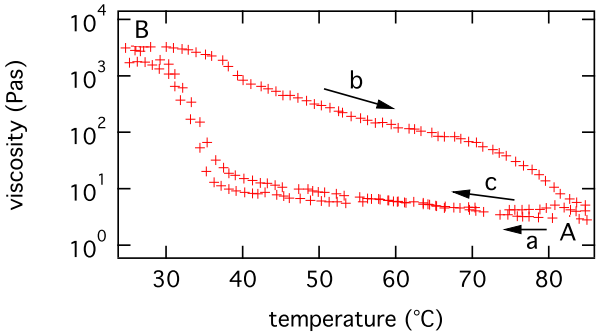

(a)

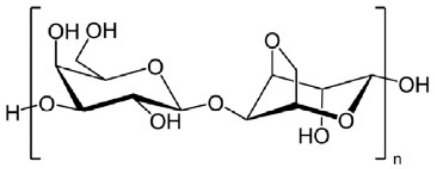

(b)

Figure 3.8: The viscosity of a 2 %-agarose solution in dependency of the temperature is given (a) (plot taken reproduced after [75]). Starting from the initial temperature of about 85°C (A), the agarose solution is cooled down along path a. In the region of the transition from the liquid to the solid gel state (36 – 31°C) the viscosity significantly rises. When the gel is heated up again, the transition from the solid gel to the liquid state runs along path b. A third sweep (c), which starts another hysteresis loop and ends at B, is indicated. The constitutional formula of agarose is displayed (b) [76]. It is a polysaccharide consisting of units of 1,3-linked β-D-galactose and 1,4-linked 3,6-anhydro-α-L-galactose (L-galactose anhydride).

tion from a quasi solid to a fluid. More than any other hydrocolloid, agarose gel exhibits a high hysteresis, i.e. a difference between melting and gelling temperatures (see figure 3.8). In particular, the gelling temperature ranges from 32°C to 45°C, while the range of the melting temperature normally is from 80°C to 95°C. These can be modified, however, by the concentration of agarose when preparing products for specific uses (see table 3.2). The standard agarose gel employed in this work is a 2 %-agarose gel prepared with a TAE buffer.

concentration	T_{gel} (°C)	T_{melt} (°C)
2 %	33-36	73
3 %	34-36	78
4 %	35-36	80
5 %	37-39	79

Table 3.2: The gelling (T_{gel}) and melting temperatures (T_{melt}) of agarose are given in dependency of the agarose concentration [75].

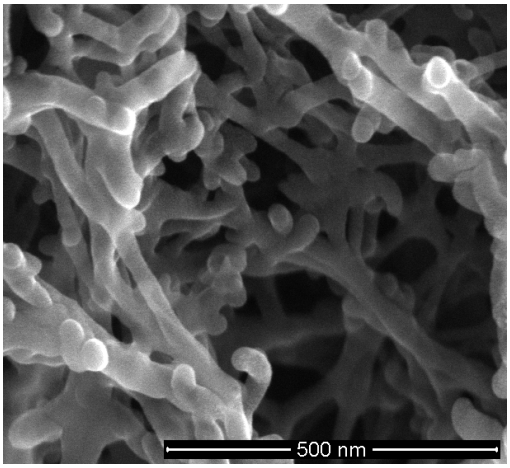

Figure 3.9: A REM image was taken of agarose gel. After the gelling process the agarose molecules (polysaccharide with 1,3-linked β-D-galactose and 1,4-linked 3,6-anhydro-α-L-galactose) polymerize and thereby form a network. The pore sizes are determined by the agarose concentration.

3.3 Sample preparation

Matrices A, B and C have a viscosity low enough to allow for a sample fabrication by simply introducing the nanoparticles in the gels. Unless specified differently, the particle-gel samples are prepared at a mass concentration $c = 0.03$ with $c = \frac{m_{\text{part}}}{m_{\text{gel}}}$ where m_{part} is the mass of the particles and m_{gel} the mass of the gel. Subsequently, the mixture is gently stirred with a glass rod until the particles are finely dispersed, which can be seen from an even coloring. Matrices D and E are solid in their final state. This means that particles have to be introduced while the matrix is still liquid which is during gel preparation. The fabrication of samples with these matrices is described in the following.

Alginate gel

Alginate gel is prepared at room temperature by mixing alginates with a curing agent. The alginates are purchased as powder blend from *Sigma Aldrich* [77] and dissolved in water at a concentration of 2%. As curing agent a 2%-calcium chloride solution is used. When the alginates are brought in contact with the curing agent, the gelling process starts immediately. After the transition to solid the particles are fixed in the gel environment. Thin gel layers are produced by dipping filter paper of the desired layer size in the curing agent. Afterwards, a thin film of alginate solution is applied on top of the filter paper using a syringe. This layer then is covered with a further filter paper having been dipped in the curing agent. Subsequently, both filter papers can be removed carefully and an alginate gel film remains. For the preparation of particle-gel samples, the nanoparticles are dissolved in the alginate solution. With the procedure just described particle-gel films can be produced.
The nanoparticles are introduced before the liquid-solid transition takes place. As long as the matrix is liquid, the particles can be deliberately adjusted in the matrix. If exposed to a homogeneous magnetic field in the liquid gel state, for example, chain fragments orientated in the direction of the external field evolve in the matrix

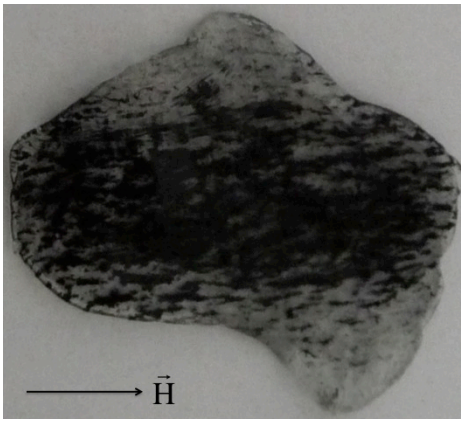

Figure 3.10: A Co nanoparticle-alginate film containing chain structures is shown. The direction of the magnetic field applied during preparation is indicated.

(see figure 3.10). Therefore, the magnetic field (690 Oe) of a magnetic stirrer is applied. After the transition to the solid state, which is initialized by adding the curing agent as described previously, the nanoparticles are fixed in the gel environment.

Besides, biogels such as alginate or agarose gel is formable and different shapes of the gel can be realized (figure 3.11 (a)). Alginate gel spheres, e.g. can be produced by dropping the alginate solution in the curing agent using a syringe (see figure 3.11 (b)). Here, the diameter of the spheres is mainly determined by the size of the used cannula.

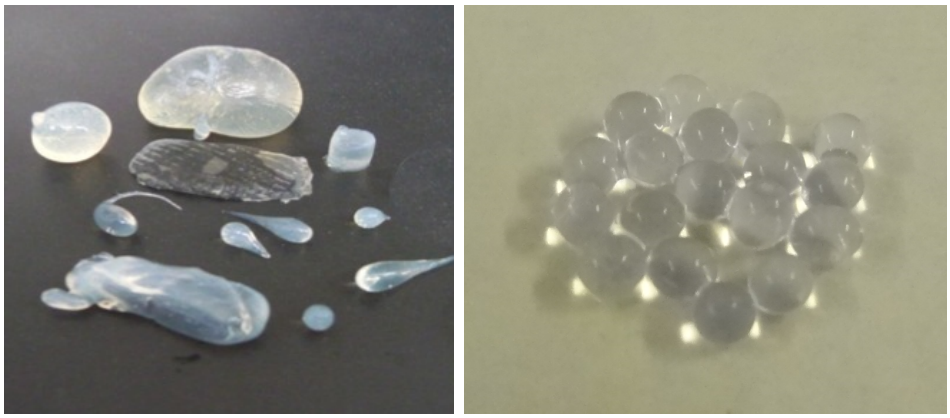

(a) (b)

Figure 3.11: Different shapes have been formed from alginate gel (a). Spheres with an diameter of about 3 mm were fabricated by dropping alginate solution in the curing agent (b).

Agarose gel

The preparation of agarose gel starts with the production of a TRIS Acetate-EDTA (TAE) buffer. Therefore, TAE powder blend of the company *Sigma Aldrich* [78] is dissolved in water. Agarose powder [79] of the desired concentration is then slowly sprinkled in the chilled TAE buffer while the solution is rapidly stirred. Having weighed this solution, it is covered with a plastic wrap with a small hole for ventilation. While stirring it, it is brought to a boil using the hotplate of a commercially available magnetic stirrer, until the whole agarose is dissolved. Finally, sufficient hot water is added in order to obtain the initial weight. Having stirred it once more, the solution is cooled until the gel is cast. The gel can be reliquefied by heating it up again to more than 75 °C. When the gel is liquid, the nanoparticles are introduced. Cooling down the particle-gel mixture initializes the gelling process. After the transition to its solid state, the particles are fixed. For structuring the particles in the sample via an external magnetic field, the sample just as in the case of alginate gel, is placed on the hot plate of the magnetic stirrer for some minutes. With the hot plate turned off the sample subsequently is left to cool.

4 Experimental methods

In the following chapter the experimental setups for the magneto-transport measurements as well as the techniques and analytical tools employed for sample preparation and characterization are described.

4.1 Experimental setup for magneto-transport measurements

Magneto-transport measurements performed in the scope of this work can be divided into measurements with direct current (DC) and measurements with alternating current (AC). Throughout this work they might sometimes simply be referred to as transport measurements or, since the effect that is investigated here is GMR, the term GMR measurement might be used simultaneously with the term magneto-transport measurement.

4.1.1 DC-transport measurements

The DC-transport measurements were carried out at room temperature using a 4-point-probe method. A sketch and a photo of the experimental setup can be seen in figure 4.1. The sample is contacted from above by four gold needles that are configured in-line with a distance of 4 mm between two needles each. A current is injected through the two outer needles by a computer-operated constant current source while the inner needles are used to record the voltage by a *Keithley Model 2000*. The setup is equipped with a computer-controlled electromagnet and covers a maximal range of ± 4000 Oe. In a typical GMR measurement a constant current is applied parallel to the magnetic field which is increased constantly starting from a maximal negative value to a maximal positive value and then decreased in the same manner. The magnetic field is monitored with a Hall-probe and the voltage is recorded simultaneously.
A defined quantity of the particle-gel mixture under investigation can be applied onto a silicon wafer of a size of $1.2\,\text{cm} \times 0.5\,\text{cm}$ with an oxide layer of roughly 50 nm. Installed in the setup it is directly contacted with the gold needles. Water-based gel matrices dry in the process of the measurements, which is associated with the loss of their conductivity. To avoid this, the wafer can be replaced by a modified chip package (figure 4.2 (a)), which allows for the air-tight sealing of the gel sample during measurements and this way prevents it from drying. The quadratic

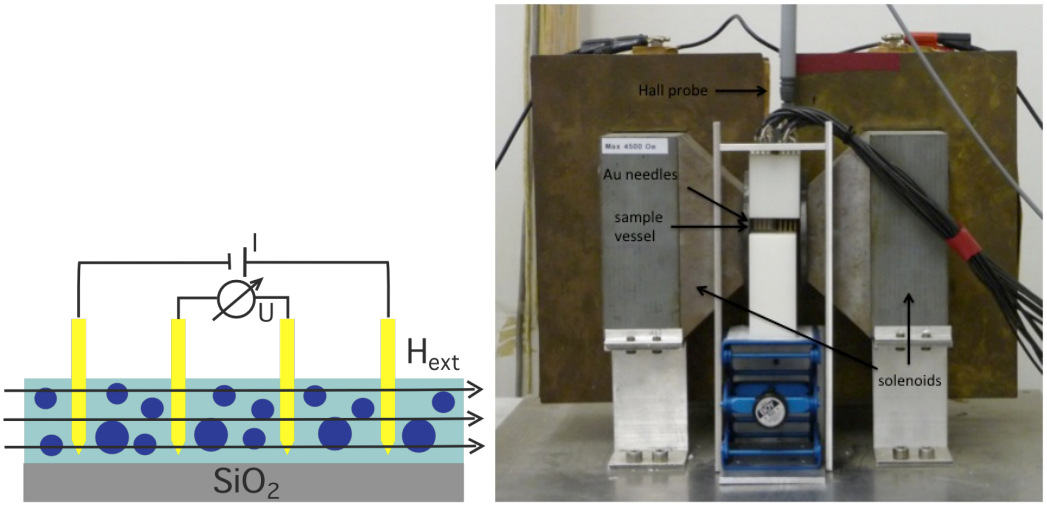

(a) (b)

Figure 4.1: Sketch of the 4-point-probe method used for the magneto-transport measurements (a) and a photo of the experimental setup (b). The particle-gel sample applied onto a silicon dioxide wafer is contacted by four needles. The two outer needles are used to inject the current, while the inner ones are used for the voltage measurement.

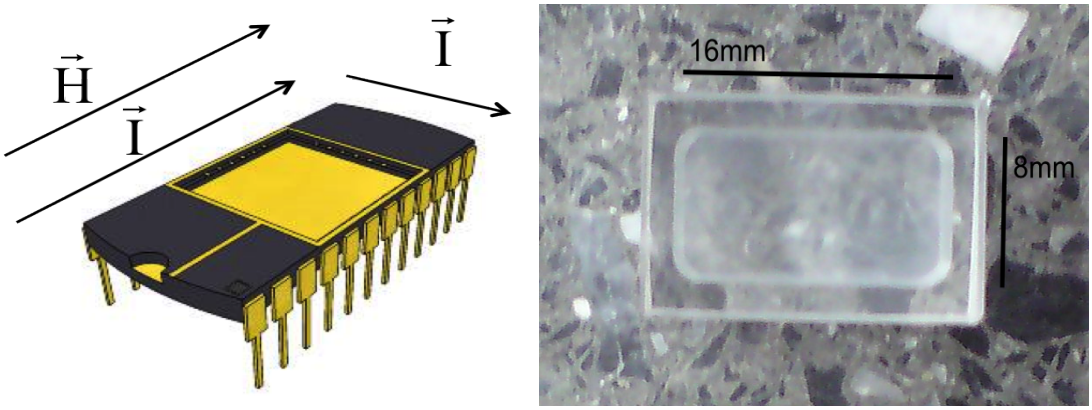

(a) (b)

Figure 4.2: The chip package used for the transport measurements is shown in subfigure (a). The base of the chip package was milled to remove the conducting top layer and to disconnect the conducting border. It can be sealed air-tight with a cover slip. The directions of the applied magnetic field and the possible current orientations are indicated. Subfigure (b) displays the sample vessel made from acrylic glass.

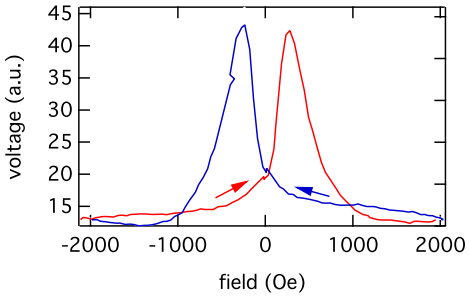

Figure 4.3: The curve of a magneto-transport measurement is exemplarily shown. The recorded voltage is plotted versus the applied magnetic field. Red color (and red arrow) indicates the progression of the curve under increasing and blue color (and blue arrow) under decreasing magnetic field.

conducting base of a conventional chip package as well as the conducting border was milled to prevent any short circuiting. The base with dimensions of 7 mm×7 mm can be filled with a defined quantity of the suspension under investigation which results in a sample height of about 1 mm. Afterwards, the whole arrangement is protected with a cover slip. As a further advantage, this construction provides the possibility to perform both current-parallel- and current-perpendicular-to-field measurements using the same setup. For both configurations two contacts on each side of the chip package, with a distance of 2 mm from each other and 7 mm to the pair of contacts on the opposite side, are chosen. Gel samples that do not require air-tight sealing can also be placed in a vessel made from acrylic glass with a base of 2 cm×1.2 cm and a height of 1.2 cm (figure 4.2 (b)).
A GMR curve is exemplarily shown in figure 4.3. The voltage in arbitrary units is plotted versus field. The red arrow indicates the direction of the progression of the curve under increasing and the blue arrow the progression under decreasing magnetic field. Those arrows will be omitted in the GMR plots throughout this work. The MR ratio or also called effect amplitude is calculated according to

$$GMR = \frac{\Delta R}{R_{\min}} = \frac{R_{\max} - R_{\min}}{R_{\min}}, \tag{4.1}$$

where $R_{\max}$ and $R_{\min}$ are the maximum and the minimum resistance, respectively. In granular systems $R_{\max}$ is obtained for the highest degree of disorder, when the magnetic moments of the single particles are statistically distributed without field, whereas $R_{\min}$ results from the alignment of the single moments in the direction of the external magnetic field. The recorded curves exhibit a linear thermal drift in the resistance over time which was subtracted before the MR ratio was calculated.

4.1.2 AC-transport measurements

The AC-transport measurements were performed using the same 4-point-probe technique as described above. To generate an alternating current, an alternating voltage was applied. Unless specified otherwise, the effective voltage was chosen to be 5 V and the frequency to 110 Hz in order to avoid disturbances, which might occur when using the same or multiples of the frequency of the supply voltage. A high dropping resistance is required in order to obtain a constant current, which can be understood by the following considerations. The sketch in figure 4.4 (a) illustrates the circuit diagram of the transport-measurement setup. Voltage U_{in} is the applied voltage and U the voltage that is measured. In case of an additional serial dropping resistance, the total resistance of the measurement circuit consists of the dropping resistance R_{drop}, the resistance R_{dut} between the two monitoring contacts, as well as the two lead resistances R_1 and R_2. The current of the system hence can be written in dependency of the single resistances as

$$I = \frac{U_{\mathrm{in}}}{R_{\mathrm{total}}} = \frac{U_{\mathrm{in}}}{R_{\mathrm{drop}} + R_1 + R_2 + R_{\mathrm{dut}}} \,. \tag{4.2}$$

From this equation it can easily been seen that the current $I = \frac{U_{\mathrm{in}}}{R_{\mathrm{drop}}}$ is approximately constant for $R_{\mathrm{drop}} \gg R_1 + R_{\mathrm{dut}} + R_2$. The required dropping resistance was determined by performing transport measurements for a known GMR trilayer system with reproducible effect amplitudes. Test measurements were recorded with AC and compared to the DC reference (figure 4.4). With increasing dropping resistance, the AC-MR-effect amplitude increases until it saturates at the reference value. The dropping resistance can subsequently be increased over a broad range from about 10 kΩ up to 100 kΩ without changing the MR-effect amplitude. For dropping resistances of more than about 100 kΩ, the current flow in the electrical circuit is too low for reliable measurements. Since the resistance of the layer system is known to be 10 Ω, it can be estimated that a dropping resistance 1000 times higher than the resistance of the trilayer allows to measure the correct effect amplitude.

4.2 Determination of conductivity

The conductivities of the matrices were determined as follows: The specimen under investigation is measured with the 4-point-probe method in the DC setup described above. With the known distance of the current flow, the conductivity σ is calculated by

$$\sigma = \frac{l}{R \cdot A} = \frac{l \cdot I}{U \cdot A} \tag{4.3}$$

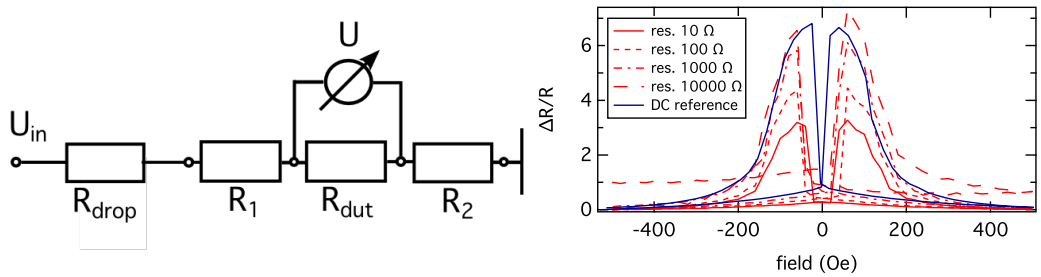

(a) (b)

Figure 4.4: The circuit diagram of the setup for the AC-transport measurement (a) consists of a series connection of a dropping resistance R_{drop}, the resistance R_{dut} between the two monitoring contacts and the two lead resistances R_1 and R_2. U_{in} indicates the applied and U the measured voltage. AC-transport measurements for a known GMR trilayer with different dropping resistances (red lines) and the DC reference measurement (blue line) are shown in subfigure (b).

with R the resistance, I the current, U the voltage and l the distance between the electrodes. The cross section A of the current flow was assumed to $1\,\mathrm{mm}^2$ for all calculations.

4.3 Recording of IV characteristics

The measurements of current-voltage characteristics (IV characteristics) are carried out using a two-point-probe technique, where the sample is contacted with two gold needles. The setup is equipped with a constant voltage source which allows to apply a bias voltage of maximum $\pm 2\,\mathrm{V}$. The current is measured with an electrometer at six possible amplifier settings and the output of the electrometer is recorded by a *Keithley Model 2000* digital multimeter. With this setup a current of maximum 13 mA and minimum 100 pA can be measured. The setup additionally offers the possibility to apply a magnetic field which is generated by a solenoid capable of 3500 Oe. Each needle is connected to a XYZ-sliding table and can be positioned freely on the sample. Measurements hence can be performed with current orientated parallel as well as orthogonal to the magnetic field.

4.4 Instruments and analytical tools

4.4.1 Scanning electron microscope (SEM)

A scanning electron microscope (SEM) was employed for the visualization of the samples as well as for the electron-beam (e-beam) lithography steps in the fabrication of the spin-valve structures for the measurement of the spin-diffusion length. The type used is a *LEO 1513 Gemini* [80] with an integrated lithography system *Elphy Plus* from the company *Raith GmbH* [81]. The possible acceleration voltage ranges from 0.2 to 30 kV. At 20 kV the SEM has a nominal resolution of 1.5 nm. The resolution in electron beam lithography is limited by the thickness of the employed resist and the proximity effect of the secondary electrons. For negative resist the lateral resolution of the patterned structures can reach 50 nm and for positive resist, which has a reduced thickness, less than 20 nm [82].

4.4.2 Electron-beam lithography

The spin-valve structures intended for the measurement of the spin-diffusion length consist of two laterally separated fm layers from which conducting lines lead to contact pads located in a distance of few hundred micrometers. More information and details on the spin valve design can be found in section 9.2. The entire patterning process of these devices can be divided in four main steps: The fabrication of the first fm layer (F1), the second fm layer (F2), the conducting lines and contact pads and, finally, the insulating cover layer. The dimensions of the spin-valve structures are very small such as 200 nm × 700 nm for $F1$ and 2 µm × 3 µm for $F2$. Including the conducting lines such a spin-valve has an overall lateral expansion of only 1 mm. Owe to this property several spin-valve arrays can be constructed onto one sample at the same time.
The first fabrication step involves the patterning of F1 and crosses that will be needed to allow for correct alignment of the sample in the following lithography processes. For a better understanding this first production process is illustrated in figure 4.5. In the cleanroom a silicon wafer with a dioxide layer of roughly 50 nm is coated with positive e-beam resist *AR-P617-03* [83] in a spin-coater (a). A summary of the used resist parameters can be found in table 4.1. The resist subsequently needs to be cured on a hot plate. Based on standard parameters, the time is chosen to 25 minutes which is longer than suggested by the manufacturer. Afterwards, the part of the sample where the FM1 is supposed to be located is exposed to the e-beam in the SEM (b). While the exposed areas of *AR-P617-03* become soluble to the photoresist developer *AR 600-55*, the unexposed parts remain insoluble. When the sample is developed (c), a mold for FM1 is created (d). Before the resist is removed, 5 nm of Ta and a layer of 50 nm of permalloy are sputtered on top of the sample (e) to provide the material for F1. The deposition is accomplished in a magnetron-sputtering chamber *CLAB 600 Clustertool* from

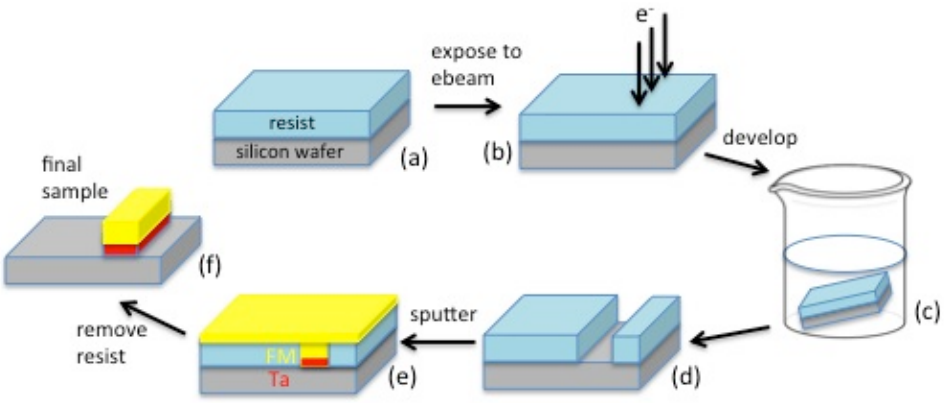

Figure 4.5: The first step of the production process of a lateral spin valve is illustrated schematically.

resist type	PMMA 617 03 Allresist
coating	5000rpm for 30s
baking	25 min at 200°C
developing	AR 600-55 for 2-5 min
stopping	AR 600-60 for 30 s
remover	AR 600-70 for 30 s

Table 4.1: The parameters of the positive e-beam resist used for the fabrication of the spin-valve structures are specified [83].

Leybold Vakuum GmbH [84]. Removing the resist results in the substrate with the final F1 (f). By coating this specimen once again the next lithography step can be realized. Since the lateral distance between F1 and F2 is supposed to be structured very small (for some samples only 20 nm), F2 is patterned in a second step in order to guarantee that the small metal bridge between F1 and F2 after sputtering can be removed in the ultrasonic bath. The last steps comprise the e-beam lithography and sputtering of the conducting lines and an insulating cover layer of e.g., MgO with notches for the gel and the contact pads (compare section 9.2). For the preparation of the conducting lines and pads 5 nm Ta and 35 nm Au were deposited by a magnetron-sputtering machine custom-built at Bielefeld University.

4.4.3 Transmission electron microscope (TEM)

The size distributions of the nanoparticles were determined with a TEM of type *Philips CM 100* with a tungsten cathode operated at an acceleration voltage of 80 kV. Images are recorded by an integrated *Keenview* CCD camera and the software packet *AnalySis Image Processing Pro 3.2* of the company *Soft Imaging Sys-*

tem GmbH. The specimens for the TEM imaging were prepared as follows: A spatula tip filled with the nanoparticles under investigation is dissolved in 0.5 ml 1,2-dichlorobenzene. For the purpose of a thorough intermixing, the solution is placed in an ultrasonic bath for roughly 30 s. Subsequently, 1 µl of the solution is dropped on a silicon-dioxide coated 400 mesh TEM grid. The supernatant is removed by a filter paper.

4.4.4 Focused ion beam (FIB) microscope

The micro structural analyses in this work were performed with a *FEI Helios Nanolab 600* system. It contains a dual beam system with an electron- and an ion-beam column and can be operated as SEM, as scanning transmission electron microscope (STEM), in an energy dispersive X-ray spectroscopy (EDX) and in an ion mode [85]. Furthermore, it comprises a gas injection system to induce ion beam-assited chemical vapor deposition, and a microprobe tool. The acceleration voltages in the SEM mode range from 5 kV to 30 kV. In the ion-beam mode a highly focussed Ga^+-beam at acceleration voltages between 1 kV and 30 kV can be used to cut and thin out fine slices of samples. This was done for the images of the particle-gel sample in section 5.2.1. A dried particle-gel sample was coated with few nanometers of gold to accomplish a better conductive surface. Afterwards, a lamella was prepared by the following *lift-out-technique* [86].

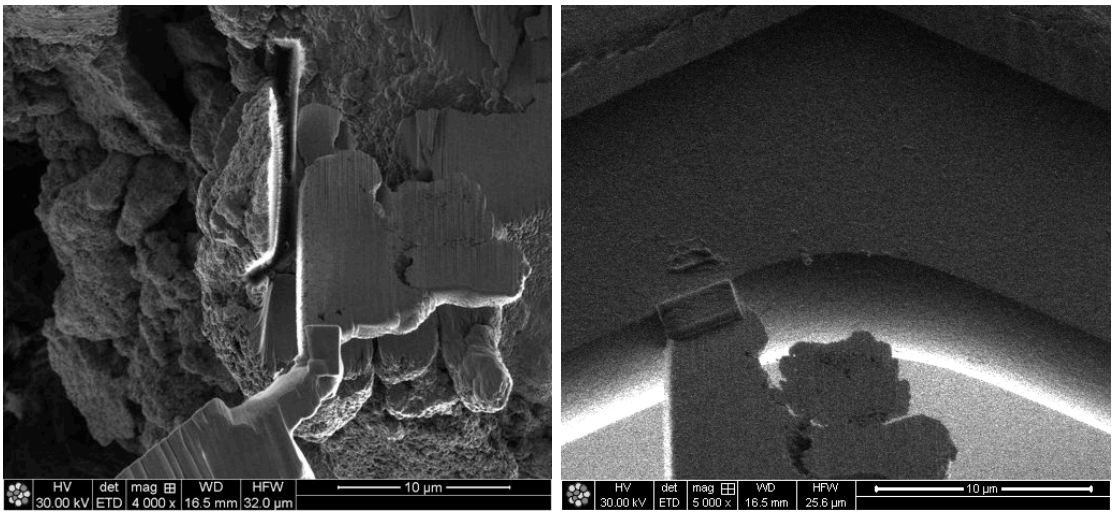

(a) (b)

Figure 4.6: The lamella (in the center right) attached to the micromanipulator (in the lower part of the image) and a trench dug on its left side is shown (a). By further trenches the lamella is then cut out, maneuvered and attached to a copper post (b).

The region of interest on the sample is covered with a Pt layer of 0.5 µm to protect

it against subsequent damage by ion beam overspray. Via FIB milling trenches are dug from two sides to prepare a slice of desired thickness. The sample is tilted and the slice is undercut so that it is only attached at one edge. The micromanipulator then is positioned close to the sample ($< 0.5\mu m$) and Pt deposition is used to attach it to the sample (figure 4.6 (a)). The sample is lifted out and maneuvered to another conductive post for further treatment (figure 4.6 (b)). Typical sizes of a lamella are 10 µm ×1 µm for the area and about 5 nm for the height. By milling it is detached from the micro-manipulator needle and thinned out in severals steps.

4.4.5 Alternating gradient magnetometer (AGM)

The magnetization measurements were performed using a *Micromag Model 2900 Alternating Gradient Magnetometer System (Princeton Measurements Corporation)* [87]. It enables the measurement of the total magnetic moment with a sensitivity of 10 nemu standard deviation at room temperature at a maximum applicable magnetic field of ±14 kOe. Figure 4.7 schematically shows the structure of an AGM.

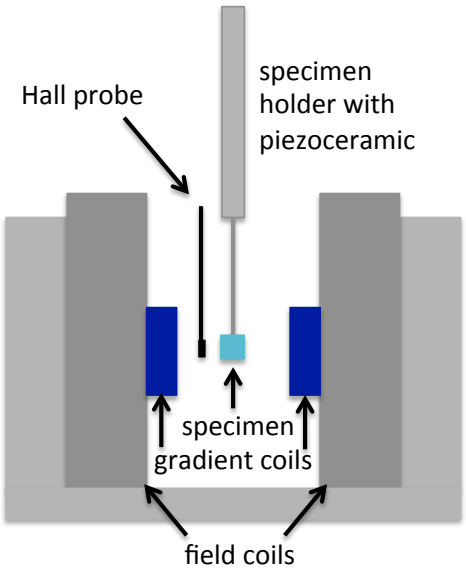

Figure 4.7: The structure of an AGM is schematically shown.

Two field coils generate a static, homogenous magnetic field which is monitored by a Hall probe and magnetizes the sample. The sample itself is mounted on the tip of a vertical extension rod (specimen holder), which is attached to a piezoelectric element. The top end of the piezoelectric element is rigidly fixed. An alternating field gradient generated by the gradient coils is used to produce a periodic force on the magnetized sample. The force acting on the sample leads to the deviation of the sample and thus a bending moment on the piezoelectric element, which induces a voltage proportional to the force on the sample. The output of the piezoelectric element is detected by means of a lock-in amplifier in dependence of the external

homogenous magnetic field. Before each measurement the resonance frequency of the system consisting of sample and sample holder is determined by varying the frequency of the alternating voltage at the gradient coils. The voltage generated in the piezoelectric element has its maximum in the case of the resonance frequency and the magnetic moment can be reliably assigned. Using a specimen with known magnetic moment, the AGM is calibrated in order to quantitatively determine the magnetic moment of the sample under investigation.

5 Hydrogel matrices

This chapter summarizes the results of the DC-transport measurements that were performed on particle-gel samples. Both Co and Heulser-based nanoparticles were integrated into granular gel systems and showed promising effect amplitudes regarding technological relevance. Parts of this chapter have been published in [88].

5.1 Transport measurements with Co nanoparticles

The first transport measurements at room temperature were carried out for Co nanoparticles in matrix A. The conductivity of matrix A was determined to be in the range of 0.2 S/m to 1.2 S/m. The samples are applied on a silicon dioxide wafer and installed in the experimental setup (see section 4.1.1). The magneto-transport measurements are performed by applying a constant current of 5 µA parallel to a magnetic field. The low value of the current is chosen in order to avoid electrolysis of the water contained in the gel that might have an impact on the recorded voltages. The magnetic field is increased from −2000 Oe to 2000 Oe in steps of 50 Oe and then decreased in the same manner. Figure 5.1 shows a series of subsequent DC-transport measurements. Due to drying of the matrix and the associated loss of its conductivity, the effect amplitude of about 60% declines gradually over a time span of roughly 10 minutes until the GMR effect is no longer measurable. With the gel completely dried, the sample is no longer electrically conductive. This implies that no direct conductive connections between the electrodes resulting from the formation of magnetic particle superstructures are existent. The GMR curves show a hysteretic field dependence with peaks located symmetrically to zero field. After the transport measurements the magnetic behavior of the sample was analyzed by AGM measurements at room temperature. Figure 5.1 indicates that the maxima of the MR curves appear at the coercive field revealed by AGM, which is the finger print of GMR-behavior [4]. The drying of the gel on the silicon wafer can be prevented by the use of a modified chip package as described in section 4.1.1. When the specimen is sealed air-tight, the GMR effect is stable over a longer period of time. Figure 5.2 shows a series of measurements for a time span of 80 minutes. The GMR-effect amplitude fluctuates around a mean height of (17.0 ± 3.6) %.

In granular solids, the concentration of nanoparticles affects the GMR-effect height. With increasing particle concentration the effect amplitude increases due to an increase in the concentration of the magnetic scattering centers. It reaches a max-

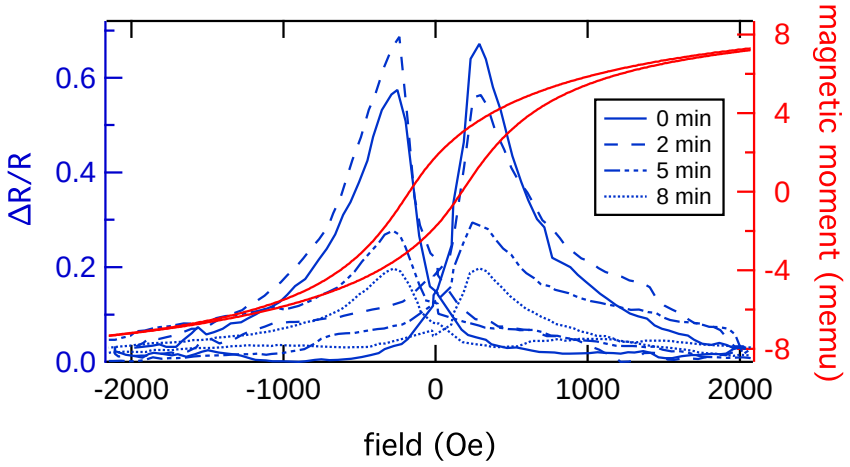

Figure 5.1: Subsequent transport measurements of Co nanoparticles in matrix A are shown (blue). Due to drying of the carrier substance, the effect amplitude declines gradually over a period of 10 minutes. Afterwards, the magnetic behavior of the sample was analyzed by AGM measurements at room temperature (red).

Figure 5.2: Sealing the particle-gel sample during the magneto-transport measurement leads to a GMR-effect height (red markers) that oscillates around a mean amplitude of about 17 % (black markers as a guide to the eye).

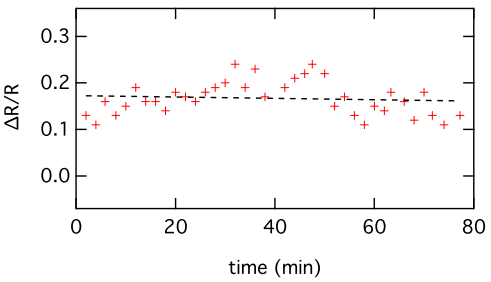

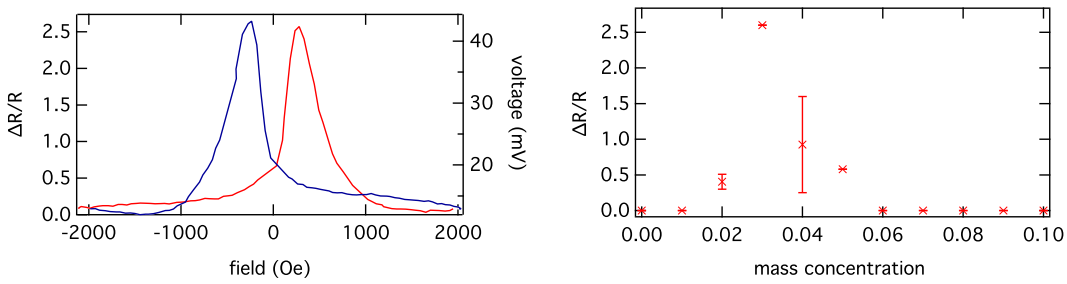

(a) (b)

Figure 5.3: A transport measurement with an effect amplitude of about 260 % was obtained with Co nanoparticles in conductive matrix A (a). A constant current was applied parallel to field. Co nanoparticles were measured in matrix A for different concentrations (b). The effect range where an MR effect occurred is plotted versus the mass concentration.

imum and decreases again with further increase of the concentration [10, 89]. No MR effect can be measured when all particles are connected. Such a behavior was confirmed by transport measurements of Co nanoparticles in matrix A carried out for different mass concentrations c (compare figure 5.3 (b)). MR effects could only be measured for concentrations ranging from $c = 0.02$ to $c = 0.05$. The concentration leading to the highest effect amplitudes was found to be about $c = 0.03$. However, it has to be stressed that the effect height varied over an extensive area as indicated by the error bars. This behavior can be attributed to the high particle mobility in the matrix which leads to clustering of the particles caused by the applied magnetic field in the course of the transport measurement. Each sample hence provides an inhomogenous particle density, which results in locally differing effect heights for samples with actually the same particle concentration depending on where the contact needles are positioned.

5.1.1 Comparison of different matrices

The highest GMR values with an effect amplitude of up to 260% were measured with matrix A (figure 5.3 (a)). This is far above the values known for GMR multilayers [90, 91] or conventional granular systems [4, 92, 93] at room- or even at low temperatures. Effects with lower amplitude could also be attained with matrices B and C (figure 5.4 and figure 5.5). The conductivity of matrix B was measured with up to 2 S/m and the conductivity of matrix C was found to be in the range of 0.03 S/m to 0.09 S/m. The GMR measurement of the sample with matrix C obviously exhibits a high noise level (figure 5.4). This is in contrast to the GMR measurements of the samples with the matrices A and B (figure 5.3 (a) and figure 5.5) and might be associated with the poor conductivity of matrix C, which is more than 10 times lower than the conductivity of the other matrices, and the resulting

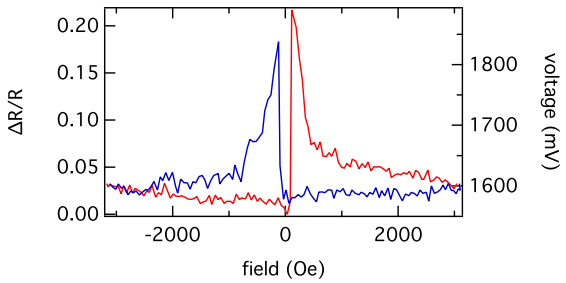

Figure 5.4: The figure displays a GMR measurement for matrix C.

poor contact during the measurement.
Furthermore, it is apparent that the recorded MR curves for the matrices additionally vary in terms of their shape and effect height. While the peaks for matrix C (figure 5.4) and matrix A (figure 5.3 (a)), for example, are narrow, they are quite broad for matrix B (figure 5.5). Besides, it has to be noted that the particle-mass concentration necessary to obtain an effect was $c = 0.08$ for matrix B and thus higher than the concentration of $c = 0.03$ used for matrix A and C. These differences can be related to the viscosity of the respective matrix. The viscosities of all hydrogels tested are low enough to allow for particle movement. For a low viscosity such as for matrix A or C, it was easier to finely distribute the nanoparticles in the gel than for matrix B. A homogenous particle distribution within the matrix, however, is essential in so far as the gel distances within the system have to be smaller than the spin diffusion length in order to measure a spin-dependent effect. Due to its higher viscosity a higher particle concentration was required for matrix B to achieve the necessary particle arrangement despite the poor solubility and to measure a GMR effect. In addition, due to the lower viscosity, the mobility of particles in matrix A and C was higher than in matrix B. This way, chain fragments of particles coupled due to magnetic dipolar forces evolved more easily under influence of the magnetic field as discussed in [94]. If those chains, however, are orientated in the direction of the current flow, this results in an enhanced particle volume density in the latter or, more precisely, an increase of particle-gel-particle interfaces. Assuming that GMR only occurs in the Co particle fragments and interfaces, respectively, this leads to higher effect amplitudes due to an increased spin-dependent scattering [95] compared to samples without chains and thus less dense particle assemblies. For that reason higher effects were obtained for matrix A and C.

Another important parameter is the conductivity. Keeping all other experimental parameters identical, higher conductivity results in higher effect amplitudes. In our experimental approach, the conductivity, unfortunately, cannot be tuned without also changing the viscosity, as can be seen for matrices B and C. High conductivity alone is not sufficient to achieve high effect amplitudes as in the case of matrix B that showed the best conductivity, but additionally a very high viscosity. Moreover, good effects were obtained with matrix C despite poor conductivity, but a

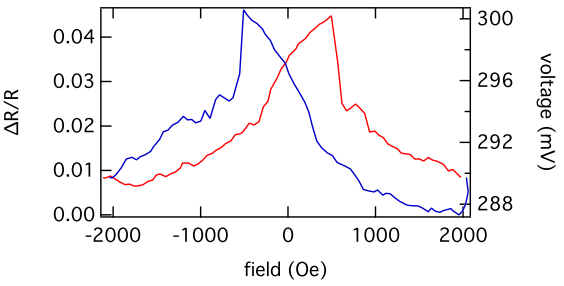

Figure 5.5: A typical GMR measurement for matrix B is shown.

viscosity that was optimized by adjusting the concentration of water and glycerin. Large effects therefore require both high conductivity and an appropriate viscosity, low enough to allow for some chain formation, but high enough to prevent the sedimentation of particles

5.1.2 Perpendicular-to-field measurements

As already mentioned, matrices A, B and C have a viscosity low enough to allow for particle movement under the influence of the magnetic field. For that reason, however, chain fragments and particle clusters evolve during the measurement in the direction of the external magnetic field. On that score, there are two different measurement geometries for our particle-gel samples: current-parallel-to field (CPF) and thus parallel to the chain fragments and current-perpendicular or orthogonal-to field (COF) and chain fragments, respectively (compare figure 5.6). Using the chip package magneto-transport measurements were carried out in both configurations for the same sample in order to examine whether particle chains oriented in the current direction are essential for the occurrence of a MR effect. It was found that a GMR effect could be measured in both configurations. Figure 5.7 gives an example of such measurements.
It is striking, however, that the measured voltage of the specimen is higher in orthogonal configuration (figure 5.7 (b)) than in parallel configuration (figure 5.7 (a)) and that the effect amplitude for the parallel configuration with 25% is slightly higher than the amplitude for the perpendicular configuration, which only reaches about 21%. Furthermore, the curves look different in terms of their shape. While the GMR peaks in parallel configuration are rather narrow, they are quite broad in the perpendicular case.
The difference in these characteristics can be associated with the generated chains that lead to an uniaxial anisotropic particle density in the specimen. When the current is applied parallel to the chains as depicted in figure 5.6 (a), the current mainly flows through the cobalt chain fragments. In this configuration the current thus is higher than in the COF configuration, where the current flow is perpendicular to the chains (see figure 5.6 (b)) and more sections of the less conductive gel have to be passed. For that reason, the voltage and the resistance, respectively, are higher in the orthogonal configuration. Similarly, a CPF configuration is associated with an

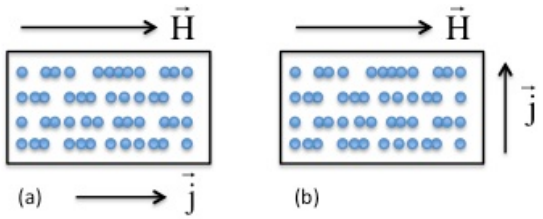

Figure 5.6: The configuration with current parallel (a) and current perpendicular to magnetic field (b) for the transport measurements are sketched out. The nanoparticles symbolized in blue are arranged in chains due to the external magnetic field.

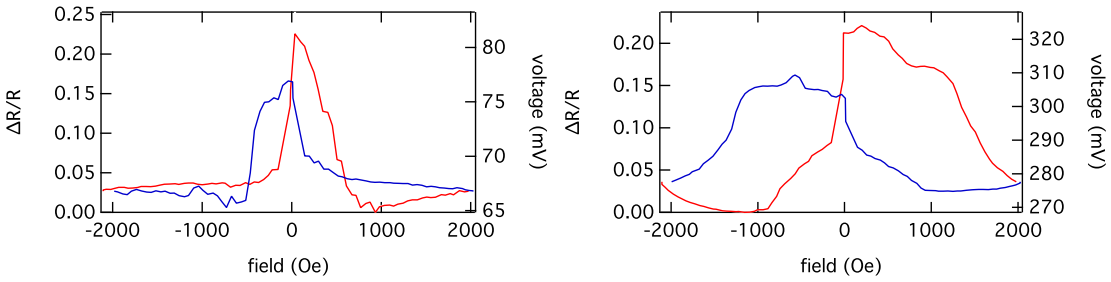

Figure 5.7: Magneto-transport measurements of the same particle-gel sample are shown for the current-parallel-to-field (a) and the current-perpendicular-to-field configuration (b). The different measurement geometries result in different voltages and shapes of the curves measured at the sample.

enhanced particle volume density and a rise in the number of particle-gel-particle interfaces in the current path, which, as previously discussed, leads to an increased spin-dependent scattering and thus larger effect amplitudes [95]. The differently formed curves for the two configurations are attributed to the shape anisotropy of the sample. While there are mainly longer chains of dipolar coupled nanoparticels in the current path in case of the CPF configuration, there are lots of differently sized smaller chain fragments in case of the COF configuration, which leads to a broad distribution of switching fields in the case of the COF- (figure 5.7 (b)) and a narrower one in the case of the CPF configuration (figure 5.7 (a)).

5.2 Monitoring of transport measurement

In order to investigate to what extend particles move by means of the varying external magnetic field, a specimen with matrix A was monitored simultaneously to performing a transport measurement. Therefore, an optical microscope of type *Keyence VHX-600* was installed at the experimental setup. Although the reso-

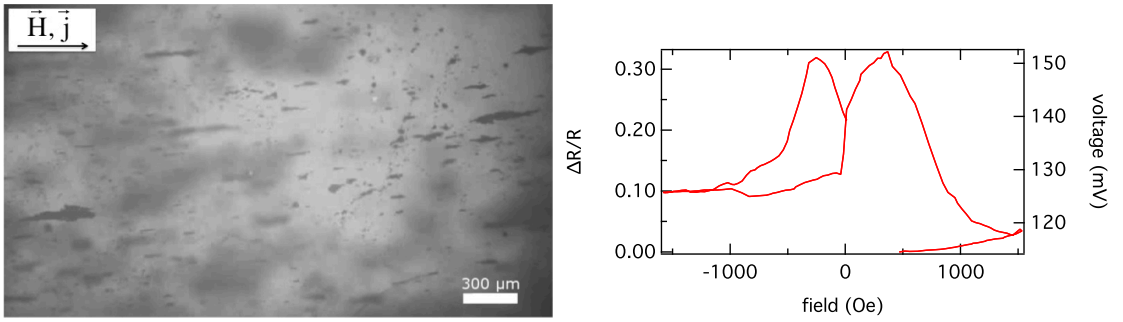

(a) (b)

Figure 5.8: A GMR sample composed of Co-nanoparticles in gel matrix A was monitored during a magneto-transport measurement. The specimen at the maximal applied magnetic field (a) and the corresponding GMR curve (b) are displayed. The large darker areas in subfigure (a) can be attributed to unevenness in the substrate surface or agglomerates above the focus of the microscope. Due to the application of the magnetic field, stable dipolar coupled chains fragments have evolved.

lution of an optical microscope is not sufficient for the observation of nanoscale particle dynamics, optical microscopy seemed to be the most obvious approach for the following reasons: Methods such as SEM are eliminatory. First of all, this is due to the difficulty to realize a simultaneous observation of transport measurement there and, secondly, due to the fact that they have to be operated under vacuum which would dry the water-containing gel in the samples. Though an optical microscope has a poorer resolution than a SEM, it does provide the option to monitor bigger agglomerates and their dynamics. For a better analysis of the monitoring, a film of the evolution of the GMR curve was created so that the development of the curve and the processes in the specimen could be watched synchronously. It was observed that stable chains evolved with initial increase of the magnetic field. Figure 5.8 (a) resembles the sample at the maximal applied magnetic field of 2000 Oe and figure 5.8 (b) shows the measured GMR curve. The formation of continuous macroscopic particle chains over the entire sample length did not occur. This supports the assumption that no closed conduction paths result from the agglomerate formation as was already stated in the context with the drying of the matrix in section 5.1. The dipolar coupled chain fragments remained intact during the measurement, even at the zero crossing of the field, where a rotation of them could be observed. This method of observation poses the difficulty that the depth of field is much smaller than the sample height. The large darker grey areas in figure 5.8 (a) hence are attributed to either agglomerates that are not in the focus of the microscope or unevenness in the substrate surface.

5.2.1 Microstructural analysis

For the study of the inner arrangement of the nanoparticles in the gel matrix, a FIB microscope with an integrated SEM was used (see section 4.4.4). A dried sample of Co nanoparticles in matrix A was prepared at the FIB microscope according to the *lift-out technique* described in section 4.4.4. Figure 5.9 shows the thinned out lamella. The image was taken in the STEM mode, where the electron detector is below the specimen and electrons pass through it before they are detected. The so-called *bright field* mode was used. The transmitted primary beam is detected and electrons diffracted by the sample are blocked by apertures. The thicker the sample or the higher the atomic mass number of the material, the more electrons are diffracted and the darker the scanned area appears. The Co nanoparticles hence appear darker than the thin surrounding carbon shell or the gel matrix. Particles of different sizes can be seen in the matrix. Larger and medium-sized particles are distributed over the whole area. A closer look also reveals very small particles finely distributed in-between. Chain structures of smaller particles can be guessed. It has to be noted, however, that drying of the gel reduced the original sample volume and inter-particle distances.
EDX analysis was used in order to gain more information on the particle distribution. Figure 5.10 shows the line scan over a larger particle of the lamella. Besides the Co (green) from the particle, carbon attributed to the particle shell (red) is found. According to this scan an accumulation of all Co particles to a huge Co block or to multiple macroscopic chains can be excluded. The Ga (blue) in the sample originates from chemical impurities caused by the ion beam.

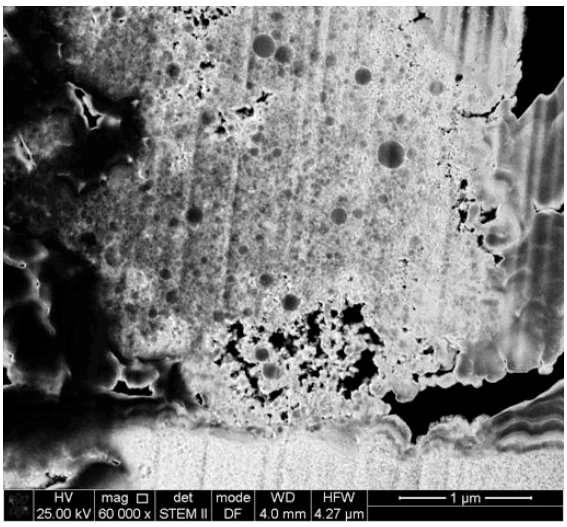

Figure 5.9: A lamella was cut out of a particle-gel sample and thinned out by milling with Ga^+ ions. The image was taken in the STEM mode of the FIB microscope. Differently sized particles embedded in the dried gel can be seen.

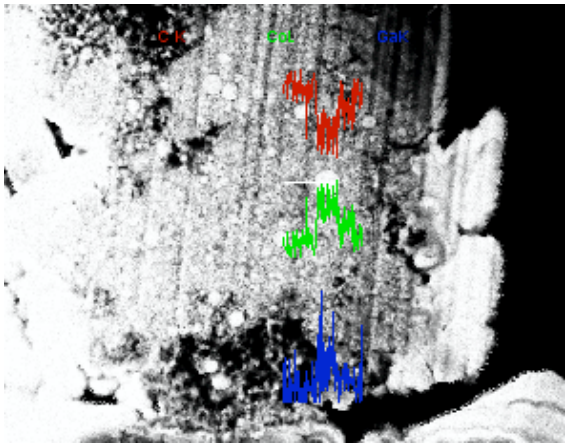

Figure 5.10: A particle-gel sample was analyzed by EDX spectroscopy. The Co (green) can be attributed to the nanoparticles themselves and the carbon (red) to their shell. The Ga (blue) that is found originates from chemical impurities caused by the ion beam.

5.3 Transport measurements with Heusler-based nanoparticles

Recently, ternary Co_2FeGa Heusler-compound nanoparticles have successfully been synthesized (see section 3.1.2). Incorporation of those particles in granular systems could lead to further progress as they would benefit from the qualities of Heusler compounds already known from layer systems such as a soft magnetic behavior and a high Curie temperature. As a first step in this direction we implemented Co_2FeGa nanoparticles [56–58] in matrix A (for the characteristics of particles and matrix see section 3). Magneto-transport measurements using a 4-point-probe method were carried out at room temperature revealing MR effects of up to 120% (compare figure 5.11). As already mentioned this is above common GMR values for granular systems at room- or even low temperatures [4, 92, 93].

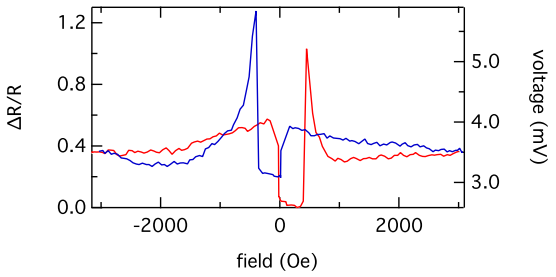

Figure 5.11: Transport measurement of Heusler-based nanoparticles of type Co_2FeGa in matrix A revealed effect amplitudes of up to 120%. Narrow GMR peaks are apparent.

The switching field for the transport measurement and the coercive field revealed by AGM are similar, but not identical. While the peaks in the transport measurement are located at about 400 Oe (compare figure 5.11), the coercive field is determined to be about 150 Oe (see section 3.1.2 figure 3.3). This difference originates from the different samples used for the respective measurements.
Furthermore, it is striking that the GMR characteristics of the Heusler nanoparticles are narrower than the ones recorded for the Co nanoparticles. Calculations

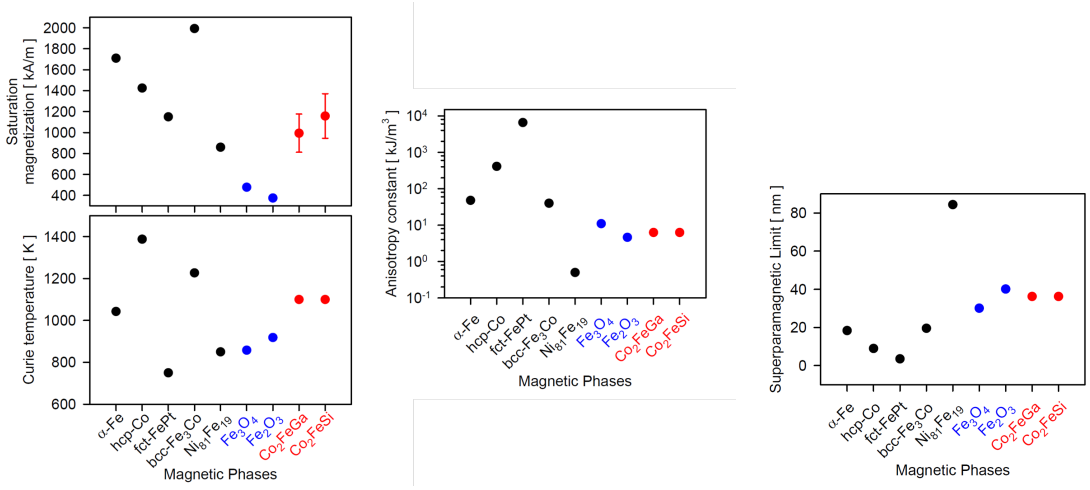

(a) (b)

Figure 5.12: The intrinsic magnetic properties for different magnetic phases are shown (a). The Heusler compounds Co_2FeGa and Co_2FeSi exhibit medium large saturation magnetizations, low magnetocrystalline anisotropies and rather large Curie temperatures. The data are collected from [55, 58, 97, 98]. The corresponding calculated superparamagnetic limits are summarized in (b). The limits of the Heusler compounds Co_2FeGa and Co_2FeSi are comparable to those of Fe_2O_3 or Fe_3O_4.

have been carried out comparing four magnetic phases, namely hcp-Co, Fe_3Co, Fe_3O_4 and the Heusler compound Co_2FeSi, in order to investigate the influence of the utilization of Heusler nanoparticles on the GMR characteristics of granular systems [96]. Figure 5.12 (a) gives an overview of the saturation magnetization, the anisotropy constant and the Curie temperature of the two Heusler compounds Co_2FeGa and Co_2FeSi and magnetic phases such as Fe_2O_3 or Fe_3O_4 to illustrate the intrinsic magnetic properties of Heuslers compared to conventional magnetic phases. It is apparent that the Heulser compounds feature a medium large saturation magnetization, a rather high Curie temperature and low magnetocrystalline anisotropy constants. The superparamagnetic limit of the magnetic phases at room temperature can be calculated when assuming spherical nanoparticles and applying the equilibrium condition (compare section 2.1.3)

$$KV = 38 k_B T, \tag{5.1}$$

where the product of anisotropy constant K and particle volume V balances thermal fluctuations at room temperature with k_B being the Boltzmann constant and

magnetic phase	color code	D_{sp} (nm)	$\langle D \rangle_{sp} \pm \sigma$
hcp-Co	black	9.0	7.5 ± 0.75
Fe_3Co	blue	19.6	15.0 ± 1.5
Fe_3O_4	pink	30.1	23.0 ± 2.3
Co_2FeSi_4	red	36.3	28.0 ± 2.8

Table 5.1: The table gives an overview of the magnetic phases considered for the calculations of the magnetic reversal and the GMR characteristic, the corresponding color code, the calculated superparamagnetic limit D_{sp} and the size distribution in the superparamagnetic regime.

T the temperature. Note that this is the equilibrium condition for nanoparticles that are considered to be magnetically stable against thermal switching for one year. The resulting superparamagnetic limits D_{sp} are displayed in figure 5.12 (b). The magnetization reversal for nanoparticles in the superparamagnetic regime can be calculated using a Langevin function [99] taking into account the nanoparticle size distributions over a $\pm 5\sigma$ range:

$$M(H_{ext}) = M_s \int_{\langle D \rangle_{sp}-5\sigma}^{\langle D \rangle_{sp}+5\sigma} \frac{1}{\sqrt{2\pi}\sigma} \exp\left(-\frac{(D-\langle D \rangle_{sp})^2}{2\sigma^2}\right) \left(\coth\left(\frac{\frac{4}{3}\pi\left(\frac{D}{2}\right)^3 M_S H_{ext}}{k_B T}\right) - \frac{k_B T}{\frac{4}{3}\pi\left(\frac{D}{2}\right)^3 M_S H_{ext}}\right) \mathrm{d}D \ . \tag{5.2}$$

Here, M_s gives the saturation magnetization (figure 5.12) and $\langle D \rangle_{sp}$ is defined as the nanoparticle size distribution over a $\pm 1\sigma$ range around the mean particle size $\langle D \rangle$ in the superparamagnetic regime.
For nanoparticles in the fm regime, on the other hand, the magnetization reversal can be described by the following equation [100]

$$M(H_{ext}) = \frac{2M_s}{\pi} \mathrm{atan}\left(\frac{H_{ext} \pm H_c}{H_c} \tan\left(\frac{\pi S}{2}\right)\right) \text{ with} \tag{5.3}$$
$$H_c = 0.556 H_A \left(1 - 0.977 \left(\frac{k_B T}{KV} ln\left(\frac{f_0 \tau}{ln(2)}\right)\right)^{\frac{2}{3}}\right).$$

The coercivity H_c is estimated assuming that the magnetic nanoparticles are randomly oriented [101]. S is the squareness of the magnetization loop. It is defined as the ratio of the remanence divided by the saturation magnetization and is estimated to be 0.75. The frequency factor f_0 is assumed to be 10^9 Hz and the measurement

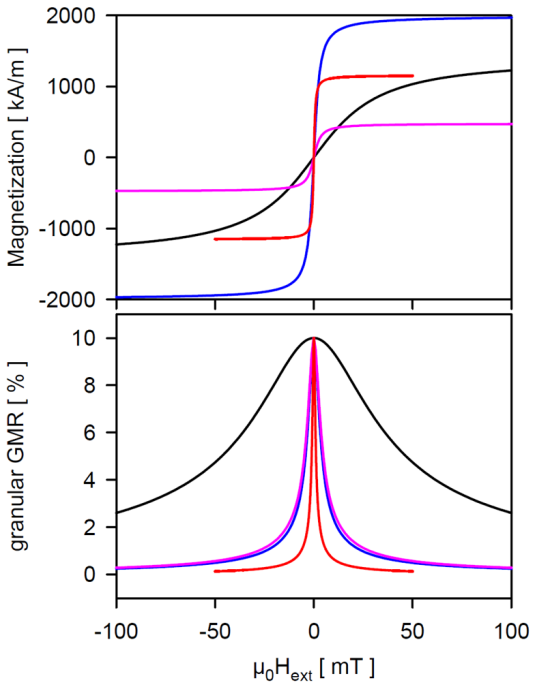

Figure 5.13: The calculated super paramagnetic magnetization curves for non-interacting magnetic nanoparticles at room temperature and the resulting GMR behavior of the particles when embedded in a conductive matrix are shown for four magnetic phases (for color code see table 5.1). The GMR characteristic of the Heusler compound (red) is very narrow which - if applied as a sensor - corresponds to a high sensitivity.

time τ to be one year. The anisotropy field H_a is estimated by a Stoner-Wohlfahrt-Ansatz [97]. The resulting magnetization curves can be seen in figure 5.13 and figure 5.14 for the superparamagnetic and the fm limit, respectively. For Co_2FeGa a behavior similar to the one of Co_2FeSi can be expected with about the same value for K. Considering granular systems where nanoparticles are embedded in a well-conducting matrix and under the presumption that the dipolar stray fields of the single particles do not interact - which is assumed here for the sake of simplicity - the GMR characteristics can be evaluated by inserting equations 5.2 and 5.3 in [89, 102]

$$\frac{\Delta R}{R}(H_{ext}) = A\left(1 - \left(\frac{M(H_{ext})}{M_s}\right)^2\right). \tag{5.4}$$

A denotes the MR effect amplitude and is assumed to be 10% in our case. The large D_{sp} and M_s of Co_2FeSi results in a very narrow GMR characteristic (figure 5.13 and 5.14).
A comparable behavior can be expected for Co_2FeGa due to very similar values for D_{sp} and M_s, respectively. This is in accordance with the GMR measurements of the Co_2FeGa particles embedded in matrix A (compare figure 5.11). Such a soft switching and narrow peaks in the GMR curve are of high technological relevance in regard of magnetoresistive sensors as they entail a high detector sensitivity [103]. The soft magnetic behavior thus makes Heusler compounds ideal candidates for the

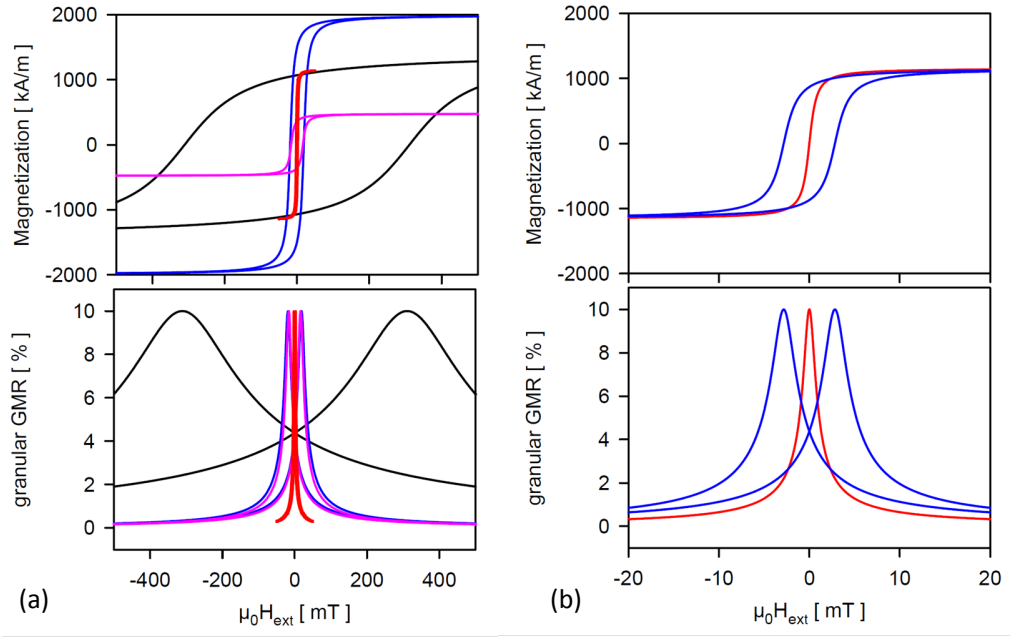

Figure 5.14: The magnetization curves and the resulting GMR characteristics of the considered magnetic phases are shown (for color code see table 5.1) (a). The magnetization reversal and the GMR curve for the Heusler compound in the superparamagnetic (red) and ferromagnetic regime (blue) are given (b).

employment in GMR devices. In particular, Heusler-based nanoparticles are very well suited as grains for granular-GMR systems based on gel matrices.

5.4 Summary

Co nanoparticles have been embedded into different conductive hydrogels as matrices for granular GMR systems. Magneto-transport measurements revealed GMR effects with amplitudes of up to 260 % which is large compared to conventional granular GMR systems. The employed matrices are not solid state objects such as common metallic ones, but viscoelastic fluids with a viscosity low enough to enable particle movement under the influence of the magnetic field. In particular, agglomerates and dipolar coupled chain fragments of single nanoparticles evolve with an initial increase of the magnetic field as was observed by optical microscopy. These chains are orientated in the direction of the external magnetic field which leads to an uniaxial anisotropic particle density within the sample. The formation of a path of pure Co connecting the electrodes over the entire sample length can be excluded as transport measurements no longer reveal a MR effect when the gel matrix is dried. MR effects could be measured independent on whether the current

was applied parallel or perpendicular to the magnetic field and thus to the chain fragments. The effect height in the CPF configuration, however, was found to be slightly higher than in COF configuration, which could be explained by the fact that chains in the direction of the current path increase the particle volume density and hence the number of particle-gel-particle interfaces in the latter. This in turn results in higher effect amplitudes due to an increased spin-dependent scattering [95]. Granular GMR systems based on gels thus definitely benefit from the specific fact that higher nanoparticular volume fractions in the current path can be generated which lead to large effect heights.
The introduction of Heusler compound nanoparticles in the conductive matrix led to a narrowing of the GMR characteristic while maintaining the large effect heights. The soft switching observed could be attributed to the Heusler phase and is of high technological relevance since it results in high sensitivity in terms of sensor application.
Besides the high effect amplitudes, granular systems based on gel offer the advantage of being printable. In view of sensor production, both manufacturing steps and production costs could be reduced with the omission of sputtering and lithography steps. In this context, the employed hydrogels, however, pose some major difficulties. Firstly, the gels did dry very fast which means that they lose their conductivity and secondly, it cannot be ruled out that particles are still mobile during measurement due to the low viscosity of the hydrogels which results in varying GMR characteristics over time. While the first issue could be rectified by sealing the matrix, the second point remains unsolved. On that score, the replacement of matrices A, B and C by biogels that feature a liquid-solid transition and thus provide the decisive advantage that one can purposely arrange and fix the particles within the matrix, is an option to gain control of these difficulties. These biogels will be introduced in the next chapter.

6 Gel matrices with liquid-solid transition

The gels examined so far face the difficulty of a low viscosity which is not desirable regarding the application as a matrix for a GMR sensor. Once embedded in the gel, particles thus are still mobile which leads to unstable response characteristics. Therefore, more viscous gels featuring a liquid-solid transition were tested (matrix D and E). These gels are prepared starting from a liquid state. Particles can be dispersed in the gel before the gelling process is initialized by either adding a cross linking agent (matrix D) or cooling the sample (matrix E). After the transition to the solid state, the particles are fixed in the gel environment. The fact that the time of the gelling can be assigned specifically allows to create particle superstructures in the sample. In the following, matrices D and E are tested concerning their applicability as a GMR matrix. Some contents of this chapter have been published in [88].

6.1 Conductivity of gel matrices

Figure 6.1 (a) displays the conductivity of matrix-D films in dependency of the alginate concentration. Within the error tolerances, the measurements revealed no significant influence of the alginate concentration on the conductivity. The standard matrix D prepared in the framework of this thesis with a 2 %-alginate

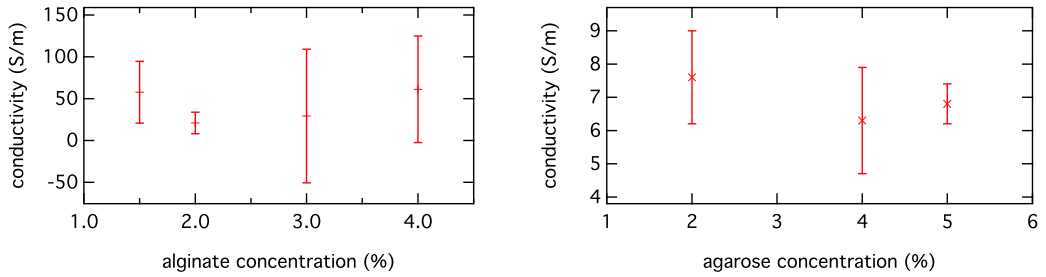

(a) (b)

Figure 6.1: The conductivity was measured for alginate (a) and agarose films (b) in dependency of a varying alginate and agarose concentration, respectively.

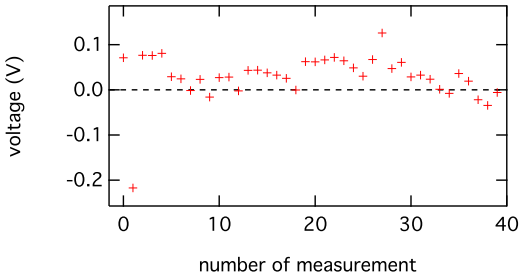

Figure 6.2: The oscillating baseline voltage of a film of particles embedded in matrix D is displayed for a series of transport measurements.

concentration showed the smallest deviation from the mean value. Its conductivity was measured to $(20.8 \pm 12.9)\,\mathrm{S/m}$. Yet, despite efforts to prepare the samples identically, large deviations from the mean values did occurr caused by a strongly fluctuating baseline voltage. The term *baseline voltage* in this context refers to the voltage recorded when the magnetic moments of all magnetic particles are saturated and aligned with the external field. Figure 6.2 illustrates the baseline voltage over time for a series of transport measurements. Changes of sign occurred at random intervals which is synonymous with a change in current flow direction. Reasons for the voltage variations might include electrolysis effects and a rapid development and degradation of an internal counter voltage (compare chapter 7). Another point to consider is that, even though, the gel did not dry and lose its conductivity within only few minutes such as the hydrogels tested in section 5, more and more humidity evaporates. Indeed, the adsorbed water present in solid polymer electrolytes can strongly influence the absolute value of protonic and ionic conductance, respectively [104, 105].
The conductivity of matrix-E films at different agarose concentrations can be seen in figure 6.1 (b). Just as for matrix D, the gels were equally conductive within the error limits for all tested agarose concentrations. The conductivity of matrix E at the standard agarose concentration of 2 % employed in this work was determined to $(7.6 \pm 1.4)\,\mathrm{S/m}$. This is a smaller value than the conductivity of the standard matrix D, but strong voltage fluctuations such as for matrix D did not appear. While the deviation from the mean value of the conductivity extends up to 273 % for gel D, the maximum deviation is only about 18 % for gel E (compare figure 6.1 (a) and (b)).
Exposed to heat, matrix D started to melt at 100°C and Matrix E at about 60°C. Above these temperatures the gels thus are not suitable for application.

6.2 Transport measurements

Transport measurements carried out for Co nanoparticles embedded in matrix D revealed high GMR-effect amplitudes of more than 200 %. Against the background of the voltage fluctuations discussed above, however, the derived MR-effect amplitudes vary on the basis of a purely arithmetically point of view depending on

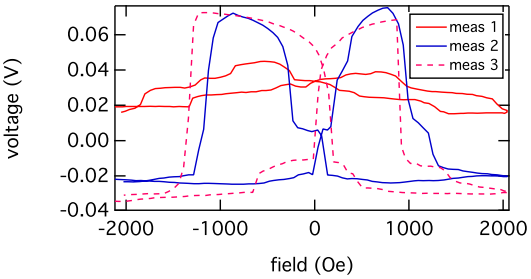

Figure 6.3: The figure displays magneto-transport measurements of Co nanoparticles in matrix D. All three curves come from the same measurement series. As can be seen the baseline voltage strongly fluctuates.

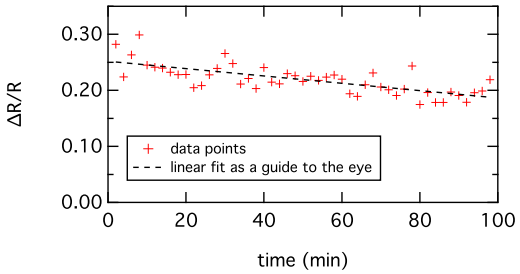

Figure 6.4: The GMR-effect amplitude of a sample of particles in matrix E remains relatively stable over time.

the absolute value of conductivity. Three examples of recorded curves from one measurement series are displayed in figure 6.3. The curves *meas* 1, 2 and 3 were measured in this chronological order, but not directly in succession.
Figure 6.4 illustrates the temporal development of the effect amplitude for Co nanoparticles in matrix E over a period of 100 min. The amplitude fluctuates around a mean effect height of $(21.9 \pm 2.6)\%$. In contrast to matrix A tested in section 5.1 that dried within a few minutes if not sealed air-tight, the GMR effect could be measured over a much longer period of time with only a slight decline of the GMR-effect amplitude. Besides, the reproducibility of GMR-effect height is higher in comparison to the measurements with the sealed gel A (see section 5.1). Since sealing of matrix A eliminates its evaporation, the variations in the effect height, here, can mainly be traced back to the viscosity of the hydrogels that is low enough to allow for a high particle mobility during measurements. In the case of matrix E, a high particle mobility is prevented by its higher viscosity. Compared to matrix D, the GMR-effect height remained relatively stable over time, too. A basic reason for this is a higher voltage stability of matrix E which results from the fact that the amount of water present in matrix E is constant over a longer period of time. All in all, matrix E did show a significantly higher reproducibility of GMR-effect amplitudes than matrix D. In addition, the standard deviation for Matrix E is slightly smaller than the one for matrix A at an even larger mean effect height.
Figure 6.5 shows a transport measurement of a granular system with matrix E with an amplitude of 12 % and the corresponding AGM measurement recorded at room temperature. The hysteresis loop of the global magnetization closely correlates with the MR curve, which is not surprising given that GMR is a direct consequence of

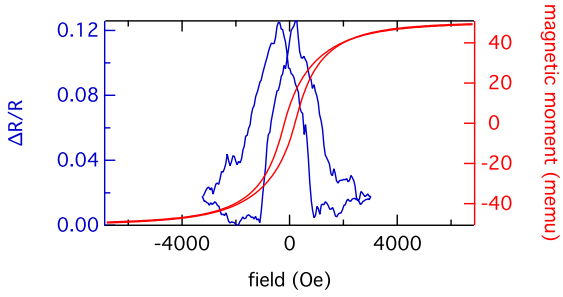

Figure 6.5: A transport measurement of Co nanoparticles in matrix E (blue) and the associated AGM measurement performed at room temperature (red) are shown.

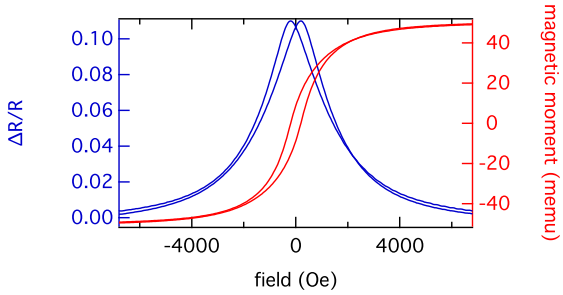

Figure 6.6: Based on the AGM measurement of Co nanoparticles in matrix E, the GMR curve (blue) was calculated using equation 5.4.

the field dependence of the magnetization. The lowest resistivities of the system are realized at the saturation magnetization, where all particles are ferromagnetically aligned. The increasing-field and the decreasing-field branches of the GMR curve correspond to those of the AGM hysteresis loop. It can be seen that the two GMR peaks or, more precisely, the maximum resistances, where the magnetic moments of the particles are in their greatest disorder, are located in the range of the coercive fields of the magnetization curve. Figure 6.6 displays the measured magnetization of the particle-gel sample and the GMR curve derived from the magnetization. For the calculation of the GMR curve non-interacting particles were presumed in order to simplify matters. Under this assumption, the calculation can be performed according to equation 5.4 as already discussed in chapter 5 [89, 102]. For the MR effect amplitude A the measured value of 12% was used. The derived GMR curve resembles the measurement (figure 6.5) quite well. It is apparent, however, that the increasing field branches of the measured GMR curve rise steeper and at smaller field values than the corresponding branches of the calculated curve. This is a result of the couplings between the nanoparticles and nanoparticle clusters in the real system, mediated directly via dipole-dipole interaction, that have been neglected in the calculation. Due to these couplings, the nanoparticles attain a collective behavior and can be saturated easier than non-interacting particles.

6.3 Influence of particle superstructures

Due to their properties fm nanoparticles offer the possibility of specific manipulation via external magnetic fields. This can be used to realize various particle

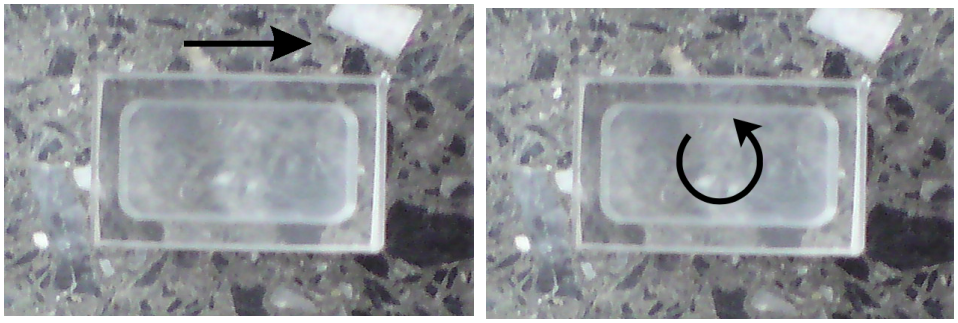

(a) (b)

Figure 6.7: For the creation of particle structures in the sample, the liquid particle-gel mixture is filled in the sample container and an external magnetic field is applied. The arrows indicate the directions of a homogeneous (a) and rotational magnetic field (b).

arrangements in the gel sample. In an external magnetic field, a torque $\boldsymbol{\tau}$ acts on the magnetic moment vector $\boldsymbol{m}$ of a fm particle favoring parallel alignment with the orientation of the external field $\boldsymbol{B}$. The torque is given by

$$\boldsymbol{\tau} = \boldsymbol{m} \times \boldsymbol{B} \ . \tag{6.1}$$

Before the gel is cast, the viscosity of the agarose mixture is low enough to deliberately assemble the nanoparticles by an external magnetic field. After the transition to the gel state, the particles are fixed. Investigations of stability and formation dynamics of dipolar coupled superstructures in microfluidic systems showed that the employment of a rotational magnetic field is suitable for the generation of highly ordered two-dimensional particle layers [106]. According to these findings, a rotational field in a frequency regime of 500 rpm was employed after introducing the nanoparticles in the liquid matrix in order to disperse particles more homogeneously.
Figure 6.8 (a) gives the mean of the measured effect amplitudes for samples with matrix E at a varying agarose concentration. All measurements were carried out for the standard particle concentration and at a fixed position of the contact needles for each sample. With the exception of the 6 %-agarose concentration, a tendency towards higher GMR-effect amplitudes was found for particle-gel samples that had been exposed to a rotation field (rot. field) in contrast to samples where no field had been applied during preparation (no field). The fact that a rotation field did not lead to higher effect amplitudes at the 6 %-agarose concentration might be related to the denser branched agarose net and higher viscosity at an increased concentration preventing high particle mobility and thus the homogenous distribution of the latter.

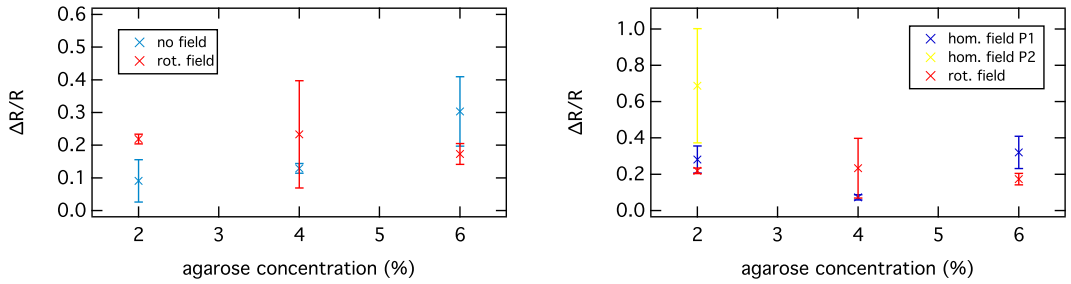

(a) (b)

Figure 6.8: The mean GMR values measured for particle-gel samples at a fixed particle concentration for matrix E at a varying agarose concentration are displayed. Particle-gel samples that have been exposed to a rotation field in a frequency regime of 500 rpm during preparation tend to show a higher GMR effect than samples that have been produced without external magnetic field (a). A further trend towards increased effect amplitudes could be achieved by the application of a homogenous magnetic field (b).

Figure 6.9: Particle-gel samples with matrix E prepared with a homogenous field tend to show higher effect amplitudes. Plotted are the GMR effects versus the particles mass concentration.

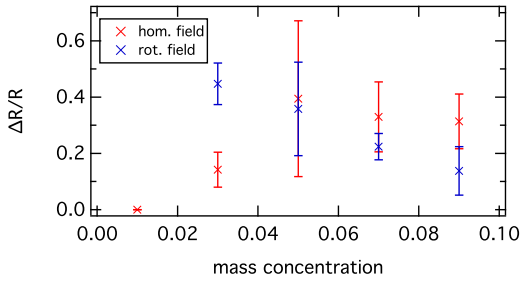

At different positions the variation in effect height for samples treated with a rotation field was found to be neglectable which can be seen as an indication for a homogeneous particle distribution within the matrix. Samples prepared with a homogenous magnetic field, on the other hand, exhibit an uniaxial anisotropy since they contain chain fragments orientated in the direction of the external field. According to the reasons already discussed in section 5.1, samples prepared with a homogenous field tend to show further enhanced effect amplitudes provided that the contact needles are positioned in such a way that the current flows through the Co-chain structures (figure 6.9). However, it might be stated that these samples show a strong variation of the measured effect amplitude depending on whether the contact needles touch a chain or regions in-between. Figure 6.8 (b) exemplarily shows the GMR effect of a sample measured at two different positions. If the needles contact the chains (hom. field P_2), the effect amplitudes exceed by far the effect amplitudes for regions in-between the chains (hom. field P_1). This phenomenon was found for all samples containing chains and is related to the locally varying

particle density. Whenever the contact needles touch the chain structures, there is an increased quantity of magnetic material in the current path which increases the GMR effect amplitude (compare section 5.1.1). MR effects could be measured for mass concentrations between $c = 0.03$ and $c = 0.09$ (figure 6.9) with the maximum values being recorded at a concentration of $c = 0.05$. The maximum here is located at slightly higher concentrations than the maximum of the hydrogels in section 5.1. As already mentioned there, one factor to explain this translation might be the viscosity of matrix E that is higher than the viscosity of the hydrogels. Contrary to matrix E, the hydrogel with the lower viscosity and thus higher particle mobility allows for clustering of particles in the current path in the direction of the external magnetic field which locally increases the mass concentration. The necessary particle density for a GMR effect in the less viscous matrix hence is reached at lower concentrations than for the more viscous matrix E.

6.4 Microstructural analysis

The utilization of electron- and ion microscopes to image gel samples faces the particular disadvantage that they are operated under vacuum which excludes imaging of liquid or water-containing samples. Regarding the investigation of the Co nanoparticles in the gel matrix, this means that the samples have to be dried which, however, presents some difficulties such as shrinkage of the sample volume during evaporation of the liquid and the destruction of the original particle arrangements. In order to circumvent these as far as possible, the sample was freeze-dried which significantly reduces the loss of volume. This technique is based on freezing the material and reducing the surrounding pressure afterwards to enable the frozen water in the material to immediately sublimate from the solid to the gas phase (figure 6.10). Therefore, the sample was immersed in liquid n-propanol which freezes the sample within milliseconds. By contrast, freezing with liquid nitrogen takes much longer and thus favors the formation of ice crystals which destroy the agarose molecules. The frozen sample was then placed inbetween two brass blocks precooled with liquid nitrogen (see figure 6.11 (a)) which guarantee that the sample is kept frozen while it is exposed to vacuum over night.
Figure 6.12 shows two freeze-dried samples of particles in matrix E after transport measurement imaged by a *Keyence VHX-600* optical microscope. In the particle-gel sample prepared without field (figure 6.12 (a)) no chain fragments are visible, but clusters originating from dispersing the particles in the matrix. Note that there are lot of very small superparamagnetic particles in-between the visible clusters that are too small to be visualized by the optical microscope. The measurement of this sample (dotted line in figure 6.13) reveals an effect amplitude of about 10%. When a homogenous magnetic field is applied during preparation, a higher GMR effect of more than 60% is measured. The corresponding sample (figure 6.12 (b)) exhibits clusters and chain structures orientated in the direction of the external magnetic

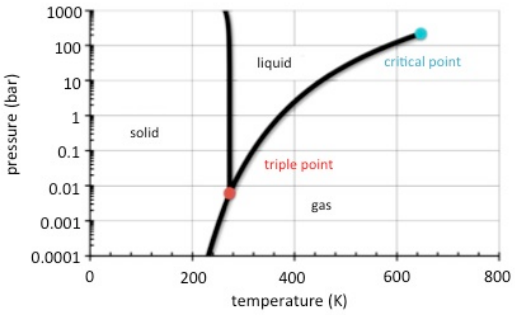

Figure 6.10: In a typical phase diagram, the boundary between gas and liquid runs from the triple to the critical point. Here, the phase diagram of water is displayed. Freeze-drying uses the reduction of pressure near the triple point to bring a system directly from the solid to the gas phase avoiding a liquid-gas transition which normally would take place.

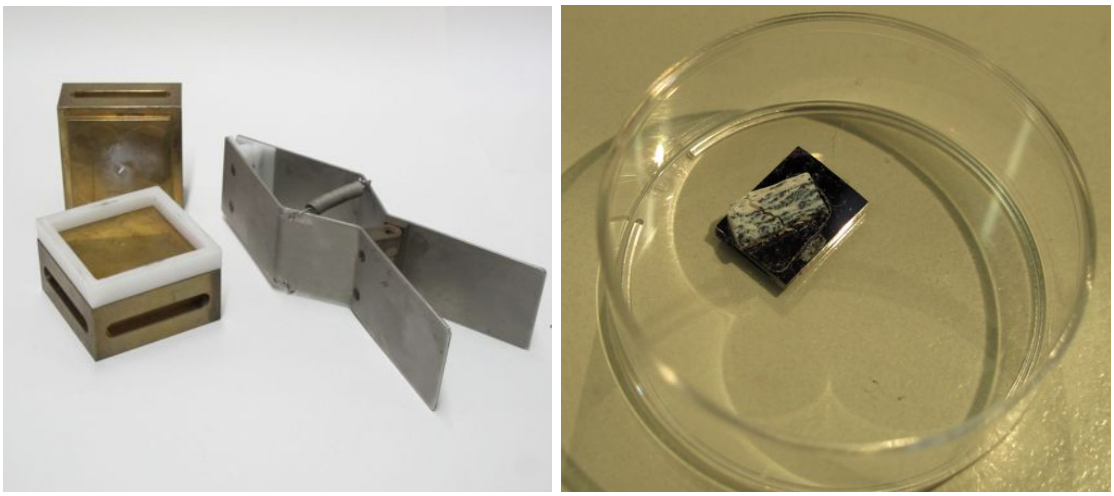

(a) (b)

Figure 6.11: For freeze-drying the specimen is frozen with liquid n-propanol and then placed inbetween two precooled brass blocks (a). The white border is a teflon seal. The whole device is then exposed to vacuum over night. The pliers are used for the transportation of the frozen blocks. A freeze-dried particle-gel sample is displayed in (b).

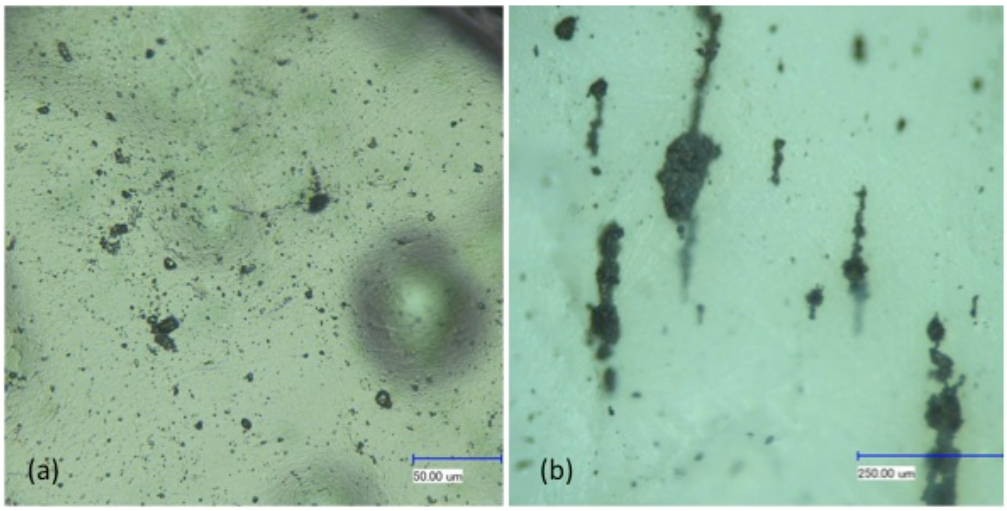

Figure 6.12: Two samples of Co nanoparticles in matrix E after transport measurements are shown. In (a) no magnetic field has been applied during preparation. The visible clusters of nanoparticles originate from introducing the particles in the matrix, but no macroscopic chain fragments can be found. The darker circular structure on the right can be attributed to a bubble included in the gel. Chain fragments and bigger clusters of Co nanoparticles evolved in matrix E when a magnetic field was applied during preparation (b).

field. Again the increase of the GMR-effect amplitude can be associated with an increased spin-dependent scattering along the chains. In the case of both samples, it can be assumed that there exist superparamagnetic nanoparticles finely dispersed in-between the visible structures. Thermal fluctuations prevent the agglutination of those particles that, however, are too small to be visible by optical microscopy. Furthermore, it is interesting to note that there is a difference in the shapes of the GMR curve in figure 6.13 and the figures in section 5.1. The curves of the agarose samples are broader and feature higher saturation fields. This difference may result from the various assemblies of the particles in the varying matrices. Different shapes of the MR curves arise due to coupling between the domains of the magnetic particles [107]. Particles in matrix A remain mobile during transport measurements and by degrees form dipolar coupled chain fragments. In contrast to matrix E, where only single particles and small particle clusters are present (figure 6.12 (a)), those chain fragments can be remagnetized more easily and smaller fields are sufficient to switch their magnetization.

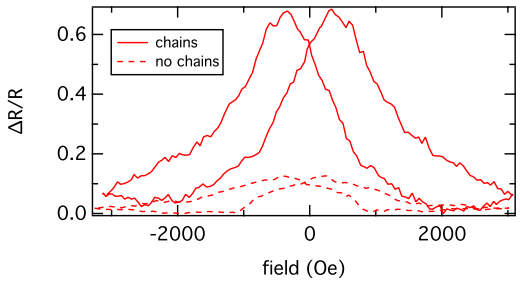

Figure 6.13: GMR measurements of Co particles in matrix E. For the sample with chain fragments (with field) an effect amplitude of more than 60% was achieved, whereas for the sample without magnetic field applied during preparation, no chains evolved and an effect of only roughly 10% was measured.

6.5 Summary

Compared to the matrices tested in chapter 5, both matrix D and E solidify and thus prevent a high particle mobility. This is a necessary quality regarding reproducible sensor characteristics. Additionally, both matrices did not dry as fast as the matrices A, B or C and were thus found to longer maintain their conductivity. Measurement series of more than 1 hour were easily feasible. Regarding application, however, all matrices could additionally be encapsulated or covered with a protective layer against evaporation which would further prolong the measurement time. Matrix D was found to be stable up to 100°C and matrix E to 60°C. Besides, both matrices show a liquid-solid transition which grants the possibility to deliberately arrange the particles within the matrix.
In matrix D strong fluctuations of the baseline voltage were found to produce adverse effects as they inevitably lead to strongly varying GMR-effect amplitudes. Reasons for these variations in conductivity might comprise a varying amount of adsorbed water in the biogel system and its evaporation. The agarose and alginate concentration, on the other hand, did not affect the conductivity within the tested range of concentration (1.5 %-4 % for alginate and 2 %-5 % for agarose). As long as it is not possible to technically control these variations, matrix D seems unsuitable for application. With matrix E an improved reproducibility of the effect amplitudes was achieved based on a higher stability of the ionic conductivity. Due to the strong voltage fluctuations, the effect amplitudes for matrix D reached very high values of more than 200 % at extremely small baseline voltages. For matrix E reproducible effect amplitudes up to 60 % were recorded, which is still very large compared to conventional systems [4, 92, 93].
The creation of particle superstructures in these gels was found to strongly influence the GMR-effect amplitude. This means that these gels do not only offer the key advantage of being structurable by means of the particle arrangement, but they additionally allow to control the GMR-effect height. For a 2 %- and 3 %-concentration of agarose an increased effect height could be attained by samples

that had been exposed to a rotational field in a frequency regime of 500 rpm during preparation which lead to a homogenous dispersion of the nanoparticles [106]. This could not be confirmed for a 6 %-agarose concentration. With increasing agarose concentration, the viscosity of the matrix increases, which is why the agarose net might be too dense to allow for a high enough particle mobility and thus a homogenous particle distribution. A further rise of effect height was reported for the employment of a homogenous magnetic field resulting in the development of particle-chain structures in the matrix.
In conclusion, it can be stated that matrix E seems to be more suitable as a gel matrix for granular systems than the matrices A, B, C or matrix D. While the former do neither offer the possibility of fixing the particles nor creating superstructures within the matrix, matrix D does not offer a stable conductance.

7 Mechanisms of conductance

This chapter addresses the transport mechanisms in the particle-gel samples. Based on the results of the previous chapters, where matrix E has emerged as the most promising candidate for application, most of the measurements are performed for the latter. First, the conductance of pure gel is investigated by current-voltage characteristics. Electrolysis effects are apparent and are further examined by electric stress measurements. The suppression of electrolysis in the matrix is essential in regard to transport measurements and possible solutions are discussed. Furthermore, this chapter deals with the question to what extend conductance changes when particles are introduced into the matrix. As revealed by IV characteristics, ion migration plays a key role in the conduction process of the gel matrix. Additional studies are performed at low temperatures, in order to gain a deeper understanding of the conductance in the particle-gel system and to separate ionic from electronic conductivity.

7.1 Ionic conductivity in electrolytes

The term liquid electrolyte refers to solvated ions in an aqueous solution [108]. The ions are subject to the strong attraction of the solvent molecules and, unlike a rigid ionic lattice, the coulombic cohesive forces are overcome. The resulting ionic solution has the ability to conduct electricity by the drift of ions. If a voltage is applied to the solution via two electrodes as illustrated in figure 7.1 (a), the generated potential difference acts on the charged particles in such a manner that the cations (K^+) of the electrolyte start to migrate to the cathode and anions (A^-) to the anode. The ions accumulate at the electrodes and so-called *electrical double layers* are established. The double layers consist of two parallel layers of charge surrounding the electrode (figure 7.1 (b)). Directly at the phase boundary electrode-electrolyte the Helmholtz layer is developed which comprises ions of equal and opposite charge adsorbed onto the electrode due to chemical interactions. This interface behaves much like a parallel plate condensator. A second layer called Gouy-Chapman- or diffuse layer is located inbetween the Helmholtz layer and the bulk electrolyte. It is composed of free ions that are drawn to the surface charge via the coulomb force and are exposed to thermal motion. Both Helmholtz and Gouy-Chapman- layer can also be subsumed under the name Stern-double layer. The electrical potential Φ in the solution decreases exponentially with the distance according to [108]

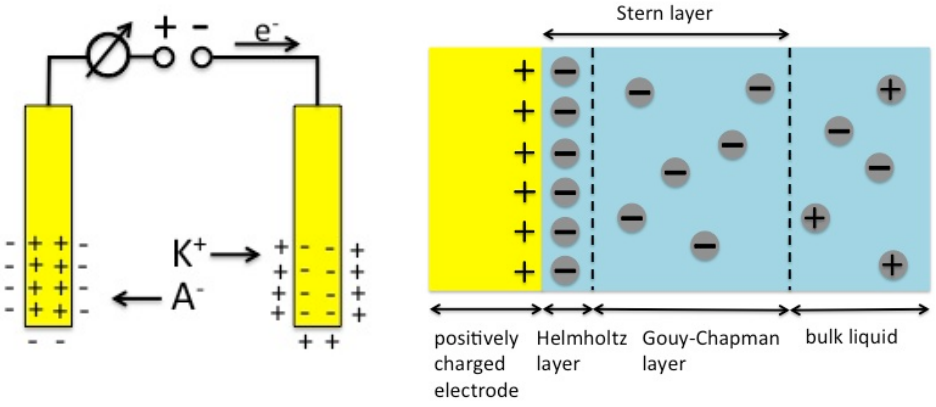

(a) (b)

Figure 7.1: If a voltage is applied to a liquid electrolyte, cations (K^+) start to migrate to the cathode and anions (A^-) to the anode (a). The ions accumulate at the electrodes and generate the so-called electrochemical double layers (b). A current is induced in the measuring circuit.

$$\Phi = \zeta \cdot \exp\left(-\frac{x}{\lambda_D}\right) , \tag{7.1}$$

where ζ is the potential determined by the adsorbed ions at the surface and x the distance from the electrode. λ_D is the Debye length, i.e. the characteristic length scale over which the charged surface is shielded from the bulk by mobile charge carriers in the electrolyte. It thus represents the characteristic thickness of the double layers and depends on the mean diffusion coefficient D of the ions, the electrical permittivity ϵ of the electrolyte and the conductivity σ according to [109]

$$\lambda_D = \sqrt{\left(\frac{D\epsilon}{\sigma}\right)} . \tag{7.2}$$

Typical values are few nanometers. The electrons in the metallic electrodes respond to the electric field arising from the charging of the electrolyte side of the phase boundary. Further ions attracted by the electrodes get oxidized and reduced, respectively. Thus, ion migration in the electrolyte induces an electron flow in the electrodes, which can be recorded in an external measuring circuit.
The basic equation to describe the process of conductance is

$$\sigma = qn\mu \tag{7.3}$$

where q is the charge, n the concentration and μ the mobility of the charge carriers. The temperature dependence of ionic conductivity generally obeys Arrhenius behavior, which mathematically is represented by [110]

$$\sigma = \sigma_0 \cdot \exp\left(\frac{-E_a}{k_B T}\right) \tag{7.4}$$

with σ_0 a preexponential factor, E_a the activation energy and k_B the Boltzmann constant. The statistical mechanical interpretation of that equation is that the mechanism of ion transport is a thermally activated process with an energy barrier of size E_a that must be overcome for ionic conduction to occur.

7.2 Current-voltage characteristics of gel

7.2.1 Linear sweeps

IV characteristics of pure matrix E were recorded in order to examine its behavior in an electrical circuit more closely. The description of the experimental setup can be found in subsection 4.3.
The red curve in figure 7.2 (a) corresponds to a measurement sweep where an applied voltage was increased stepwise by 0.05 V starting from -2 V up to +2 V. The measurement time steps were 270 ms. The blue curve is the result of a measurement that was started at zero voltage and only half of the sweep was run. It is striking that both curves exhibit a non-linear behavior. Starting from -2 V the absolute value of the current flow decreases with voltage, crosses zero at -0.7 V and is non-zero at zero voltage. For a further increase of the applied voltage, the current starts to flow in the other direction and its absolute value increases again. Besides a local maximum located at about 0.1 V, a plateau can be found at about 1 V. Sweeps that start at zero voltage (blue line), on the other hand, show no current flow at zero voltage. The first peak is missing, but the plateau at 1 V is visible.
The observed non-linear behavior resembles typical current-potential curves of electrolytes [111]. From a chemical point of view, the salts contained in the buffer form an ionically conducting solution in the polymer matrix. Agarose itself, on the other hand, is a molecule known to be stable (for more information see section 3). Furthermore, it can be assumed that the electrodes do not dissociate since they are both made of gold and thus a nobel metal.
Additionally, gold electrodes are known to be highly polarizable. If a voltage of -2 V is applied, one electrode becomes the cathode (-) and the other one the anode (+). Negatively charged ions contained in the gel such as the acetate ion CH_3COO^-, start to migrate in the direction of the anode and positively charged ions such as

H_3O^+ in the direction of the cathode. Besides the acetates of the TAE-buffer, further ions might be derived from the tris of the buffer (compare section 3.2.5) that to a certain extend might exist protonated. The ions accumulate at the electrodes, where the electrical double layers are established [108]. Ion migration in the electrolyte always corresponds to an electron flow in the electrodes and thus a discharge current can be recorded in the measuring circuit. According to the principle of superposition, all types of ions contribute to this process [112]. If the applied voltage is decreased, ion migration decreases and so does the absolute value of the current. When the external voltage approaches -1 V, the voltage becomes too small for a discharge current. At -0.7 V there is no current flow. The electrical double layers then start to decompose which leads to a current flow in the opposite direction and a broad peak around 0.1 V. At zero volt there is a non-zero current. In addition, the polarity of the electrodes is reversed at this point and ion migration starts in the opposite direction. When the voltage is increased, the current flow enhances and saturates at 1 V. A possible explanation for this plateau is that the concentration of salts, i.e. reducible or oxidizable ions near the electrodes has strongly decreased which is known as electrolyte depletion [113]. It is not before 1.5 V that a further increase of voltage leads to a rise in the current. At this point, the energy provided by the electrodes might be high enough to allow for the ionization of additional types of ions that now are available for reduction and oxidization, respectively, or to recharge the depleted layer with ions from the bulk electrolyte.
When the sweep starts at zero voltage (blue line), on the other hand, there is no current for zero voltage. As the specimen has not been stressed before, the system is in electrical equilibrium when the voltage is applied. The current hence does not start to rise before the voltage is increased and ion migration starts. The characteristic peak at 1 V, however, can be found at the same position as before and might be explained by the same argumentation.
The most evident proof of ionic conductance is the detection of electrolysis and electrolysis products, respectively. If voltages of 3V and higher were applied to the gel, electrolysis became obvious which manifested itself in a discoloration of the electrolyte close to one of the two electrodes as well as gas formation (bubbles).
Figure 7.2 (b) displays the IV characteristic for the gel with Co nanoparticles. The same measurements as for the pure gel were carried out. There is also a current at zero voltage for the sweep that starts at -2 V and no current if the sweep starts at zero voltage. The shape of the curves of the particle-gel sample, however, differs from the curves of the pure gel. No pronounced features are visible in figure 7.2 (b). This can be explained by the fact that conductivity is strongly increased by the introduction of Co nanoparticles. As a result conduction waves are hidden and not apparent in the graph.

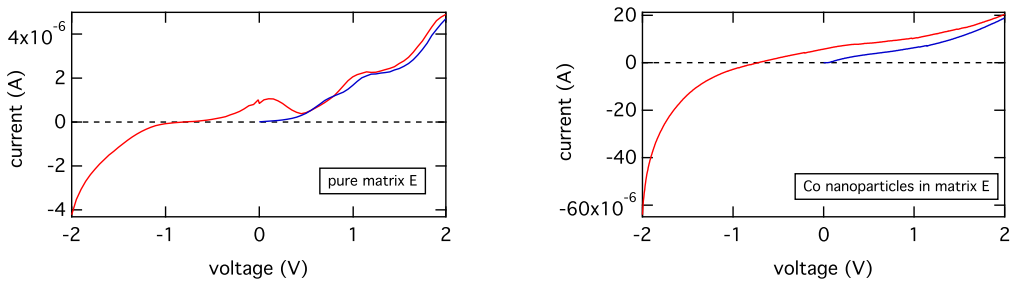

(a) (b)

Figure 7.2: IV characteristic of a sample of pure matrix E (a) and a sample of Co nanoparticles in matrix E (b). When the sweep is started at -2 V a current is measured for zero voltage (red lines) due to a prestressing of the gel. This is not the case if the measurement sweep is started at zero voltage as the gel has not been stressed before (blue lines).

7.2.2 Cyclic sweeps

The next step was to apply a triangular shaped potential (upper part of figure 7.3) as excitation signal in a cyclic manner to the gel samples in order to test whether the electrochemical processes in the matrix are symmetric and reversible. The lower part of figure 7.3 displays the resulting plot for a gel-E- and figure 7.4 for a gel-D specimen as reference. Contrary to the procedure for the linear sweeps, the voltage is scanned starting from 0 V in forward direction in 50 mV steps up to the maximum potential of 2 V. Then, the sweep is reversed and the voltage is decreased down to the minimum potential of -2 V. Finally, the voltage is increased again to 0 V. This cycle is run several times. The voltage dependency of the current shows a hysteresis, which is reproducible as indicated by plotting subsequent cycles on top of each other.
Figure 7.5 shows a little bit more than one cycle for gel E. The curves exhibit 4 peaks labeled in the graphic. At the start at zero voltage no current flow is measured. The gel and the salts of the buffer, more precisely anions and cations are in equilibrium. With increasing voltage the ions start to migrate and a discharge current flows. At a voltage of about 1.1 V the current begins to saturate, just as it was the case for the linear sweeps, resulting in the plateau *wave 1* in the voltammogram. With further increase of the voltage the current rises again. At 2 V, the potential sweep is reversed. With decreasing voltage the current flow diminishes. When the voltage is low enough, ion migration stops and the current flow vanishes. As already discussed for the linear sweeps, we now have a predominant negative charge distribution around the still negatively charged electrode and vice versa for a short period. The double layers start to decompose and the system relaxes back to equilibrium. There is a current pulse in the opposite direction and plateau (*wave 2*) arises. At zero potential, however, the polarity of the voltage

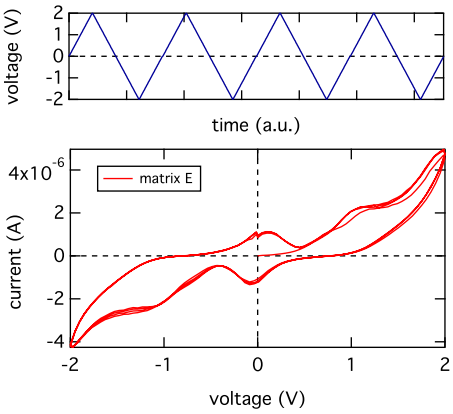

Figure 7.3: A triangular-shaped time-dependent potential (upper part of graphic) is applied in a cyclic manner to a sample of matrix E. To illustrate reproducibility several cycles were run and plotted on top of each other (lower part of graphic).

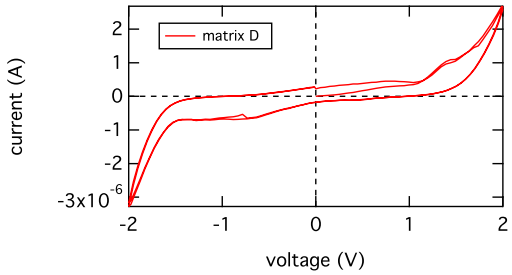

Figure 7.4: A triangular-shaped time-dependent potential is applied in a cyclic manner to a sample of matrix D. Several cycles were run and plotted on top of each other.

has been reversed. In the first place, this leads to the drop of *wave 2*, then, to an increasing current. Further decrease of the voltage leads to *wave 1a* at -1.1 V and we also find a plateau *wave 2a* when we increase the voltage. *Wave 1* and *wave 1a* as well as *wave 2* and *wave 2a* are point symmetric to the origin. The recorded cycles for the gel D are also nonlinear, but the waves are found to be less pronounced. The maximum current obtained at 2 V is about 25 % smaller for gel D than for gel E. The curves of both gels are highly symmetric and reproducible indicating that the chemical processes that take place at the electrodes are reversible.

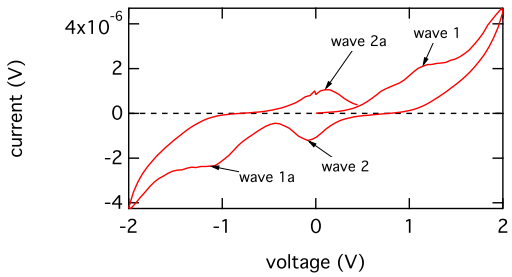

Figure 7.5: A triangular-shaped time-dependent potential is applied in a cyclic manner to a sample of matrix E. The recorded curves are nonlinear with plateaus (waves) at ±0.1 V and ±1.1 V.

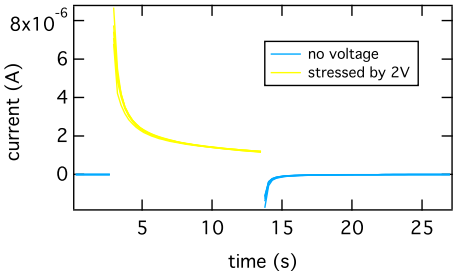

Figure 7.6: After about 3 s of zero voltage (blue), pure matrix E is stressed by a voltage of 2 V (yellow). Finally, the voltage is switched off and the behavior of the system is observed by recording the post-current (blue). In this plot multiple measurements are plotted on top of each other to indicate reproducibility.

7.3 Stressing of gel

The behavior of matrix E under a constant voltage was further analyzed by electric stress measurements. After a pre-measurement of 3 s duration at zero voltage, a stress voltage was applied for about 11 s. Afterwards, the bias was switched off and the behavior of the system was observed by post-measurement of the current. The measurement steps were 270 ms. Figure 7.6 shows the recorded current for a stress voltage of 2V (yellow). When the stress voltage is applied, there initially is a current pulse. The current then slowly decreases until it reaches a saturation value. When the bias voltage is switched off, a negative current pulse is observed followed by a decrease of the absolute value and a saturation at zero current. This behavior is reproducible as indicated in figure 7.6 by plotting 5 measurements on top of each other. The measurement process described above is carried out for stress voltages from zero to 2 V. The corresponding plots can be seen in figure 7.7 (a). Subfigure (b) displays the measurements under stress on an extended scale. Immediately after switching on the stress voltage, drift-related ion transport starts. As already discussed, the negatively charged ions such as CH_3COO^- migrate to the anode and the positively charged ions such as H_3O^+ to the cathode. A positive current pulse is observed in the measuring circuit. The electrochemical double layers developed at the respective electrodes act as a counter-voltage to ion migration and finally lead to the saturation of the current. For all voltages tested the transient time scale was less than 9 s. The temporal development of the current under stress could numerically be fitted by an exponential function with moderate quality

$$I(t) = I_{sat} + \Delta I \cdot \exp\left(\frac{-t}{\tau}\right) \tag{7.5}$$

where I_{sat} is the current in saturation, ΔI the proportional constants with $\Delta I = I(0) - I_{sat}$ and τ the decay time. Figure 7.8 (a) exemplarily displays the fitted data

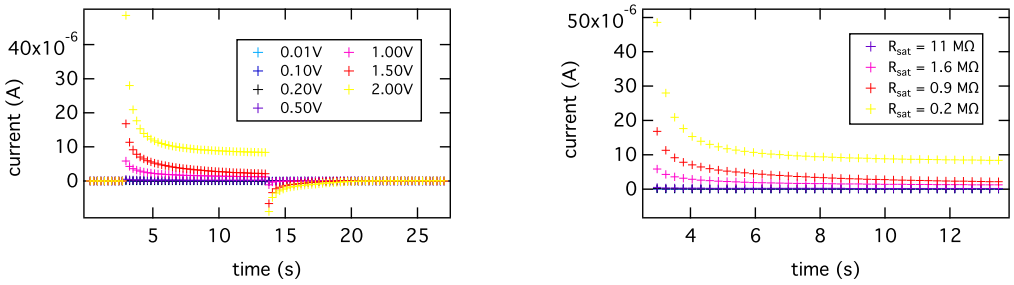

(a) (b)

Figure 7.7: After a pre-measurement of 3 s duration with zero voltage, a stress voltage is applied to pure gel E for about 11 s. The development of the current and the subsequent relaxation is plotted over time for different stress voltages (a). Subfigure (b) displays the part of the measurement under applied stress voltage. For 0.5, 1.0, 1.5 and 2 V the resistances in saturation are given (for the color coding see subfigure (a)).

voltage [V]	0.5	1	1.5	2
τ [ms]	988 ± 85	1206 ± 74	1195 ± 93	511 ± 29

Table 7.1: An electrical stress voltage was applied to matrix E. The temporal development of the current was fitted by an exponential function. The table summarizes the decay constants τ.

for a stress voltage of 2 V. The decay constants revealed for stress voltages between 0.5 and 2 V are summarized in table 7.1.

When the bias voltage is switched off, the charges built up at the electrodes cause the electric field to change direction. The current reverses as the ions relax back to their equilibrium positions. The degradation of the electrochemical double layer manifests in a negative current pulse (compare figure 7.8 (b)). When the counter-voltage has been removed, the current flow grinds to a halt. This relaxation occurs on a shorter time scale of less than 6 s.
The observed behavior of the current waveforms is in agreement with literature about the effects of time-varying electrical fields on the development of electric double layers [114]. According to Sato and Morrow [112, 114], the current induced by the motion of charged particles is a result of the superposition of the contributing particles. It can accurately be described by the Morrow-Sato equation which yields the true total external current due to a voltage applied to an electrolytic solution. For the approximation of small gaps of size d between the electrodes with a cross-sectional area of $A \gg d^2$, the Morrow-Sato equation is given by [114]

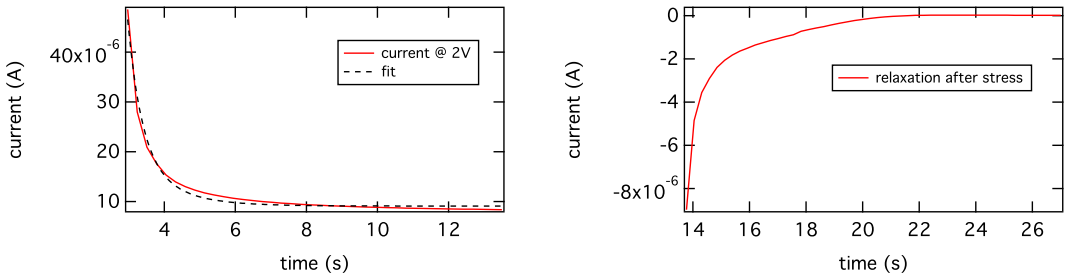

(a) (b)

Figure 7.8: The development of the current in the agarose gel is displayed under a constant stress voltage (a) and after the stress voltage has been switched off (b).

$$I = \frac{A}{d}\left(e\int_0^d \left[\rho_\mathrm{p} v_\mathrm{p} - \rho_\mathrm{n} v_\mathrm{n} + D_\mathrm{p}\frac{d\rho_\mathrm{p}}{dx} - D_\mathrm{n}\frac{d\rho_\mathrm{n}}{dx}\right]\mathrm{d}x + \epsilon_r\epsilon_0\frac{dU}{dt}\right). \tag{7.6}$$

Here, $C = \frac{A\epsilon_r\epsilon_0}{d}$ is the capacitance neglecting fringe effects, ϵ_r the relative and ϵ_0 the vacuum permittivity, e denotes the elementary charge, t the time, U the applied voltage between the two electrodes and x the distance from the respective electrode. D is the diffusion coefficient, ρ the number density and v the drift velocity, where the index p indicates positive and n negative charge. The drift velocities differ depending on the mass of the particles and hence are not necessarily the same for the anion and the cation of a redox pair.
For all stress voltages tested, it can be assumed that the saturation current and thus a constant resistance is reached after 9 s. For voltages below 0.2 V no significant current pulses were noticeable. A constant current flow is desirable regarding transport measurements. The transient response current therefore can be suppressed by either avoiding voltages higher than 0.2 V or, if higher voltages are applied, by allowing a time period of at least 9 s to expire before measuring.

7.4 AC conductivity

Observed electrolysis effects in the gel matrix as well as effects related to the enrichment of a specific ion type at the electrodes result in a conductivity difficult to control and are undesirable during transport measurements since a change of conductivity on the chemical level might hide the specific MR signal. According to the stress measurements a first solution is to perform the transport measurements in low voltage and current ranges, respectively. Currents of about 5 µA were thus

used for the transport measurements in this work. Additionally, it was tested to use AC in order to weaken electrolysis in the matrix. As a first step an alternating current was generated computer-operated by applying a voltage sequence. Starting from zero, the voltage was increased up to 2 V in steps of 50 mV and time steps of 270 ms. The positive voltage was always followed by the corresponding negative value (0, +50 mV, -50 mV, +100 mV, -100 mV, ...). The resulting characteristic for matrix E (blue markers in figure 7.9) is clearly different from the DC curve (red line). While the DC curve exhibits the typical waves in the voltage dependency of the measured current, the AC-curve, on the other hand, is symmetric to the origin and reduction waves are suppressed.

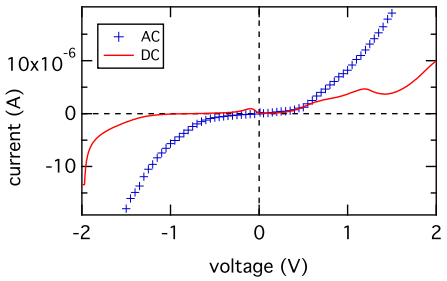

Figure 7.9: The IV characteristic of pure gel E was recorded for DC and AC. Electrolysis effects that occurred for DC (red line) could be suppressed by the use of AC (blue markers).

The electric field in the bulk electrolyte depends on the frequency of the applied electrical field owing to electrode polarization [109]. Alternating the polarity of the electrodes periodically at a timescale shorter than the timescales on which the depletion of the ionic charge carriers at the electrodes occurs, ensures a level-playing field in terms of charging of the diffusive layer. Netto electrolysis effects such as depletion plateaus are hence suppressed in the IV characteristic. The characteristic frequency here is the so-called charge relaxation frequency $f_c = \frac{1}{2\pi}\frac{\sigma}{\epsilon}$ with σ the conductivity and ϵ the electrical permittivity of the electrolyte, which is usually about ~ 1 MHz [115]. Using AC with frequencies below f_c guarantees that the ions at the electrode-electrolyte interface have sufficient time to induce charge accumulation in the diffuse double layer and the applied potential is dropped across the latter. At higher frequencies approaching the charge relaxation frequency, on the other hand, the potential changes that fast that the double layer does not have enough time to form. The double layer impedance thus becomes negliable and the total electrolytic impedance is dominated by the impedance of the bulk. Measurements dealing with the AC conductivity can be found in section 8.2.

7.5 Electronic and ionic contribution

7.5.1 Conductivity in particle-gel samples

AC-IV characteristics as described in section 7.4 are carried out at room temperature for pure matrix E and particle-gel specimens. The voltage is varied from

−1.5 V to 1.5 V in steps of 50 mV. Typical plots obtained for a pure gel and a particle-gel sample can be seen in figure 7.10 (a). The measured particle-gel sample contained chains that had been formed by applying a constant homogenous magnetic field during sample preparation. The behavior of the pure matrix E is obviously non-linear. The behavior of the sample with particles, on the other hand, seems to be nearly ohmic. Since the change of current is very small, the first derivative of the current with respect to the voltage (differential conductance) ($\mathrm{d}I/\mathrm{d}U$) is plotted versus the voltage to display the conductance more illustratively (figure 7.10 (b)). As can be seen, the differential conductance of the sample with particles (blue curve) exceeds the conductivity of the pure gel (red curve) by about two orders of magnitude. For that reason we can assume that, at room temperature, nearly the whole electric current flows through the particles in this sample. The almost ohmic behavior of the particle-gel sample is confirmed by its virtually constant differential conductance. Note that this is in contrast to IV characteristics of other particle-gel samples described later in section 7.5.2, where the curves of the particle-gel samples are also non-linear. The linearity of the particle-gel sample here can be explained by the chains in the sample that lead to a higher fraction of electrically conducting Co in the current path and thus increase the contribution of electronic conductivity.

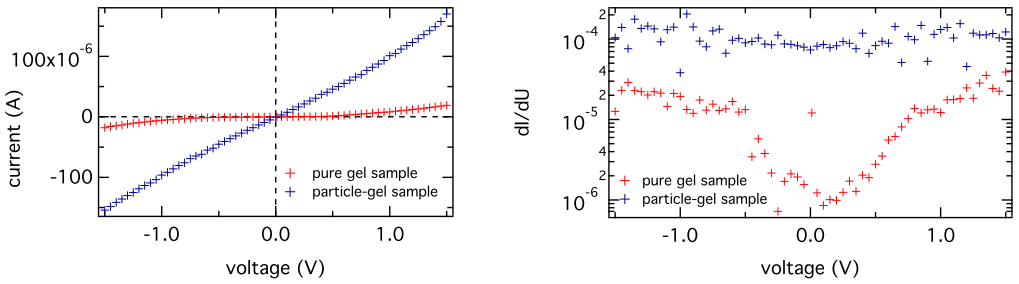

Figure 7.10: IV curve of pure matrix E (red) and matrix E containing Co particles (blue) are recorded by a quasi AC measurement (a). The derivative of the current is plotted logarithmically versus voltage (b).

7.5.2 Temperature dependence of conductivity

Experimental setup

In order to examine the kind of conductivity and the transport mechanism in the sample more closely, IV characteristic measurements at low temperatures were performed using a closed-cycle-Helium cryostat (*Oxford Cryodrive 1.5*) with a temperature range of 13 K to 330 K. This setup allows to precisely set the temperatures

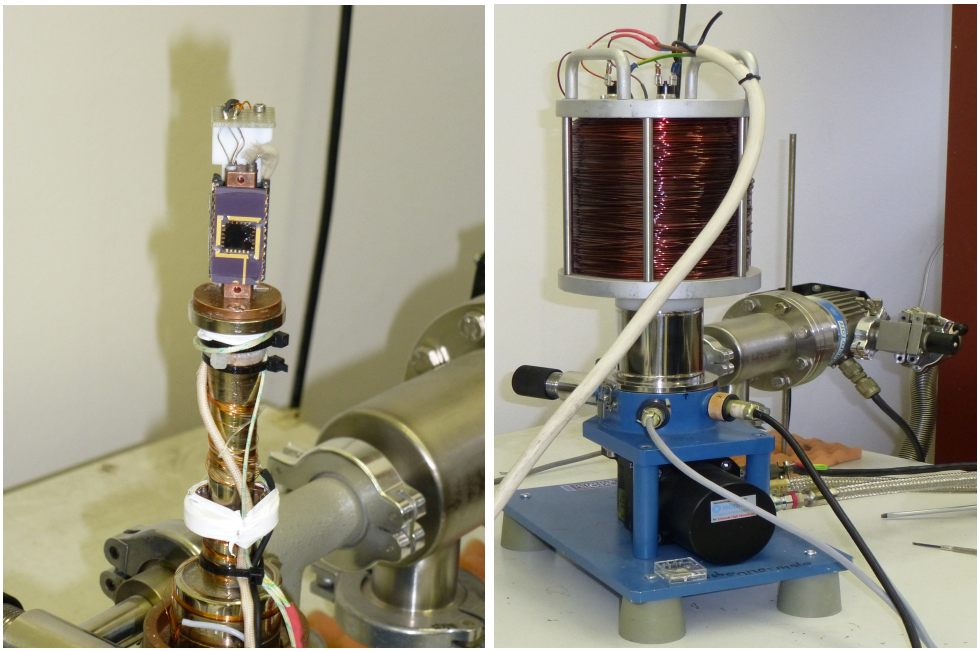

(a) (b)

Figure 7.11: Subfigure (a) shows the chip carrier with the sample placed in the closed-cycle-Helium cryostat. The sample is then covered with a radiation shield and the outer housing. Finally, a solenoid is placed on top of it (subfigure (b)).

in a controlled manner. Since the cryostat operates with the sample being in a vacuum chamber, air-tight sealing of the gel is required. Therefore, the gel-specimen under investigation is filled in a modified chip package as described in section 4.1.1. A glass lid is glued on top of the chip package and high vacuum grease is used to seal it gas-tight. The whole device is then placed in the cryostat as pictured in figure 7.11 (a). Having closed the cryostat with a radiation shield and the outer housing, a custom-built solenoid with a maximum field of 2000 Oe is placed on top of it (figure 7.11 (b)).

Measurements

Starting at 302 K a sample of Co nanoparticles in gel E is cooled down to 245 K. In steps of 2 K the IV characteristic is measured for both DC and AC. As already described previously, the AC measurements are carried out by applying a voltage sequence computer-operated. For each temperature, the voltage is increased from zero V up to 2000 mV in steps of 50 mV with always a positive voltage followed by the corresponding negative value (0, +50 mV, -50 mV, +100 mV, -100 mV, ...). Afterwards, the temperature of the cryostat is increased stepwise from 245 K to 302 K while measurements are carried out in the same manner.

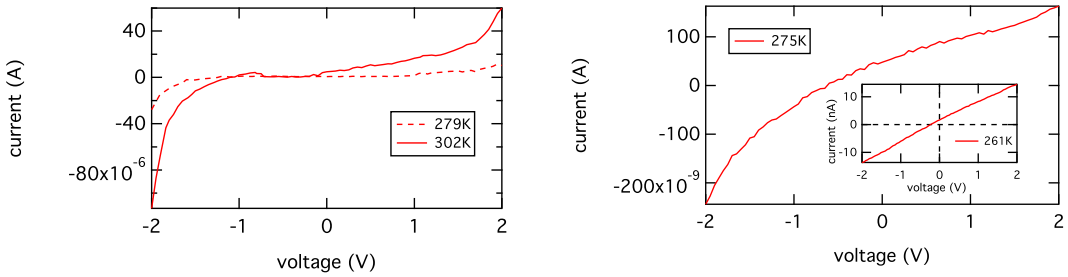

Figure 7.12: IV characteristics recorded with DC during cooldown are shown. Starting from 302 K the curves are clearly non-linear and feature a sharp rise of the current at about 1.8 V (subfigure (a)). Current and curvature decrease with temperature. At 275 K the form of the curve has clearly changed (subfigure (b)) and is nearly linear at 261 K (inset of subfigure (b)).

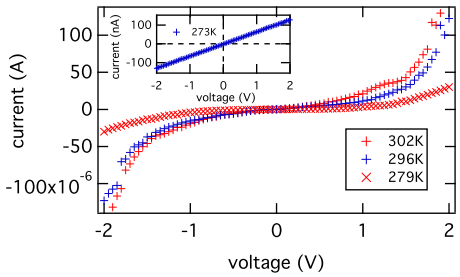

Figure 7.13: The IV characteristics for the AC cool down is shown. While the characteristic is non-linear at 302 K, 296 K and 279 K, it has become ohmic at 273 K.

The recorded IV characteristic at 302 K for the DC measurement is clearly non-linear (figure 7.12 (a)). As already discussed this is an indication of ionic conductivity. Since the system investigated here contains Co nanoparticles, an electronic contribution cannot be excluded. The ionic contribution, though, can be assumed to constitute the main part of the conductance mechanism due to the non-linearity of the measured curves. The recorded characteristic seems to be in contrast to the recorded trace of the particle-gel sample in subsection 7.5.1 that behaves nearly linear. The observed difference can be explained by the fact that both the actual particle concentration and the particle arrangement in the matrix vary slightly due to manufacturing tolerances. The specimen considered in subsection 7.5.1 must have had a higher nanoparticular volume density of Co in the current path which lead to an increased electronic contribution to conductance and thus a linearization of the IV curve.

At 302 K the current rises sharply with voltage as depicted in figure 7.12 (a). Both current and curvature decrease with decreasing temperature. At a temperature of about 275 K the voltage is no longer sufficient to create such a strong increase of the current as was achieved at higher temperatures (figure 7.12 (b)). Though, the

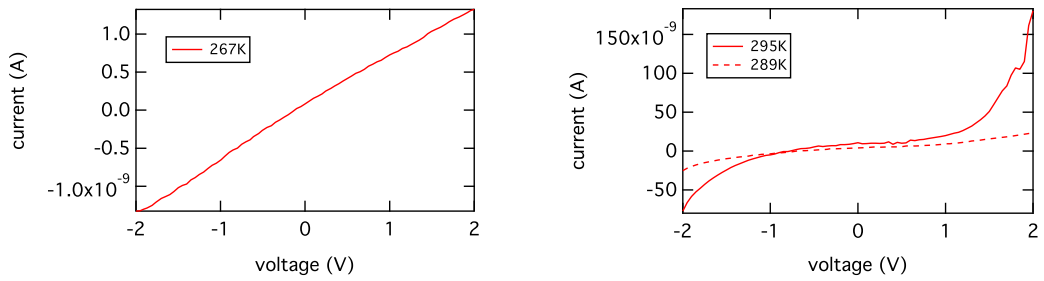

(a) (b)

Figure 7.14: The IV characteristic for DC was recorded during the warm up. While the characteristic is still linear at 267 K (a) it becomes non-linear at 289 K (b).

characteristic is still non-linear. When 261 K is reached (inset of figure 7.12 (b)), the curve has become nearly linear with a non-zero current at zero voltage. The same behavior was found for AC except that electrolysis effects are suppressed which, as already pointed out, leads to characteristics that are symmetric to the origin. Starting from the non-linear behavior at 302 K, the current and the slope of the AC characteristic decrease with decreasing temperature as can be seen in figure 7.13. Between 277 K and 275 K the IV characteristic becomes ohmic. The characteristic at 273 K is shown in the inset of figure 7.13. It is linear and crosses the origin. Warming up the cryostat, the linear IV characteristics of both DC and AC measurements reach their original non-linear form between 287 K and 289 K when the ion mobility has been restored. Examples of the recorded characteristics for DC and AC are displayed in figure 7.14 and figure 7.15, respectively.

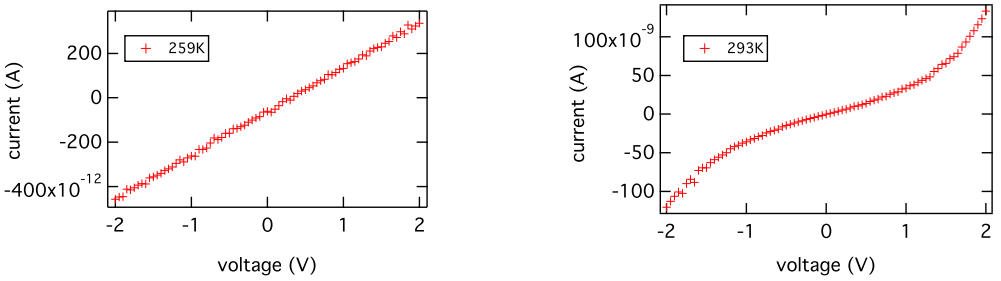

(a) (b)

Figure 7.15: The IV characteristic of the Co particle-matrix-E sample for AC was recorded during the warm up. Shown is the plot for 259 K (a) which is linear and the plot for 293 K which has become non-linear again (b).

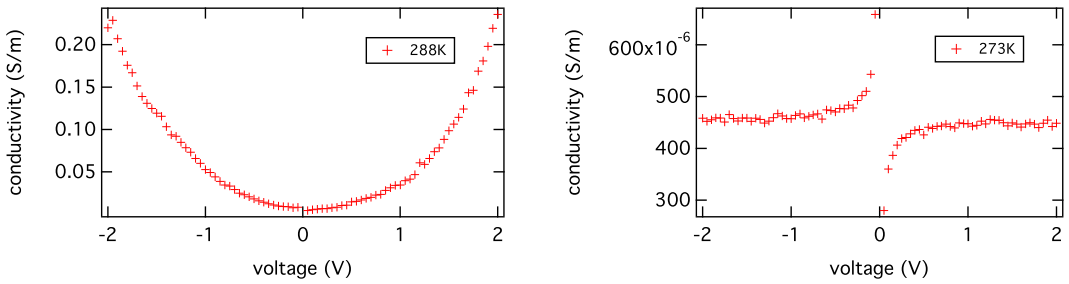

(a) (b)

Figure 7.16: The calculated conductivity of the Co particle-matrix-E sample is plotted versus voltage for 288 K (a) and at 273 K (b).

Evaluation

Based on the IV characteristics, the conductivity was calculated using formula 4.3 (see section 4.2). Typical plots of the conductivity for AC measurements can be seen in figure 7.16. Since the conductivity mathematically equals the derivative of the IV curve, the non-linear IV characteristic at 288 K results in a parabola (subfigure (a)). The ohmic characteristic at 273 K yields a conductivity as displayed in subfigure (b). It is constant sufficiently far away from zero V. At zero V it features a so-called zero bias peak, which is a mathematical artefact attributed to the division by small voltage values in the conductivity calculation. The conductivity at a voltage of 1700 mV was chosen to examine the temperature-dependency of the conductivity of the sample, (figure 7.17 (a)), in order to avoid a distortion by the influence of the zero bias peak. For both DC and AC, the conductivity clearly declines for lower temperatures. Located near the temperatures where the IV curves change their non-linear characteristic, kinks in the conductivity-versus-temperature graphs can be found. It is striking that the conductivities during the warm up are lower than during the cool down. Since the elapsed time span between the collection of data at different temperatures was chosen long enough to guarantee thermal equilibrium of the system, it can be excluded that this is due to an offset in temperature. In fact, this decrease in conductivity might rather be traced back to evaporation of water in the gel over the duration of measurement or destruction of gel structures due to the stress of freezing. Figure 7.17 (b) illustrates the current of the AC measurement at 2 V. At the turning point towards ohmic conductance the current drops dramatically. At 260 K it is only a few nano ampere and thus has become three orders of magnitude smaller.
Figure 7.18 (a) displays the natural logarithm of the calculated conductivity plotted versus the reciprocal temperature for the particle-gel sample. Implying ionic conductance, the natural logarithm of conductivity versus the reciprocal of temperature should result in a linear graph with a slope given by the activation energy of the process according to equation 7.4. Indeed, the left side of the plot, which

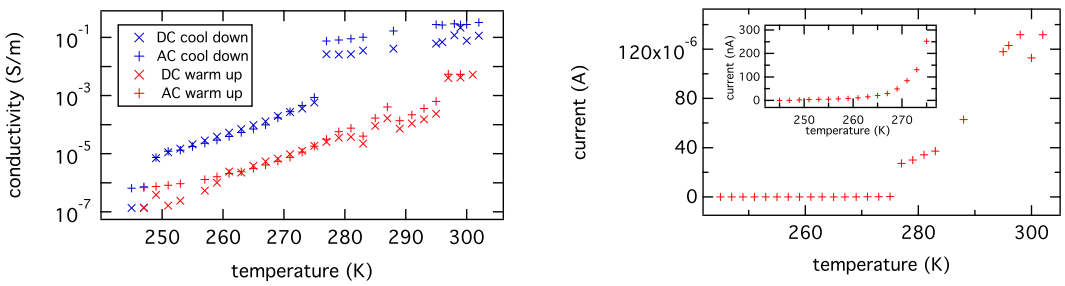

(a) (b)

Figure 7.17: Subfigure (a) displays the conductivity of the Co particle-matrix-E sample versus temperature for both AC and DC during the cool down and the warm up, respectively. Subfigure (b) illustrates the current at 2 V in dependency on the temperature. In the inset the current for temperatures below 277 K are plotted on an extended current scale.

corresponds to temperatures higher than 277 K, could be fitted linearly (7.18 (b)) with moderate quality, which yielded an activation energy of (452.7 ± 24.1) meV. There is a vast literature published on ionically conducting polymer electrolytes and their activation energies revealed according to Arrhenius [116–121]. Alias et al., for instance, investigated agar polymer hosts with NH_4I- and I_2 salts. The revealed activation energies range from 240 meV to 300 meV at comparable conductivities ranging from roughly $5 \cdot 10^{-2}$ S/m to 0.1 S/m [116]. Rozali et al. determined the activation energies of polymer electrolytes based on carboxy methylcellulose with different concentrations of salicylic acid to 400 meV up to 500 meV at conductivities ranging from about $1 \cdot 10^{-7}$ S/m to $1 \cdot 10^{-5}$ S/m [117]. It has to be noted that our system in contrast to the systems just mentioned contains metallic and thus electrically conducting nanoparticles. Yet, as already stated previously, the ionic conductance dominates above the freezing temperature of the gel. Moreover, electronic conductance alone is not sufficient for the transport mechanism since dried samples are no longer conductive (compare section 5.1). Having taken these factors into account, it can be said that the obtained activation energy for our system is positioned within the framework of values for ionic systems of comparable polymer electrolytes.

More precisely, the Arrhenius equation is indeed well applicable to ionic crystals and electrolytes where the solvent molecules are locked into a fixed orientation, such as polymer electrolytes below the glass transition temperature, but it only approximately describes the conductivity of amorphous electrolytes and gel electrolytes above the glass transition temperature. In fact, those polymer electrolytes exhibit curved $\ln \sigma$ vs $1/T$ plots instead of straight lines. For that reason, instead of the Arrhenius equation, empirical equations such as the Vogel-Tamman-Fulcher (VTF) equation are commonly used to characterize the temperature dependent

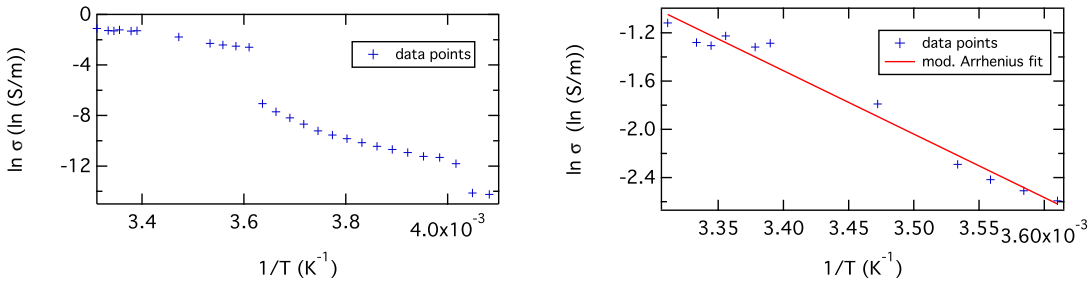

Figure 7.18: The natural logarithm of the measured conductivity of a particle-gel sample is plotted versus the reciprocal temperature (a). At temperatures above the freezing point, conductivity is dominated by ionic behavior. For higher temperatures the measured data hence were fitted by a modified Arrhenius equation (b) as described in the text.

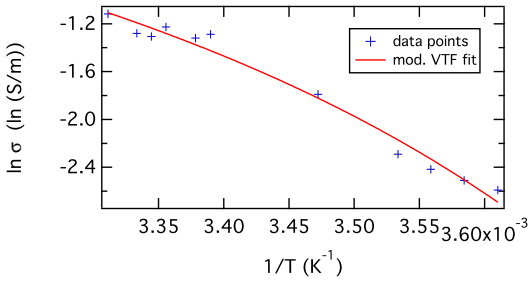

Figure 7.19: The natural logarithm of the conductivity was fitted according to the empirical Vogel-Tamman-Fulcher equation, which is commonly used to describe the temperature dependent conductivity process of liquid electrolytes (see text).

conductivity process of liquid electrolytes, where the solvent molecules are capable of orienting in the presence of an applied electric field [110]. The VTF equation is given by [122–125]

$$\sigma = \sigma_0 \cdot \frac{1}{\sqrt{T}} \exp\left(\frac{-E_a}{k_B(T - T_0)}\right) \tag{7.7}$$

where σ_0 is a constant, E_a the activation energy, k_B the Boltzmann constant and T_0 a reference temperature at which the configurational entropy of the polymer becomes zero and is close to the glass transition temperature. Figure 7.19 displays the logarithm of the measured conductivity and the logarithm of conductivity expressed with VTF formalism. An activation energy of $(18.7 \pm 4.4 \cdot 10^{-4})$ meV was revealed, which is a bit smaller than the value derived by Arrhenius. As the VTF equation was found to better fit the experimental data, the activation energy obtained by VTF can be assumed to approach the true value more closely.
While in the case of temperatures above the freezing point, ionic conductance thus clearly dominates, the situation is different for lower temperatures. Here, the IV

curves are ohmic and the conductivity dependence on temperature does not obey Arrhenius law. The reason for this is that with declining temperature the mobility of the ions and thus their contribution to conduction decreases [104, 118, 126]. The lower the temperature, the lower the activation energy. The IV characteristics become flatter. At some point the activation energy actually is too low to allow for ionic conduction processes and the curves become linear.
This ohmic behavior may arise from electronic current. Since the electrical conductivity of organic compounds and polymers usually is about 18 orders of magnitude smaller than those of metals [127], it can be assumed that the major contribution to electronic conductance is made up by electron transport through the Co nanoparticles. For all the considerations concerning electronic transport, it has to be kept in mind that the particle-gel system is a 3D system implying that there might be a vast range of inter-twined paths contributing to conduction. Let us now consider the contribution of electronic conductance via the gel. In organic biogels or biopolymers such as agarose (see section 3.2), organic molecules such as polysaccharides build up a network based on dipole-dipole interaction, hydrogen bonds or Coulomb forces. When dealing with electronic conductivity in organic molecular polymers, one has to distinguish between *inter*- and *intra*molecular types of electronic motion [127]. Although, conduction in organic compounds clearly differs from conduction in metals or inorganic semiconductors, band theory of atomic lattices has provided the basic concepts of intramolecular conduction in organic compounds [127]. For the intermolecular motion hopping conduction might occur. Normally, long polymeric molecules that only feature single bonds do not show significant electronic conductivity as they are chemically fully saturated. The situation is different for conjugated molecule chains. The spare electrons of the carbon atoms in the p_z-orbitals overlap and form delocalized molecular π-orbitals [127]. Those π-orbitals overlap and based on band theory of atomic lattices, the electronic states are expected to merge into a valence band. When electrons of the highest occupied orbital are excited to the lowest unoccupied of the conduction band, this results in metallic-like conduction for long polymer chains. In reality, however, good electronic conductivity was only found in combination with high crystallinity as for polyacetylene or in classes of organic compounds based on charge transfer complexes and radical ion systems (for further reading see [127]). Although, the EDTA contained in the buffer of the agarose gel features double bounds, i.e. delocalized electrons that might contribute to charge transport, agarose gel is not known to have a relevant electronic conductance. Since dried samples, however, are no longer conductive (section 5.1), there definitely is a certain amount of gel volume in-between the Co chain fragments and according to the size distribution of the nanoparticles also in-between the single superparamagnetic particles that are distributed between the chain fragments (compare section 6.4). While one can easily understand that the current and the spin information is forwarded via the Co nanoparticles, it is not clear which kind of mechanism applies to the gel volumes

that the electrons have to pass. A possible explanation might be that the electronic current and thus spin information is mediated by the electrons of the EDTA or some kind of electronic hopping mechanism occurs. This electronic contribution that is revealed at low temperatures is superimposed by the ionic contribution at high temperatures which is why it is not directly visible in the recorded characteristics.
Owing to the linearity of the IV characteristic, a solely or dominant contribution of tunneling at low temperatures can be excluded. On the grounds of this, the MR effect can at least not exclusively be of granular tunneling type, which confirms the applied assumption of granular GMR. The MR effect itself has to take place within the Co-chain fragments, while the spin information might be mediated through the gel volumes. Here, as already mentioned, the electrons of the EDTA could play a crucial role. Considerations of the spin diffusion length in the case of the gel can be found in section 9.2.

7.6 Summary

IV characteristics were recorded to investigate conduction in the gel. The conduction seems to be mainly ionic which was confirmed by stress measurements that show the typical behavior of the discharge current in an electrolyte solution. A problem associated with the ionic conduction in the matrix is electrolysis that occurs during the use of DC. With respect to magneto-transport measurements this leads to unstable voltages which is not preferable regarding the reproducibility of the GMR-effect amplitude. Electrical stress measurements were exploited for a more detailed examination of the temporal performance of gel E under and after an applied voltage. Stress voltages between 0.2 V and 2 V yielded current pulses with relaxation times of less than 9 s. When the stress was released, current pulses took place with a relaxation on shorter time scales of less than 6 s. A possibility to avoid these current fluctuations is the use of low currents in transport measurements. Most of the measurements in this work hence are performed by applying a current of only 5 µA. Furthermore, the employment of AC was found to suppress the influence of charge accumulation at the electrodes which will be investigated more closely in the next chapter.
Especially for gel samples that contain Co nanoparticles, however, electronic contribution to conductance certainly plays a role. By cooling down particle-gel samples, it was possible to distinguish electronic from ionic conductance. At room temperature and temperatures above the freezing point of the gel, the overall conductance process was encountered to be dominated by the ionic contribution. The temperature dependency of the conductivity was found to obey Arrhenius behavior with moderate quality as it is expected for ionic conductance from literature. The activation energy was determined to (452.7 ± 24.1) meV which was found to be in agreement with values for similar polymer electrolytes in literature. A greater

consistency of the fit with the experimental data could be achieved with the Vogel-Tamman-Fulcher equation, which is commonly used to characterize the temperature dependent conductivity process of liquid gel electrolytes below the glass transition temperature. The activation energy was derived to $(18.7 \pm 4.4 \cdot 10^{-4})$ meV. Of course, electronic conduction takes place in the Co nanoparticles. When the particle-gel sample was cooled down to temperatures, where the thermal activation energy is too low to allow for ionic conduction, the electronic contribution to conductance became visible. The electronic current measured was three orders of magnitude smaller and is thought to take place mainly in the nanoparticle chains and clusters as agarose gel itself is not known to be electronically conductive. The EDTA contained in the buffer, however, features chemical double bounds which means that free electrons might mediate electrical transport in-between the Co nanoparticles. Tunneling processes as main transport mechanism were excluded due to the ohmic shape of characteristics at low temperatures where the activation energy is too low for ionic conductance to occur. This implies that granular TMR at least by itself cannot explain the MR effects measured in the considered systems. Indeed, this fact can rather be interpreted as further evidence that the MR effect is of granular GMR type. The spin information hence would be passed on through the Co-nanoparticle chains and would be mediated via the gel, e.g. by the electrons of the EDTA, in-between the chain fragments. Considerations concerning the spin diffusion length in gel can be found in section 9.2.

8 AC-transport measurements

During measurements with DC disruptive electrolysis effects can occur in the matrix as was shown in section 7.4. Even though matrix E was found to show an improved reproducibility compared to other gels tested, the influence of electrolysis that might lead to unstable voltages and a low reproducibility of effect amplitudes, cannot be excluded. In this context, the use of AC, i.e. reversing the polarity of both electrodes periodically with a frequency higher than the timescales of processes at the respective electrodes, seems to be suitable to suppress electrolysis in the matrix during transport measurements. Some results of this chapter have been published in [128].

8.1 Transport measurements

Based on the results of section 7.4, AC transport measurements were performed according to the setup described in section 4.1.2. Preventing the influence of electrolysis, the voltage stability as well as the reproducibility of MR effects could significantly be enhanced. High effect amplitudes were achieved over a long period of time at a high signal-to-noise ratio. Figure 8.1 (a) displays a typical DC-transport measurement for a sample of Co nanoparticles in matrix E in comparison to a measurement with AC carried out at exactly the same sample position. The maxima of both curves are located at about the same magnetic field, which derives from the identical particle arrangement in the DC- and AC measurement. While the DC graph is quite noisy, though, the AC graph follows a very smooth curve. In figure 8.1 (b) the effect height of a measurement series over a period of about 50 minutes is plotted versus the number of measurement to illustrate the temporal development. The mean effect amplitude of the DC measurement was determined to $(21.9 \pm 2.6)\,\%$. In other words, the DC-GMR amplitude fluctuates around the AC value by a maximum of 30 %. The effect amplitudes of the AC measurements are almost constant at a value of 22.5 % with a standard deviation of only 0.7 % suggesting that fluctuations of the baseline voltage and thus of the GMR-effect amplitude such as for DC are eliminated by simply using AC. Consequently, in return for the more stable baseline voltages, outliers in the voltage and thus in the GMR-effect amplitude are suppressed by AC resulting in a loss of the maximum effect height, which originates from very small voltages that might occur using DC. Figure 8.2 (a) gives the first measurement of a series of AC measurements of a sample of Co nanoparticles in matrix E as well as the measurement number 21 at

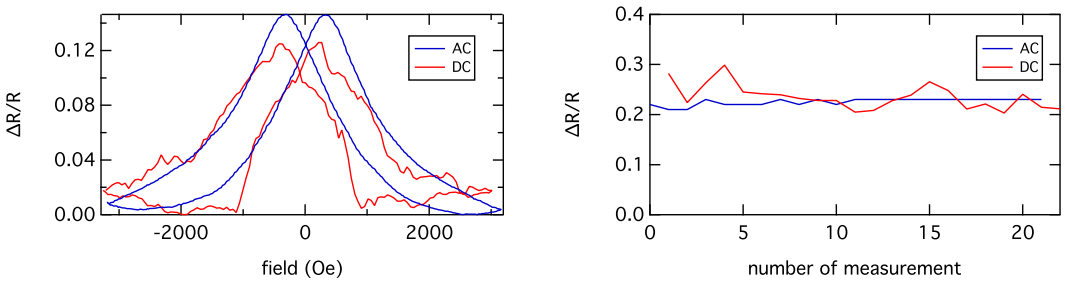

(a) (b)

Figure 8.1: Transport measurements carried out at a fixed position for a sample of Co nanoparticles in matrix E are shown for AC in comparison to DC (a). The development of the effect amplitude is plotted versus the number of measurement in subfigure (b).

the same position after 40 minutes. Both curves overlay almost exactly, which very nicely illustrates the stability of the GMR effect. When measured at different positions within the sample, however, a high variation of the effect height associated with the locally differing particle assembly in the sample can occur (figure 8.2 (b)).

The impact of more stable baseline voltages is particularly greater for matrix D, where very high baseline oscillations completely prevented the measurement of reproducible GMR-effect heights as was seen in section 6.2. The latter now become reproducible, the maximum effect amplitude, however, drops dramatically from more than 200 % to only roughly 4 % (figure 8.3 (a)) due to the suppression of voltage oscillations with outliers to extremely small values. In exchange for the smaller amplitudes, the effect heights get reproducible and reliable. Figure 8.3 (b) displays the temporal development of a granular system with matrix D over a period of about 40 minutes with a mean GMR value of (3.5 ± 0.1) %.
As mentioned earlier in chapter 5.1, the GMR-effect height is affected by the concentration of the magnetic nanoparticles in granular solids. Transport measurements with AC have been carried out for different mass concentrations c of Co nanoparticles in matrix D. It did not make sense to examine this question by DC-transport measurements due to the extremly fluctuating GMR-effect heights for this matrix. The obtained diagram of effect height versus concentration is illustrated in figure 8.4. The largest amplitudes were registered for a concentration of $c = 0.03$. An increase in concentration leads to a decline in the effect amplitude. Within the limits of error no differences in effect height were found between a concentration of $c = 0.04$ and $c = 0.05$. The position of the maximum is consistent with the corresponding measurements for the hydrogel in section 5.1 and lies in the same range as the maximum for the samples of matrix E treated with a rotation field in section 6.3.

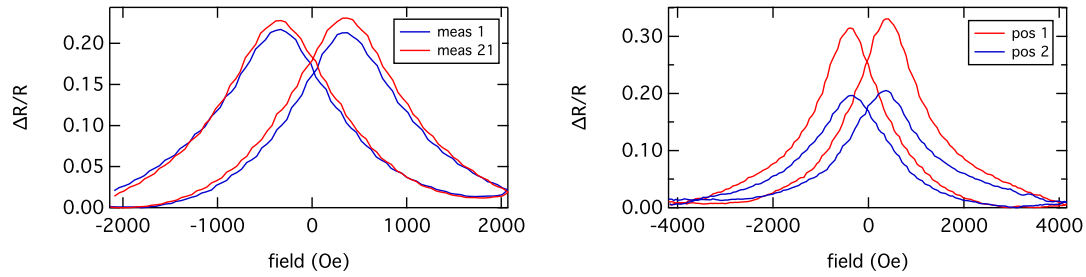

(a) (b)

Figure 8.2: The GMR curves of AC transport measurements are very stable. In subfigure (a) the first measurement and a measurement after 40 minutes is shown for a sample of Co nanoparticles in matrix E. As illustrated in subfigure (b), the effect amplitude at different positions (pos 1 and pos 2) within the sample, on the other hand, can vary greatly which is related to the local particle assembly.

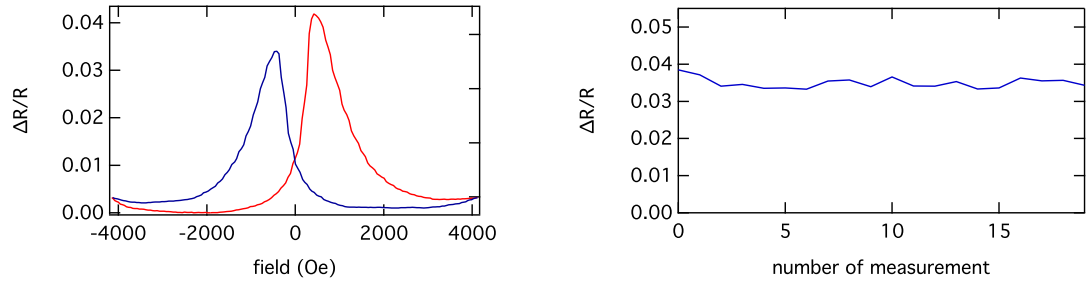

(a) (b)

Figure 8.3: A typical magneto-transport measurement of Co nanoparticles in matrix D performed with AC is shown in subfigure (a) and the temporal development of the GMR-effect height for a measurement series of about 40 minutes in subfigure (b).

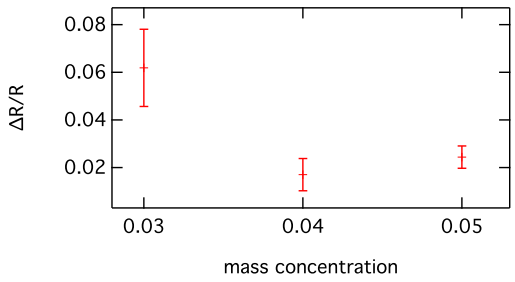

Figure 8.4: The GMR-effect height in dependence of the concentration of Co nanoparticles in matrix D was investigated by AC transport measurements.

8.2 Frequency-dependence of conductivity

When using alternating current, the question arises whether and to what extend the current frequency affects the conductivity and thus the GMR amplitude of the system. Figure 8.5 shows an example of the effect amplitude measured at 3 different frequencies for a particle-gel specimen measured in the AC setup. The curves almost overlap for these three frequencies. The GMR effect heights plotted versus a wider range of AC frequencies from 110 Hz to 100 kHz are displayed in figure 8.6 (a). The effect height was not found to vary much for frequencies in the limits of 110 Hz to 1510 Hz. Beyond frequencies of 1510 Hz, the effect height decreases from 1.3% to 0.5% before it increases again. The corresponding conductivity versus frequency plot (calculated from the voltage according to equation 4.3) can be seen in figure 8.6 (b). Starting with (25.1 ± 0.01) S/m at 110 Hz and (27.9 ± 0.16) S/m at 310 Hz, a plateau of nearly constant conductivity is formed at sufficiently low frequencies. According to the GMR-versus-frequency plot, the conductivity starts to decrease at frequencies higher than 1510 Hz down to (1.7 ± 0.05) S/m at 50 kHz, before it rises again. At 100 kHz the measured conductivity is (10.9 ± 0.03) S/m. The prominent dip in conductivity resembles the influence of an inductance. The fact that the same behavior was also observed for a pure matrix-E sample (see red markers in figure 8.7) excludes that there is a significant inductance attributed to the magnetic nanoparticles in the specimen. Since this response characteristic was measured for a carbon resistor, too (blue markers in figure 8.7), which should show a constant conductance over the considered frequency range, the inductivity seems to be caused by the setup itself, e.g. by the supply lines.

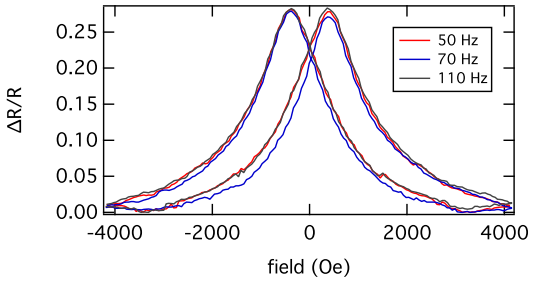

Figure 8.5: AC-magneto-transport measurements were carried out for Co nanoparticles in matrix E. There is no difference between the characteristics at the three frequencies displayed here.

Figure 8.8 (a) sketches how the setup can be converted into an equivalent circuit diagram. The alternating voltage source V_{in} and the dropping resistor R_2 are used to generate an alternating current. C_1 and C_2 are capacities and L_1 and L_1 inductances of the supply lines. R_1 reflects the measured resistor and was assumed to be 560 Ω. With capacities in the range of some nF and inductances of less than 1 mH, *SPICE* simulations of the model circuit (inset of figure 8.8 (b)) show a good agreement with the measured data (figure 8.8 (b)).
There is a large body of literature on the frequency-dependent AC conductivity of polymers and polymer composites [129–131]. The general behavior that is experimentally observed in a broad range of polymers is a constant value of conductivity

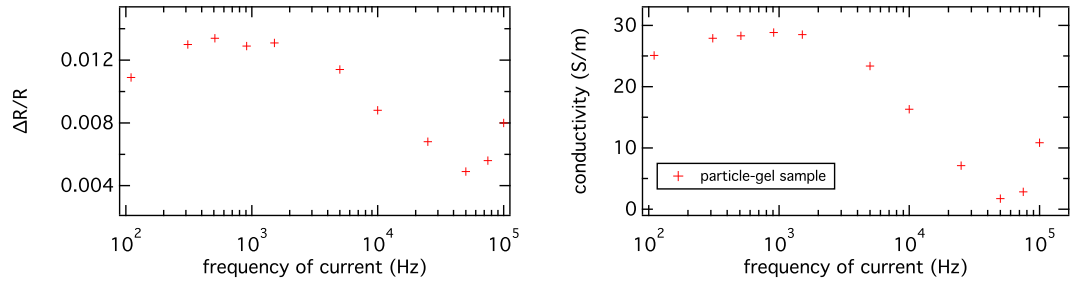

(a) (b)

Figure 8.6: Transport measurements were carried out for a particle-gel sample at different frequencies. The effect amplitude (a) and the conductivity (b) are plotted versus frequency.

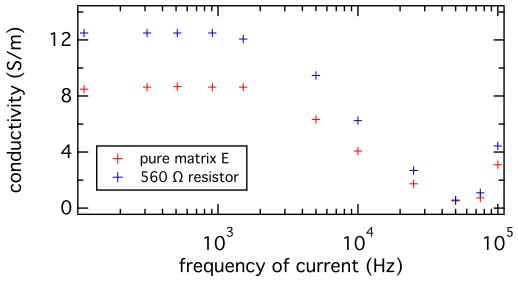

Figure 8.7: The conductivity is plotted for a pure gel E (red markers) versus AC frequency. The fact that the dip in conductivity is also found for a resistor (blue markers) indicates that the inductivity can be attributed to the setup.

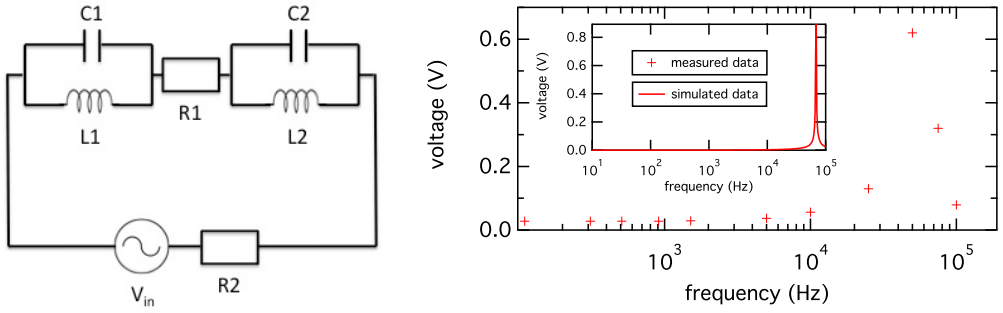

(a) (b)

Figure 8.8: The equivalent circuit diagram of the experimental setup is given (a). The alternating voltage source V_{in} and the dropping resistor R_2 generate an alternating current. C_1 and C_2 are the capacities and L_1 and L_1 the inductances of the supply lines. R_1 reflects the measured resistor. The measured data and the simulated response of the equivalent circuit diagram are shown in (b).

at sufficiently low frequencies that resembles the DC conductivity and a rise towards higher frequencies [132, 133]. For this frequency dependence is observed in a broad range of materials such as conducting polymers, ionic conductive glasses, disordered semiconductors or ionic crystals, Papathanassiou et al. argue that the qualitative response characteristic is unattached by the atomic structure of the material, but is associated with the morphology of the conducting network [130], and reproduce the ac response by a model assuming that electric charge flows along a network of conductive paths of different lengths. Although, the transport mechanism in the gels considered in this work has to be distinguished from the mechanism of conductance in conventional conducting polymers or the other systems previously mentioned (section 7), it can also be interpreted as a network of conducting parts. More detailed, these are the Co chain fragments in case of the electronic-, and the segments of the polymer salt complexes within the polysaccharide net in case of the ionic conduction. As a consequence it can be expected that the frequency dependent conductivity should behave similar to the characteristic described above. Indeed, the conductivity is constant in the low-frequency regime at the value of the DC conductivity, which is about 8 S/m for the pure gel matrix and about 15 S/m for the particle-gel sample. Eventually, the remarkable dip occurs and the conductivity rises from 50 kHz on suggesting a trend towards further increasing conductivities. Potential frequency-dependent changes in the conductivity, however, might be hidden due to the large effect of the inductance on the response characteristic. Therefore, an influence of a change in frequency cannot be eliminated. It can be stated, though, that if there were changes in conductance, they would be very small.

8.3 Summary

In conclusion, it can be said that transport measurements carried out with alternating instead of direct current are suitable to prevent distortions associated with electrolysis such as strongly varying baseline voltages in the gel matrices. The reproducibility of the GMR effect amplitude over time could be enhanced at an increased signal-to-noise ratio. AC hence is the preferred choice for magneto-transport measurements of granular systems containing biogel matrices.
The dependency of the conductivity on frequency was tested within a range of 110 Hz to 100 kHz. Gauging the AC setup leads to the conclusion that the favored frequencies leading to the highest conductivities for this setup are located within 110 Hz and 1510 Hz. From 110 Hz to 1510 Hz the conductivity was found to be constant at a value equal to the DC conductivity. A dip found at subsequent frequencies up to 50 kHz in the frequency dependence of conductivity could be attributed to the measurement setup itself. Although, an influence of the frequency could not explicitly be excluded, it can - if existent - be assumed to be very small. More generally, the measurements show that cabling of the respective setup might

have an important influence on the recorded conductivity. With regard to sensor application the inductive and capacitive properties of the supply lines thus should always be taken into consideration.

9 Outlook

The results of this thesis indicate that it is worth to continue work on granular GMR in gel systems. The next crucial step will be the industrial manufacturing of a gel-GMR sensor. Furthermore, investigations on the spin diffusion length in gel would help to gain a deeper insight in the corresponding transport mechanisms. The following chapter thus outlines a concept of future studies. It gives an introduction into the idea of the granular-gel GMR sensor, proposes a field of application that would benefit from its use and summarizes first steps regarding the sensor realization and the measurement of the spin diffusion length that have already been performed within the scope of this dissertation.

9.1 Realization of granular gel-GMR sensor

9.1.1 Concept

The discovery of the GMR effect and the final technological development regarding the controlled fabrication and characterization of nanostructures allowed the launch of a magnetic field sensor, which by the 1990s was already commercially available [5] . In the simplest setup, a conventional GMR sensor consists of two fm layers that are separated by a nonmagnetic spacer (compare section 2.3.2). The electric resistance of the device depends on the orientation of the magnetizations in the two layers. The magnetization of one of the layers is fixed while the other one can e.g. be influenced by an external stray field of a particle that is to be detected. For a parallel configuration of the sensing layers, the electrical resistance of the GMR device is low whereas it is high for the antiparallel configuration due to an increased scattering probability of the conducting electrons.
With the progressive miniaturization of functional devices, the superparamagnetic limit is approached. On these scales thermal fluctuations of the magnetization become significant, which is why larger anisotropies are necessary to obtain stable magnetic equilibrium states. This means that larger magnetic fields are required for switching as well as for writing the magnetizations. In sensor technology this corresponds to a decreased sensor sensitivity. A possibility to overcome this problem is the change to granular material, where magnetic domains are separated by a metallic matrix [3, 4, 103]. For the limit case of dipolar coupled nanoparticles, numerical studies on arrays of nanoparticles have been carried out to analyze their electric transport characteristics in response to a magnetic field with respect to

their capability to serve as magnetic field sensor. The following results were published in [134].
Initially, the magnetic equilibrium configuration was evaluated by solving the Landau - Lifshitz equation for a particle ensemble. Therefore, the magnetic nanoparticles were assumed to be homogeneously magnetized [134, 135] and were thus approximated by magnetic dipoles. Solutions for a system consisting of 64 particles positioned along a cubic grid that arise from the minimization of the systems stray field energy are presented in figure 9.1. The left side displays the azimuthal component of the magnetization (color-code: disc) whereas the right side represents the out-of-plane component. In contrast to the magnetic distributions of continuous films, magnetic moments reach orientations with a globally and locally vanishing sample magnetization which is a result of the missing exchange coupling between the individual granules. In addition, an increasing aspect ratio (from subfigure 9.1 (a) to (c)) leads to a stronger in-plane confinement of the magnetic moment vectors. This resembles the situation for continuous films without strong perpendicular anisotropy. In other words, such granular systems maintain the magnetic distributions of continuous films, but also exhibit a magnetic substructure resulting from the absence of exchange-coupling.
In order to investigate the transport properties of these structures, the GMR characteristics were evaluated. As a direct calculation of the GMR behavior via transport equations is far too complicated, this was done using

$$GMR = 1 - \frac{C}{2}\langle 1 + \cos\theta \rangle^2 \tag{9.1}$$

with C as a measure for the spin dependence of electron scattering set to $C = 1$ for reasons of simplicity and θ the angle between adjacent magnetic moments. Figure 9.2 exemplarily shows the solutions of an 10×10 array of particles with radius of 8 nm arranged in hexagonal symmetry with a lattice constant of 20 nm, a magnetization of 1000 kA/m and with varying species of nanocomponents. Indeed, it was found that granular films can act as magnetic field sensors if the area of operation is chosen along one of the response slopes with a biunique relation between magnetic response and field. Furthermore, the GMR response varies with respect to the type of nanoparticle. In particular, this means that the GMR device can be adjusted to a specific task or measurement. Sensors based on the granular particle-gel systems investigated in this work would even enhance sensor sensitivity due to the high effect amplitudes.

9.1.2 Application

In general, it would be conceivable that granular GMR sensors are used in all scopes of application suitable for conventional GMR sensors. An example is the spatial detection of small magnetic sources such as superparamagnetic beads that are

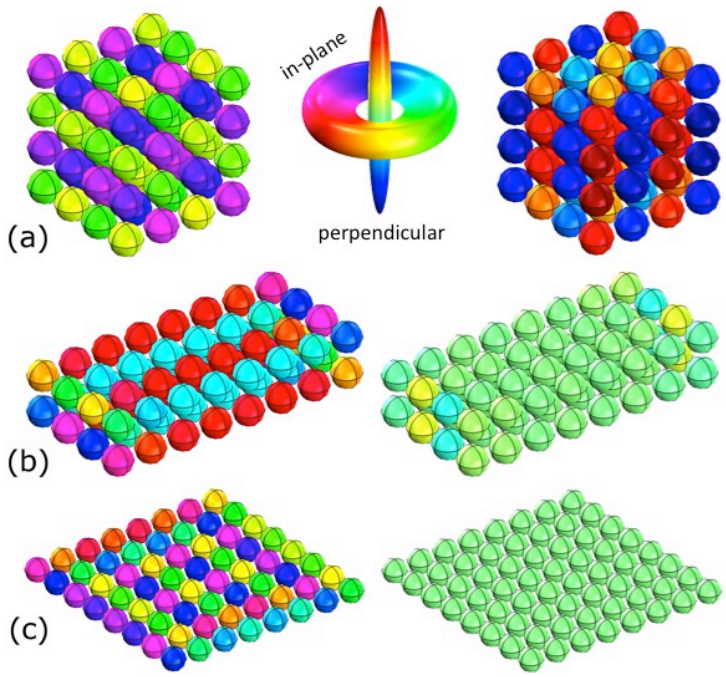

Figure 9.1: The magnetic equilibrium states of ensembles of dipolar coupled nanoparticles have been calculated [134]. The distributions of the in-plane components are displayed on the left (color code: disc) and the out-of-plane contributions on the right side of the figure (color-code cone). For all configurations the minimization of the stray field energy is the driving force. Due to the absence of exchange coupling, the global and local magnetization of the system disappears. With increasing aspect ratio, out-of-plane contributions vanish and the magnetic distribution is dominated by the geometry of the system.

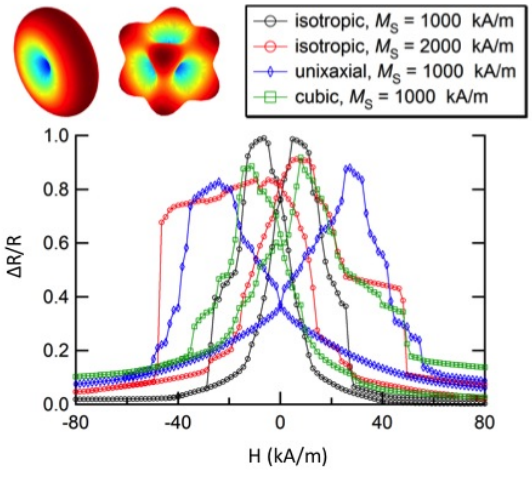

Figure 9.2: The response properties of a 10×10 hexagonal assembly of particles with a radius of 8 nm have been calculated for different magnetic particle properties [134].

attached as markers to biomolecules. This concept is used in lab-on-a-chip immuno assays which constitute an established method in medical analysis designed to determine the concentration of a macromolecular analyte (antigen) in solution [6,7]. Nowadays, those immune assay procedures are carried out on so-called Micro Total Analysis Systems (µTAS), chips of only few cm^2. Analytes in the sample are immobilized on the chip surface. Labeled antibodies that specifically bind the target antigen on the chip surface are then introduced into the system. All unbound labels are removed in a washing step before the remaining labeled molecules can be detected. One possibility to label molecules is the attachment of superparamagnetic beads. Here, GMR sensors, either in form of a multilayer or a granular GMR sensor, can be used for detection as the dipolar magnetic stray field of the beads influences the magnetic configuration of the sensor layer inducing a change in the electrical resistance. The GMR sensors are integrated in the µTAS structure. All lab-on-a-chip immuno assays usually require microfluidic channel systems and suffer from the fact that the majority of the labeled molecules passes the sensing area without contacting the sensor surface. In the past, different approaches, employing magnetic forces, ultrasonic standing waves, or hydrodynamic effects have been suggested to circumvent this problem [136–139]. Common to them all is that well-defined surfaces and lithography steps are necessary, which entails increased production costs often preventing a successful market introduction. As published in [140], paper-based test strips printed with gel-based GMR sensors represent an alternative sensor concept offering the advantage of reduced production costs of the µTAS system due to the simplified fabrication of these strips. Instead of structuring sensors on the bottom of a microfluidic channel, gel containing magnetic nanoparticles could be printed on small paper strips, similar to a pH-test strip. The concept is sketched out in figure 9.3. The surface of the gel has to feature functional groups that are able to bind antibodies. The test strip can be activated for a specific immunoassay by dipping the strip in the respective antibody solution. The next step is the preparation of the test sample, e.g. blood containing the antigens to be detected. Therefore, the test sample is mixed with a bead solution containing the marker beads that due to antibodies on their surface link to the antigens in the test solution. Dipping the activated strip into this mixture leads to the linking of the antigens that are labeled with the beads and the antibodies of the gel. After a washing step, in which unbound beads are removed, the strip can be inserted into a standardized magnetic field. The developing stray field of the beads would alter the resistance of the GMR gel according to the GMR effect, which allows the direct measurement of the bead and thus of the antigen density. Finally, the problem of the contact between beads and surface could be circumvented as the mixing takes place under macroscopic flow conditions.

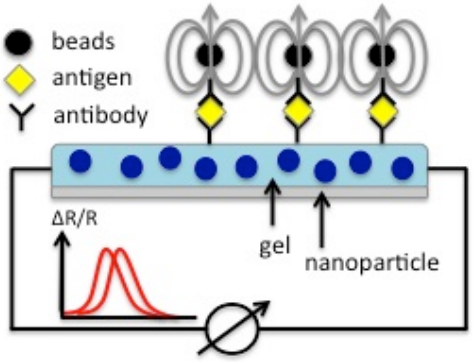

Figure 9.3: A gel-GMR sensor in form of a test strip for a immuno assay is illustrated. Dipped into a sample containing the antigens to be detected, the antigens labeled with superparamagnetic beads link to the antibodies bound on the gel surface. In a magnetic field, the magnetic stray fields of the beads influence the resistance of the gel-GMR sensor and allow to determine the bead and thus antigen density.

9.1.3 Production

While printed electronics are well-developed in a broad range of applications such as organic light-emitting diodes (OLEDs), organic photovoltaics, displays, sensors and electronic components such as batteries, printable magnetic sensing devices are a quite new research field [141]. All of the gels employed in this work, basically, offer the possibility of being printed, which has the advantage that GMR sensors can be realized without the employment of photo- or e-beam lithography or sputtering processes which will reduce the complexity of the overall production process. Together with the fact that biogels such as agarose- or alginate gels are available at low cost since they are based on seaweed and their sources hence may be regarded as unlimited, this results in a fabrication more rapid and less expensive compared to conventional manufacturing processes. Besides, gels are shapable and mechanically flexible as mentioned in section 3.2, which might open up new fields of application. Further advantages are light weight, reduced size and disposability. Printing will be realized with industrial partners (*MEAS Deutschland GmbH*) using the printer displayed in figure 9.4. A pre-structured wafer is placed on the base of the printer (hot plate). For applications where a hot plate is required, it can be heated up to 400°C. Furthermore, it allows to apply a rotational or homogenous magnetic field for structuring the printed particle-gel mixtures. Microtubes on the right side of the printer are used for storage of the liquids and as a reservoir for cleaning fluids. Controlled by a computer, Eppendorf pipettes dip in the reservoir to get the required amount of mixture. Afterwards, they are positioned at the desired spot on the wafer and dip a drop of the mixture on it. In the event that different liquids are needed, such as for alginate gel, where the alginate-particle mixture and the gelling agent are printed, the pipette is cleaned after printing the first mixture by moving in and out a cleaning liquid at the micro tube reservoir before the second liquid is collected and positioned at the respective spot. On the

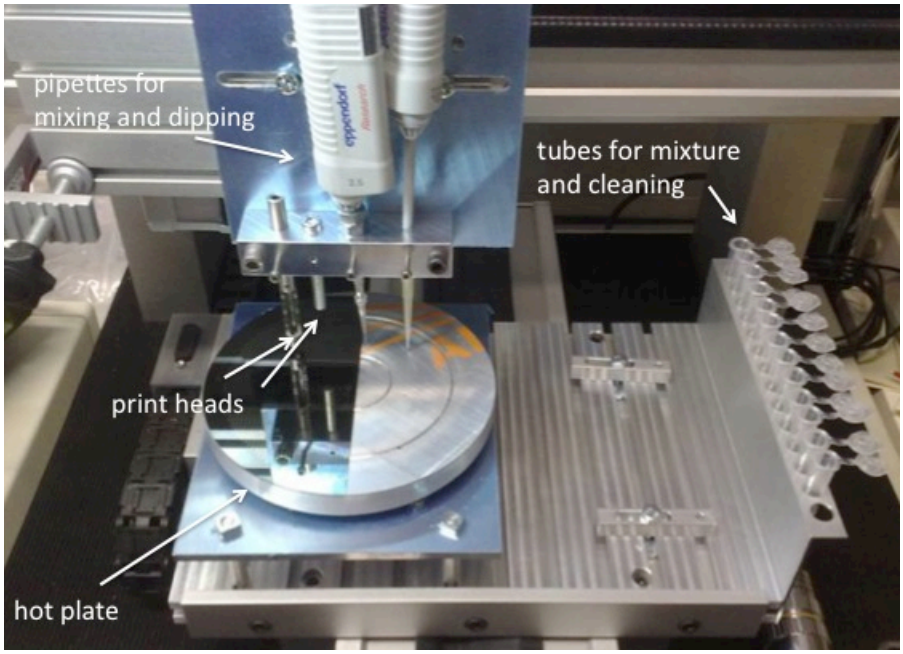

Figure 9.4: The figure displays the printer. It consists of a hot plate, on which a pre-structured wafer can be placed. The micro tubes on the right side are used to store the mixtures and cleaning liquids for the pipettes. The printing process is computer operated. Eppendorf pipettes fetch the mixtures from the micro tubes reservoir and position drops on the desired spots on the wafer.

whole, the printing process for a gel looks as follows: Printing of the gel-particle mixture, heating the plate in the case of matrix E to keep it liquid, applying the magnetic field for structuring, turn off the hot plate in case of matrix E or printing a crosslinking agent in the case of a gel such as matrix D to initialize the gelling process.

9.2 Measurement of spin-diffusion length

When a current is passed from a FM into nonmagnetic material, a net spin angular momentum and thus a net magnetization is injected in the new material, provided that one spin type is dominant in the electrical transport of the FM [142]. This non-equilibrium magnetization induced in the paramagnet is called spin accumulation. It decays exponentially away from the interface on a length scale known as spin-diffusion length λ_s which is determined by the interaction between the net spin-injection and the spin-flipping rate in the paramagnet. As already discussed in subsection (2.3.2), λ_s is the crucial scaling length for CPP. Although, experiments in vertical CPP-GMR configurations have also been carried out [143], spin valve

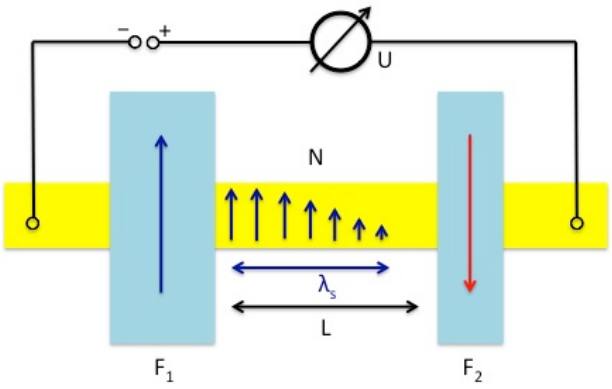

Figure 9.5: A lateral spin valve consists of two fm contacts (F1 and F2) located at a distance L to each other and connected by a nonmagnetic wire (N). Transport measurements reveal a magnetoresistive behavior as long as L is smaller than λ_s (blue arrows). Modeled after [155].

effects using lateral structures were found to be more suitable to investigate the spin-diffusion length. Such lateral spin valves have been used by a number of groups [144–150], since the first experiment on the spin injection and detection in bulk aluminum in 1985 [142]. Typical lengths for λ_s are 140 nm for Cu [151], 59 nm for Co [152] and 5 nm for permalloy at low temperatures. Spin-diffusion lengths in the range from 10-100 nm have been derived for spintronic devices utilizing spin injection and transport through a semi-conducting spacer layer [153, 154]. The conventional case of a classical spin valve is depicted in figure 9.5. Spin polarized electrons are injected from a first FM (F1) into a nonmagnetic stripe (N) and are detected in a second FM (F2) [155]. In the linking wire N a non-equilibrium spin accumulation is induced by spin polarized electrons from F1. As mentioned above, this spin accumulation decays within the characteristic spin diffusion length (visualized by differently sized blue arrows and indicated by λ_s in figure 9.5). It can be detected with the F2 as the relative orientation of the detector spin and spin accumulation sensitively determines whether a low or a high resistance is measured. The electrodes are different in size resulting in different coercive fields. Transport measurements will reveal a magnetoresistance effect as long as the distance L between the two FMs is smaller than the spin diffusion length λ_s. For parallel alignment of the magnetizations of F1 and F2 a low and for antiparallel alignment a high voltage or resistance is measured.

In order to investigate the spin-diffusion length and the transport mechanism in gel more closely, a modified lateral spin valve system was designed (see figure 9.6). Just as the spin valve in figure 9.5, it consists of parallel pairs of fm electrodes ($F1$ and $F2$) separated by different distances. Instead of bridging those electrodes by a nonmagnetic stripe, however, the connection is made by the gel under investigation. Varying the distances between the electrodes allows to determine λ_s which equals the length at which magnetic behavior can no longer be detected. The spin injector as well as the spin detectors are made of a FM such as permalloy. Dif-

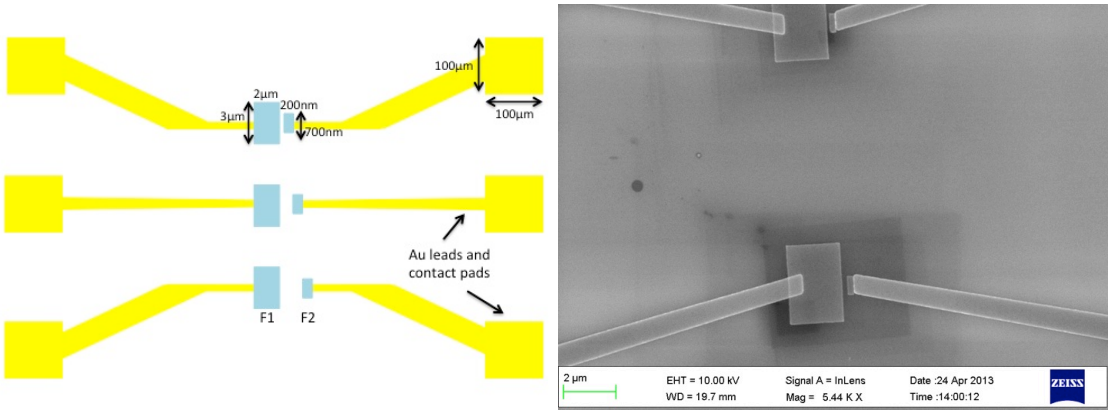

(a) (b)

Figure 9.6: The lateral spin structure for the measurement of the spin diffusion length in gel is sketched (a). Two FMs (F1 and F2) with different switching fields are separated by a gap. F1 and F2 get connected by gel. As long as the distance between the two FMs is smaller as the spin diffusion length λ_s a magnetoresistive behavior can be detected if a current is induced by the contact lines. If the distance becomes larger than λ_s this magneto dependence will vanish.

ferent widths for injector and detector are chosen to guarantee different switching behavior. To avoid the FM to be soft magnetic the height is chosen to be only few nm. Gold leads of a length of few hundred micrometer connect the FMs and the contact pads located at the edge of the structure. The size of the contact pads ($100\ \mu\text{m} \times 100\ \mu\text{m}$) is chosen large enough to facilitate the bonding later on. In order to prevent a short circuiting of the gold leads via the gel, the gel is to be placed in such a way on the spin valve that it does not completely cover both FMs, but only the area in-between the two FMs and also a part of each FM. Since the dimensions are too small to correctly position the gel drop by hand, an insulating protection layer of, for example, MgO with a recess for the gel drop and the contact pads, is sputtered on top of the whole arrangement. In figure 9.6 (b) the FMs and the conducting lines of a fabricated test structure can be seen. In general, it is possible to structure FMs with a laterally distance down to the size of 25 nm (see figure 9.7 and figure 9.8).

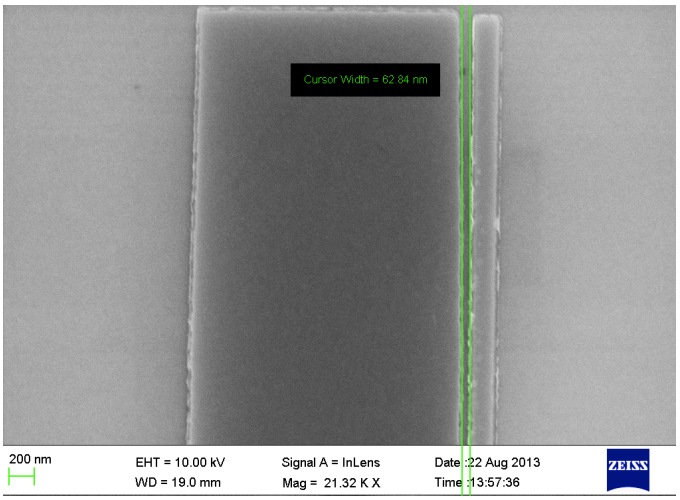

Figure 9.7: Spin valve test structure with about 63 nm between FM1 and FM2.

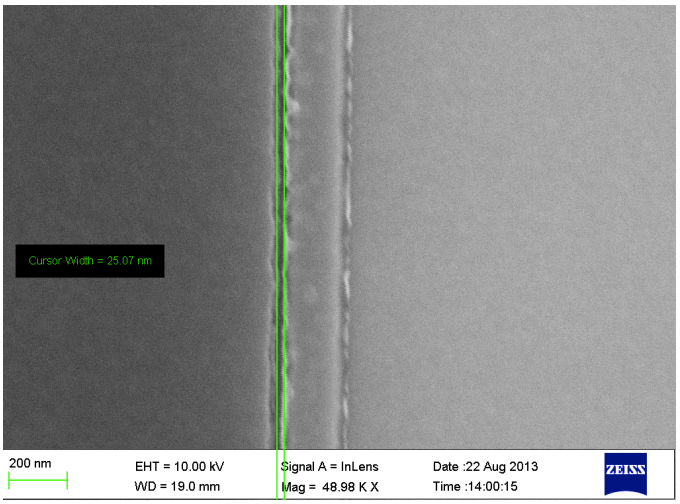

Figure 9.8: Spin valve test structure with about 25 nm between FM1 and FM2.

10 Conclusion

In summary, it was shown that it is possible to replace common metallic matrices for granular GMR systems by conductive gels. Magneto-transport measurements at systems composed of Co nanoparticles embedded in hydrogels revealed GMR-effect amplitudes of up to 260 % at room temperature, which is very high compared to conventional systems. These gels thus are very interesting in terms of sensor application and were analyzed more closely throughout this thesis.
In hydrogels with a viscosity low enough to allow for the movement of the magnetic nanoparticles, the latter will arrange in chain fragments under the influence of the external magnetic field applied during the transport measurement. Magneto-transport measurements with the current applied both parallel and orthogonal to the magnetic field and thus to the chain structures revealed a GMR effect. The measurements with current flow parallel to the chain fragments, however, lead to an increase in the effect height. Very narrow GMR characteristics at comparable effect amplitudes were achieved by the use of Heusler-based nanoparticles. The observed soft switching is of high technological relevance regarding sensor application and could be related to the Heusler phase.
As particle movement in matrices with relatively low viscosity such as the tested hydrogels, leads to varying effect amplitudes over time, the hydrogels were replaced by gels featuring a liquid-solid transition, after which the magnetic particles are fixed in the gel environment. Two gel types, namely alginate gel (matrix D) and agarose gel (matrix E) were tested. Concerning voltage stability, matrix E was found to be more suitable than matrix D. The employment of matrix E in granular GMR systems resulted in a higher reproducibility of the GMR-effect amplitude over time. Additionally, gels with a liquid-solid transition allow to deliberately arrange particle superstructures within the sample. For a 2 %- and 3 %-agarose concentration an increased effect height could be attained by the application of a rotational field in a frequency regime of 500 rpm which lead to a homogenous dispersion of the nanoparticles. A further increase of effect height was reported for the employment of a homogenous magnetic field during preparation resulting in the development of particle-chain structures in the matrix.
The conductance mechanism within the gel matrix was investigated by electrical transport and electrical stress measurements. Electrical transport measurements indicated conductance of mainly ionic behavior by the appearance of electrolysis effects in the matrix. This assumption could be confirmed by temperature dependent IV characteristics. For temperatures above 273 K, the conductivity showed Arrhenius behavior with an activation energy of (452.7 ± 24.1) meV. A fit according

to the Vogel-Tamman-Fulcher equation resulted in an even better consistency with the experimental data. The corresponding activation energy was determined to $(18.7 \pm 4.4 \cdot 10^{-4})$ meV. By cooling a particle-gel sample below the freezing point of the gel, where the activation energy is too low for ionic conductance to occur, the electronic conduction could be separated from the ionic contribution. The electronic conduction, basically, is thought to take place within the Co chain fragments. Tunneling processes as main transport mechanism can be omitted due to the ohmic shape of the IV characteristics at low temperatures. Therefore, granular TMR by itself cannot explain the measured MR effects, which can be regarded as a further evidence that the MR effect is of granular GMR type. The GMR effect hence would take place in the Co-nanoparticle chains and the spin information would be mediated via the gel. This could, e.g., be achieved by the electrons of the EDTA contained in the buffer. It features chemical double bounds and could provide free electrons that mediate the electrical transport in-between the Co nanoparticles. An impact of the ionic behavior of conductance in the matrix are electrolysis effects occurring during measurement. They result in a conductivity difficult to control, which is why they are undesirable. According to electrical stress measurements carried out for different stress voltages, a transient response current appears if stress voltages of more than 0.2 V are used. If current pulses occur, the saturation current is reached after at least 9 s. No significant current pulses were noticeable when voltages of 0.2V and below were applied. Since a constant current flow is desirable regarding magneto-transport measurements, the pulses in the response current can be suppressed by either avoiding voltages of more than 0.2 V or, if higher voltages are applied, by waiting a time period of at least 9 s before starting to measure. As a result, subsequent transport measurements were performed in low current (5 µA) and voltage ranges, respectively.
Moreover, the use of AC for the magneto-transport measurements was found to suppress electrolysis in the matrix. Both the reproducibility of the effect amplitude over time and the signal-to-noise ratio could be improved by AC-transport measurements. A distinct AC-frequency dependence of the MR effect amplitude was not found for the frequencies tested from 100 Hz to 100 kHz. Magneto-transport measurements for granular particle-gel systems should thus be performed with AC. The fact that magneto-transport measurements at the gel-particle systems studied within this thesis revealed a biunique connection between the applied magnetic field and the GMR ratio as well as a smooth switching characteristic of the magnetic state allows for the employability of such systems as magnetic field sensors. A scope of application are paper-based test strips printed with gel-based GMR sensors that represent an alternative sensor concept for µTAS systems as illustrated in the outlook. The manufacturing of these sensors could be realized by printing the particle-gel mixtures on paper strips instead of using common techniques such as ebeam lithography or sputtering processes as it is necessary in case of conventional sensor types. The complexity of the production process of the GMR sensor

could hence be reduced. Furthermore, the gels are based on seaweed, which is why they are cheap and abundant in supply. The employment of gel additionally offers the possibility to specifically shape the sensors which might enlarge the field of application. All in all, granular gel-based sensors offer the advantage of a faster and cheaper production process compared to conventional sensor production. The manufacturing of gel-GMR sensors will be realized in cooperation with industrial partners (*MEAS Deutschland GmbH*). First steps such as the installation of the printer have already been carried out. Further studies regarding granular gel GMR might include the investigation of the spin transport in gel. A concept using modified lateral spin valves and first steps of its implementation have been outlined. On the whole, it can be stated that particle-gel systems offer great potential for granular GMR sensors and the results of this work encourage to pursue further studies in this field.

Bibliography

[1] M. N. Baibich, J. M. Broto, A. Fert, F. Nguyen Van Dau, and F. Petroff. Giant Magnetoresistance of (001)Fe/(001)Cr Magnetic Superlattices. *Phys. Rev. Lett.*, 61(21):2472, 1988.

[2] G. Binasch, P. Grünberg, F. Saurenbach, and W. Zinn. Enhanced magnetoresistance in layered magnetic structures with antiferromagnetic interlayer exchange. *Phys. Rev. B*, 39(7):4828, 1989.

[3] A. E. Berkowitz, J. R. Mitchell, M. J. Carey, A. P. Young, S. Zhang, F. E. Spada, F. T. Parker, A. Hütten, and G. Thomas. Giant Magnetoresistance in Heterogeneous Cu-Co Alloys. *Phys. Rev. Lett.*, 68(25):3745, 1992.

[4] J. Q. Xiao, J. Samuel Jiang, and C. L. Chien. Giant Magnetoresistance in Nonmultilayer Magnetic Systems. *Phys. Rev. Lett.*, 68(25):3749–3752, 1992.

[5] IBM. http://www.research.ibm.com/research/gmr.html. Accessed: 2013-06-04.

[6] C. P. Y. Chan, Y. C. Cheung, R. Renneberg, and M. Seydack. New trends in immunoassays. *Adv. Biochem. Eng. Biotechnol.*, 109:123–154, 2008.

[7] B. Mattiasson, K. Teeparuksapun, and M. Hedstrom. Immunochemical binding assays for detection and quantification of trace impurities in biotechnological production. *Trends Biotechnol.*, 28:20–27, 2010.

[8] A. P. Guimarães and I. S. Oliveira. *Magnetism and magnetic resonance in solids*. John Wiley & Sons, INC., 2002.

[9] B. D. Cullity and C. D. Graham. *Introduction to magnetic materials*. 2 edition.

[10] S. P. Gubin. *Magnetic Nanoparticles*. Wiley-VCH, 2009.

[11] A. Hubert and R. Schäfer. *Magnetic Domains - The Analysis of Magnetic Microstructures*. Springer-Verlags, 1998.

[12] C. J. O' Connor, J. Tang, and J. H. Zhang. *Magnetism: Molecules to Materials III - Nanosized Magnetic Materials*. Wiley-VCH, 2002.

[13] J. Frenkel and J. Dorfmann. Spontaneous and Induced Magnetisation in Ferromagnetic Bodies. *Nature*, 126:274, 1930.

[14] C. Kittel. *Einführung in die Festkörperphysik*. R. Oldenbourg Verlag, 1999.

[15] B. Murray, S. Sun, H. Doyle, and T. Betley. Monodisperse 3d Transition-Metal (Co, Ni, Fe) Nanoparticles and their Assembly into Nanoparticle Superlattices. *MRS Bulletin*, 26:985, 2001.

[16] B. Kalska, J. J. Paggel, P. Fumagalli, M. Hilgendorff, and M. Giersig. Magneto-optics of thin magnetic films composed of Co nanoparticles. *J. Appl. Phys.*, 92:7481, 2002.

[17] W. F. Brown. Thermal Fluctuations of a Single-Domain Particle. *Phys. Rev.*, 130:1677, 1963.

[18] C. Kittel. On the gyromagnetic ratio and spectroscopic splitting factor of ferromagnetic substances. *Phys. Rev.*, 30:743–748, 1949.

[19] J. D. Jackson. *Classical electrodynamics*. Wiley, 1975.

[20] A. K. Garg. *Classical electromagnetism in a nutshell*. Princeton University Press, 2012.

[21] A. Weddemann. *A finite element analysis of a microfluidic lab-on-a-chip system employing magnetic carriers for biomedical applications*. PhD thesis, Bielefeld University, 2009.

[22] P. Grünberg, R. Schreiber, M. B. Pang, Y. Brodsky, and H. Sowers. Layered Magnetic Structures: Evidence for Antiferromagnetic Coupling of Fe Layers across Cr Interlayers. *Phys. Rev. Lett.*, 57:2442, 1986.

[23] S. S. P. Parkin, N. More, and K. P. Roche. Oscillations in exchange coupling and magnetoresistance in metallic superlattice structures: Co/Ru, Co/Cr, and Fe/Cr. *Phys. Rev. Lett.*, 64:2304–2307, 1990.

[24] M. Rührig, R. Schäfer, A. Hubert, R. Mosler, J. A. Wolf, S. Demokritov, and P. Grünberg. Domain Observations on Fe-Cr-Fe Layered Structures. *Phys. Stat. Sol. (a)*, 125:635–656, 1991.

[25] P. Bruno and C. Chappert. Oscillatory coupling between ferromagnetic layers separated by a non-magnetic metal spacer. *Phys. Rev. Lett.*, 67(12):1602–2592, 1991.

[26] P. Bruno. Theory of interlayer magnetic coupling. *Phys. Rev. B*, 52(1):411–439, 1995.

[27] W. Thomson. On the Electro-Dynamic Qualities of Metals: Effects of Magnetization on the Electric Conductivity of Nickel and of Iron. *Proc. Royal Soc.*, 8:546–550, 1865-1875.

[28] W. Thomson. On the electrodynamic qualities of metals: effects of magnetization on the electric conductivity of nickel and iron. *Proc. Roy. Soc. London*, 8:546–550, 1993.

[29] T. Miyazaki and N. Tezuka. Giant magnetic tunneling effect in Fe/Al2O3/Fe junction. *J. Magn. Magn. Mater.*, 139:L231–L234, 1995.

[30] J. S. Moodera, L. R. Kinder, T. M. Wong, and R. Meservey. Large Magnetoresistance at Room Temperature in Ferromagnetic Thin Film Tunnel Junctions. *Phys. Rev. Lett.*, 74:3273, 1995.

[31] T. R. Mc Guire and R. I. Potter. Anisotropic Magnetoresistance in Ferromagnetic 3d Alloys. *IEEE Trans. Magn.*, 11:1018–1038, 1975.

[32] R. Coehoorn. Giant Magnetoresistance in Exchanged-Biased Spin-Valve Layered Structures and its Application in Read Heads. In *Magnetic Multilayers and Giant Magnetoresistance - Fundamentals and Industrial Applications*. Springer-Verlag, 2000.

[33] J. Smit. Magnetoresistance of ferromagnetic metals and alloys at low temperatures. *Physica*, 16:612–627, 1951.

[34] H. Kano, K. Kagawa, A. Suzuki, A. Okabe, K. Hayashi, and K. Aso. Substrate temperature effect on giant magnetoresistance of sputtered Co/Cu multilayers. *Appl. Phys. Lett.*, 63:2839, 1993.

[35] N. F. Mott. The Resistance and Thermoelectric Properties of the Transition Metals. *Proc. Roy. Soc.*, 156:368–382, 1936.

[36] E. Y. Tsymbal and D. G. Pettifor. Perspectives of giant magnetoresistance. *Sol. Stat. Phys.*, 56:113, 2001.

[37] T. Valet and A. Fert. Theory of the perpendicular magnetoresistance in magnetic multilayers. *Phys. Rev. B*, 48(10):7099–7113, 1993.

[38] T. Shinjo. *Nanomagnetism and Spintronics*. Elsevier, 2009.

[39] J. F. Gregg, I. Petej, E. Jouguelet, and C. Dennis. Spin electronics- a review. *J. Phys. D: Appl. Phys.*, 35:R121–R155, 2002.

[40] M. Julliere. Tunneling between ferromagnetic films. *Phys. Lett. A*, 54:225–226, 1975.

[41] E. Y. Tsymbal, O. Mryasov, and P. R. LeClair. Spin-dependent tunnelling in magnetic tunnel junctions. *J. Phys. Condens. Matter.*, 15:R109–R142, 2003.

[42] Mott. Electrical conductivity of transition metals. *Proc. Roy. Soc. A*, 153:689, 1936.

[43] H. Fujimori, S. Mitani, and S. Ohnuma. Tunnel-type GMR in metal-nonmetal granular alloy thin films. *Mater Sci. Eng. B*, 31:219–223, 1995.

[44] H. Fujimori, S. Mitani, and S. Ohnuma. Tunnel-type GMR in Co-AI-O insulated granular system - Its oxygen-concentration dependence. *J. Magn. Magn. Mater.*, 156:311–314, 1996.

[45] J. Inoue and S. Maekawa. Theory of tunneling magnetoresistance in granular magnetic films. *Phys. Rev. B*, 53(18):R11 927–R11 929, 1996.

[46] J.-H. Park, E. Vescovo, H.-J. Kim, C. Kwon, R. Ramesh, and T. Venkatesan. Magnetic Properties at Surface Boundary of a Half-Metallic Ferromagnet $La_{0.7}Sr_{0.3}MnO_3$. *Phys. Rev. Lett.*, 81(9):1953–1956, 1998.

[47] M. Holdenried, B. Hackenbroich, and H. Micklitz. Systematic studies of tunneling magnetoresistance in granular films made from well-defined Co clusters. *J. Magn. Magn. Mater.*, 231:L13–L19, 2001.

[48] Turbobeads Llc. http://www.turbobeads.com/. Accessed: 2013-04-24.

[49] R. N. Grass and W. J. Stark. Gas phase synthesis of fcc-cobalt nanoparticles. *J. Mater. Chem.*, 16:1825–1830, 2006.

[50] R. N. Grass, E. K. Athanassiou, and W. J. Stark. Covalently Functionalized Cobalt Nanoparticles as a Platform for Magnetic Separations in Organic Synthesis. *Angew. Chem. Int. Ed.*, 46:4909–4912, 2007.

[51] F. Heusler. *Verh. Dt. Phys. Ges.*, 5:219, 1903.

[52] T. Graf, C. Felser, and S. S. P. Parkin. Simple rules for the understanding of Heusler compounds. *Prog. in Solid State Chem.*, 39:1–50, 2011.

[53] R. A. de Groot, F. M. Mueller, P. G. van Engen, and K. H. J. Buschow. New Class of Materials: Half-Metallic Ferromagnets. *Phys. Rev. Lett.*, 50(25):2024–2027, 1983.

[54] B. Balke, S. Wurmehl, G. H. Fecher, C. Felser, and J. Kübler. Rational design of new materials for spintronics: Co_2FeZ (Z = Al, Ga, Si, Ge). *J. Sci. Technol. Adv. Mater.*, 9:014102, 2008.

[55] S. Trudel, O. Gaier, J. Hamrle, and B. Hillebrands. Magnetic anisotropy, exchange and damping in cobalt-based full-Heusler compounds: an experimental review. *J. Phys. D: Appl. Phys.*, 43:193001, 2010.

[56] C. H. Wang, Y. Z. Guo, F. Casper, B. Balke, G. H. Fecher, C. Felser, and Y. Hwu. Size correlated long and short range of ternary co_2fega heusler nanoparticles. *Appl. Phys. Lett.*, 97:103106, 2010.

[57] L. Basit et al. Heusler compounds as ternary inter metallic nanoparticles: Co_2FeGa. *J. Phys. D: Appl. Phys.*, 42:084018, 2009.

[58] C. Wang et al. Probing the Size Effect of $Co_2FeGa-SiO_2@C$ Nanocomposite Particles Prepared by a Chemical Approach. *Chem. Mater.*, 22:6575–6582, 2010.

[59] particles prepared by C. Wang, Johannes Gutenberg-Universität Mainz, 2011.

[60] C. Wang. *A chemical approach to Heusler compounds and nanoparticles*. PhD thesis, Johannes Gutenberg-Universität Mainz, 2001.

[61] K. H. J. Buschow and P. G. van Engen. Magnetic and magneto-optical properties of heusler alloys based on aluminium and gallium. *J. Magn. Magn. Mater.*, 25:90–96, 1981.

[62] T. Graham. Drei Abhandlungen über Dialyse (Kolloide). In *Ostwald's Klassiker der exakten Wissenschaften*, volume 179. Verlag von Wilhelm Engelmann, Leipzig, 1911.

[63] H.-D. Dörfler. *Grenzflächen und kolloid-disperse Systeme*. Springer, 2002.

[64] S. Sakka. *Handbook of sol-gel science and technology - Processing characterizations and applications*. Kluwer Academic Publishers, 2005.

[65] gel prepared by C. Müller, FH Bielefeld, 2012.

[66] C. Müller, K. Kraushaar, A. Doebbe, J. H. Mussgnugc, O. Kruse, E. Kroke, and A. Patel. Synthesis of transparent aminosilane-derived silica based networks for entrapment of sensitive materials. *Chem. Commun.*, 49:10163, 2013.

[67] C. Müller, M. Hanitzsch, K. Kraushaar, E. Kroke, and A. Patel. Development of novel transparent silica gel and "glass". Poster at 6th European Silicon Days Conference, France, 2012.

[68] C. Wiltzsch, J. Wagler, G. Roewer, and E. Kroke. Sol-gel analogous aminolysis-ammonolysis of chlorosilanes to chlorine-free Si/(C)/N-materials. *Dalton Trans.*, 28:5474–5477, 2009.

[69] CV-TRONIC Elektrodengel. https://shop.apotal.de/. Accessed: 2013-05-07.

[70] Dow Glycerine. online, 2013. physical properties.

[71] P. Gemeiner, L. Rexová-Benková, F. Švec, and O. Norrlöw. Natural and Synthetic Carriers Suitable for Immobilization of Viable Cells, Active Organelles, and Molecules. In *Immobilized Biosystems - Theory and Practical Applications*. Blackie Academic and Professional, 1994.

[72] A. Haug and O. Smidsrød. Strontium-calcium selectivity of alginates. *Nature*, 215:757, 1967.

[73] O. Smidsrød and K. I. Draget. Alginate gelation technologies. In *Food Colloids - Proteins, Lipids and Polysaccharides*, pages 279–293. The Royal Soc. of Chem., 1996.

[74] Ý. A. Mørah. *Novel Alginate Microcapsules for Cell Therapy - A study of the structure-function relationships in native and structurally engineered alginates*. PhD thesis, Norwegian University of Science and Technology, Trondheim, 2008.

[75] K. Frühauf. *Evaluierung von temperaturrelevanten Parametern zur lokalen Erwärmung von Geweben mittels magnetischer Thermoablation*. PhD thesis, Friedrich-Schiller-Universität Jena, 2001.

[76] http://commons.wikimedia.org/wiki/File:Agarose_polymere.svg. Accessed: 2013-10-28.

[77] Alginic aced sodium salt from brown algae datasheet. http://www.sigmaaldrich.com/catalog/product/sigma/a0682?lang=de&region=DE. Accessed: 2013-04-30.

[78] TRIS Acetate-EDTA buffer datasheet. http://www.sigmaaldrich.com/catalog/product/sigma/t4038?lang=de&region=DE. Accessed: 2013-04-30.

[79] Agarose datasheet. http://www.sigmaaldrich.com/catalog/product/sial/a47-18?lang=de&region=DE. Accessed: 2013-04-30.

[80] http://corporate.zeiss.com/corporate/de/home.html. online. Accessed: 2013-04-30.

[81] http://www.raith.com/. online. Accessed: 2013-04-30.

[82] C. Albon. *Integration of tunneling magnetoresistive sensors for high resolutive magnetic particle detection*. PhD thesis, Bielefeld University, 2009.

[83] http://allresist.de. online. Accessed: 2013-07-15.

[84] http://www.oerlikon.com/leyboldvacuum/. online. Accessed: 2013-07-15.

[85] N. Yao. *Focused Ion Beam Systems*. Cambridge University Press, 2007.

[86] W. R. McKenzie, E. A. Marquis, and P. R. Munroe. Focused ion beam sample preparation for atom probe tomography. *Microscopy: Science, Technology, Applications and Education*, 3:1080–1810, 2010.

[87] AGM. http://www.princetonmeasurements.com/agmfeata.htm. Accessed: 2013-11-18.

[88] J. Meyer, T. Rempel, F. Wittbracht, C. Müller, A. V. Patel, and A. Hütten. Giant magnetoresistance effects in gel-like matrices. *Smart Mater. Struct.*, 22:025032, 2013.

[89] C. L. Chien. Giant magneto-transport phenomena in granular magnetic systems. *Mat. Sci. Eng.*, B31:127–131, 1995.

[90] S. S. P. Parkin, Li. Z. G., and D. J. Smith. Giant magnetoresistance in antiferromagnetic Co/Cu multilayers. *Appl. Phys. Lett.*, 58:2710, 1991.

[91] R. Schad, C. D. Potter, P. Beliën, G. Verbanck, and V. V. Moshchalkov et al. Giant magnetoresistance in Fe/Cr superlattices with very thin Fe layers. *Appl. Phys. Lett.*, 64:3500, 1994.

[92] P. Allia, M. Knobel, P. Tiberto, and F. Vinai. Magnetic properties and giant magnetoresistance of melt-spun granular $Cu_{100-x} - Co_x$. *Phys. Rev. B*, 52(21):15398–15411, 1995.

[93] Y. J. Chen, J. Ding, L. Si, W. Y. Cheung, S. P. Wong, I. H. Wilson, and T. Suzuki. Magnetic domain structures and magnetotransport properties in Co?Ag granular thin films. *Appl. Phys. A*, 73:103–106, 2001.

[94] F. Wittbracht, A. Weddemann, B. Eickenberg, and A. Hütten. On the direct employment of dipolar particle interaction in microfluidic systems. *Microfluid. Nanofluid.*, 13:543–554, 2012.

[95] D. Kechrakos and K. N. Trohidou. Interplay of dipolar interactions and grain-size distribution in the giant magnetoresistance of granular metals. *Phys. Rev. B*, 62:3941–3951, 2000.

[96] private communication Andreas Hütten, 2013.

[97] R. C. O'Handley. *Modern magnetic materials: principles and applications*. Wiley & Sons, United States of America, 2000.

[98] M. Hashimoto, J. Herfort, H.-P. Schnherr, and K. H. Ploog. Epitaxial Heusler alloy Co_2FeSi/GaAs(001) hybrid structures. *Appl. Phys. Lett.*, 87:102506, 2005.

[99] A. Hütten, D. Sudfeld, K. Wojczykowski, P. Jutzi, and G. Reiss. Giant magnetoresistance and magnetic aspects in granular structures. *JMMM*, 262:23, 2003.

[100] M. B. Stearns and Y. Cheng. Determination of para and ferromagnetic components of magnetization and magnetoresistance of granular Co/Ag films. *J. Appl. Phys.*, 75:6894, 1994.

[101] D. J. Sellmyer, C. P. Luo, and Y. Qiang. *Handbook of thin film devices magnetic, 5, nanomaterials and magnetic thin films*, volume 37.

[102] C. L. Chien, J. Q. Xiao, and J. S. Jiang. Giant negative magnetoresistance in granular ferromagnetic systems (invited). *J. Appl. Phys.*, 73:5309, 1993.

[103] A. Weddemann et al. Review and outlook: from single nanoparticles to self-assembled monolayers and granular GMR sensors. *Beilstein J. Nanotechnol.*, 1:75–93, 2010.

[104] E. Raphael, O. A. César, B. Manzolli, and A. Pawlicka. Agar-based films for application as polymer electrolytes. *Electrochim. Acta*, 55:1455–1459, 2010.

[105] R. I. Mattos, C. Tambelli, J. P. DOnoso, and A. Pawlicka. NMR study of starch based polymer gel electrolytes: Humidity effects. *Electrochim. Acta*, 53:1461–1465, 2007.

[106] F. Wittbracht. *Interaction of magnetic beads in microfluidic systems: fundamentals and applications*. PhD thesis, Bielefeld University, 2012.

[107] I. Ennen et al. From Magnetic Nanoparticles to Magnetoresistive Biosensors. *Acta Phys. Pol. A*, 121(2):420–425, 2012.

[108] J.O'M Bockris and A. K. N. Reddy. *Modern Electrochemistry*, volume 2. Plenum Press, New York, 1970.

[109] N. G. Green, A. Ramos, González, H. Morgan, and A. Castellanos. Fluid flow induced by nonuniform ac electric fields in electrolytes on microelectrodes. III. Observation of streamlines and numerical simulation. *Phys. Rev. E*, 66:026305, 2002.

[110] M. Faiz. *Specialty Polymers - Materials and Applications*. I. K. International Publishing House Pvt. Ltd., 2007.

[111] A. J. Bard and L-R. Faulkner. *Electrochemical Methods - Fundamentals and Applications*. Wiley, 2001.

[112] N. Sato. Discharge current induced by the motion of charged particles. *J. Phys. D: Appl. Phys.*, 13:L3–6, 1980.

[113] G. P. Pandey, Y. Kumar, and S. A. Hashmi. Ionic liquid incorporated polymer electrolytes for supercapacitor application. *Indian Journal of Chemistry*, 49A:743–751, 2010.

[114] R. Morrow, D. R. McKenzie, and M. M. M. Bilek. The time-dependent development of electric double-layers in saline solutions. *J. Phys. D: Appl. Phys.*, 39:937–943, 2006.

[115] N. G. Green, A. Ramos, González, H. Morgan, and A. Castellanos. Fluid flow induced by nonuniform ac electric fields in electrolytes on microelectrodes. I. Observation of streamlines and numerical simulation. *Phys. Rev. E*, 61(4):4011, 2000.

[116] S.. S. Alias and A. A. Mohamad. Effect of NH_4I and I_2 concentration on agar gel polymer electrolyte properties for a dye-sensitized solar cell. *Ionics*, 19:1185–1194, 2013.

[117] M. L. H. Rozali, A. S. Samsudin, and M. I. N. Isa. Ion Conducting Mechanism of Carboxy Methylcellulose Doped With Ionic Dopant Salicylic Acid Based Solid Polymer Electrolytes. *Int. J. Appl. Sc. Technol.*, 2(4):113–121, 2012.

[118] N. H. Zainol, S. M. Samin, L. Othman, K. B. Md Isa, W. G. Chong, and Z. Osman. Magnesium Ion-Based Gel Polymer Electrolytes: Ionic Conduction and Infrared Spectroscopy Studies. *Int. J. Electrochem. Sci.*, 8:3602–3614, 2013.

[119] B. Ganesh, D. Kalpana, and N. G. Renganathan. Acrylamide based proton conducting polymer gel electrolyte for electric double layer capacitors. *Ionics*, 14:339–343, 2008.

[120] S.-Y. Lin, C.-M. Wang, P.-T. Hsieh, Y.-C. Chen, C.-C. Liu, and S.-C. Shih. A novel gel polymer electrolyte based on lithium salt with an ethyl cellulose. *Colloid Polym. Sci.*, 287:1355–1358, 2009.

[121] A. Pawlicka, R. I. Mattos, J. F. Lima, C. E. Tambelli, C. J. Magon, and J. P. Donoso. Magnetic resonance and conductivity study of a gelatin-based polymer gel electrolyte. *Electrochim. Acta*, 57:187–191, 2011.

[122] H. Vogel. *Z. Phys.*, 22:645, 1922.

[123] V. G. Tammann and H. G. Hesse. *Anorg. Allg. Chem.*, 19:245, 1926.

[124] G. S. Fulcher. *J. Am. Ceram. Soc.*, 8:339, 1925.

[125] J. Jiang, D. Gao, Z. Li, and G. Su. *Reactive & Functional Polymers*, 66:1141–1148, 2006.

[126] J.O'M Bockris and A. K. N. Reddy. *Modern Electrochemistry*, volume 1. Plenum Press, New York, 1970.

[127] A. R. Blythe. *Electrical properties of polymers*. Cambridge University Press, 1979.

[128] J. Meyer, M. Schäfer, T. Rempel, and A. Hütten. AC-granular magnetoresistance effects in systems with organic matrices. In NSTI, editor, *Tech Connect World 2013 Proceedings*, volume 1, page 699. CRC Press, 2013.

[129] W. Rehwald, H. Kiess, and B. Binggeli. Frequency Dependent Conductivity in Polymers and Other Disordered Materials. *Z. Phys. B - Condensed Matter*, 68:143–148, 1987.

[130] A. N. Papathanassiou, I. Sakellis, and J. Grammatikakis. Universal frequency-dependent ac conductivity of conducting polymer networks. *Appl. Phys. Lett.*, 91:122911, 2007.

[131] N. Chand and D. Jain. Evaluation of a.c. conductivity behaviour of graphite filled polysulphide modified epoxy composites. *Bull. Mater. Sci.*, 27(3):227233, 2004.

[132] A. K. Jonscher. The 'universal' dielectric response. *Nature*, 267:673, 1977.

[133] A. K. Jonscher. A new understanding of the dielectric relaxation of solids. *J. Mater. Sci.*, 16:2037, 1981.

[134] A. Weddemann, J. Meyer, and A. Hütten. Numerical Study of Nanoscaled Granular Giant Magnetoresistance Sensors for the Limit Case of Dipolar Coupled Nanoparticles. *JBAP*, 2:60–67, 2013.

[135] A. Hütten, D. Sudfeld, I. Ennen, G. Reiss, W. Hachmann, U. Heinzmann, P. Wojczykowski, K. Nad Jutzi, W. Saikaly, and G. Thomas. New magnetic nanoparticles for biotechnology. *J. Biotech*, 112:47–63, 2004.

[136] L. Lagae, R. Wirix-Speetjens, J. Das, D. Graham, H. Ferreira, P. P. P. Freitas, G. Borghs, and J. de Boeck. On-chip manipulation and magnetization assessment of magnetic bead ensembles by integrated spin-valve sensors. *J. Appl. Phys.*, 91:7445–7447, 2002.

[137] A. Weddemann, F. Wittbracht, A. Auge, and A. Hütten. A hydrodynamic switch: Microfluidic separation system for magnetic beads. *Appl. Phys. Lett.*, 94:173501:1–173501:3, 2009.

[138] A. Weddemann, F. Wittbracht, A. Auge, and A. Hütten. Positioning system for particles in microfluidic structures. *Microfluid. Nanofluidics*, 7:849–855, 2009.

[139] M. Wiklund, S. Radel, and J. J. Hawkes. Acoustofluidics 21: Ultrasound-enhanced immunoassays and particle sensors. *Lab Chip*, 13:25–39, 2013.

[140] B. Eickenberg, J. Meyer, L. Helmich, D. Kappe, A. Auge, A. Weddemann, F. Wittbracht, and A. Hütten. Lab-on-a-Chip Magneto-Immunoassays: How to Ensure Contact between Superparamagnetic Beads and the Sensor Surface. *Biosensors*, 3:327–340, 2013.

[141] D. Makarov, D. Karnaushenko, and O. Schmidt. Printable Magnetoelectronics. *ChemPhysChem*, 14:1771–1776, 2013.

[142] M. Johnson and S. Silsbee. Interfacial Charge-Spin Coupling: Injection and Detection of Spin Magnetization in Metals. *Phys. Rev. Lett.*, 55(17):1790, 1985.

[143] W. P. Pratt, S.-F. Lee, J. M. Slaughter, R. Loloee, P. A. Schroeder, and J. Bass. Perpendicular Giant Magnetoresistances of Ag/Co Multilayers. *Phys. Rev. Lett.*, 66(23):3060–3063, 1991.

[144] F. J. Jedema, A. T. Filip, and B. J. van Wees. Electrical spin injection and accumulation at room temperature in an all-metal mesoscopic spin valve. *Nature (London)*, 410:345, 2001.

[145] T. Kimura, T. Sato, and Y. Otani. Temperature Evolution of Spin Relaxation in a NiFe/Cu Lateral Spin Valve. *Phys. Rev. Lett.*, 100:066602, 2008.

[146] Y. Ji, A. Hoffmann, J. E. Pearson, and S. D. Bader. Enhanced spin injection polarization in Co/Cu/Co nonlocal lateral spin valves. *Appl. Phys. Lett.*, 88:052509, 2006.

[147] Y. Ji, J. S. Jiang, and S. D. Bader. Spin injection, diffusion, and detection in lateral spin-valves. *Appl. Phys. Lett.*, 85:6218, 2004.

[148] X. J. Wang, H. Zou, L. E. Ocola, and Y. Ji. High spin injection polarization at an elevated dc bias in tunnel-junction-based lateral spin valves. *Appl. Phys. Lett.*, 95:022519, 2009.

[149] A. Vogel, J. Wulfhorst, and G. Meier. Enhanced spin injection and detection in spin valves with integrated tunnel barriers. *Appl. Phys. Lett.*, 94:122510, 2009.

[150] K. Ohnishi, T. Kimura, and Y. Otani. Nonlocal injection of spin current into a superconducting Nb wire. *Appl. Phys. Lett.*, 96:192509, 2010.

[151] L. Piraux, S. Dubois, and A. Fert. Perpendicular giant magnetoresistance in magnetic multilayered nanowires. *J. Magn. Magn. Mater.*, 159:L287, 1996.

[152] L. Piraux, S. Dubois, A. Fert, and L. Belliard. The temperature dependence of the perpendicular giant magnetoresistance in Co/Cu multilayered nanowires. *Eur. Phys. J. B*, 4:413–420, 1998.

[153] P. A. Bobbert, W. Wagemans, F. W. A. van Oost, B. Koopsmans, and M. Wohlgenannt. Theory for Spin Diffusion in Disordered Organic Semiconductors. *Phys. Rev. Lett.*, 102:156604, 2009.

[154] M. Wohlgenannt. Organic magnetoresistance and spin diffusion in organic semiconductor thin film devices. *Phys. Status Solidi RRL*, 6:229–242, 2012.

[155] Y. Ji, A. Hoffmann, J. S. Jiang, J. E. Pearson, and S. D. Bader. Non-local spin injection in lateral spin valves. *J. Phys. D: Appl. Phys.*, 40:1280–1284, 2007.

Danksagung

An dieser Stelle möchte ich mich bei all den Menschen bedanken, die zum Gelingen dieser Doktorarbeit beigetragen haben.
An erster Stelle gilt mein Dank Prof. Dr. Andreas Hütten, dafür, dass er mich so herzlich in seiner Arbeitsgruppe aufgenommen und mir die Möglichkeit zu dieser interessanten Doktorarbeit auf einem mir damals neuen Fachgebiet gegeben hat. Ich danke ihm für sein Vertrauen, dafür, dass er mir im gesamten Prozess dieser Arbeit jederzeit für Diskussionen jeglicher Art zur Verfügung stand, für das Beisteuern kreativer Ideen sowie für seine fortwährende Unterstützung und Motivation.
Desweiteren gilt mein Dank Prof. Dr. Thomas Huser, der sich für die Erstellung des Zweitgutachtens bereit erklärt hat.
Ich danke Prof. Dr. Günter Reiss für wertvolle Diskussionen, für die er sich stets Zeit genommen hat.
Ganz herzlich bedanken möchte ich mich auch bei Dr. Karsten Rott für fachliche Beratung und technischen Support im Labor, allen voran bei Fragen bezüglich des REMs und der Lithographie.
Ich danke Dr. Camelia Albon und Peter Hedwig dafür, dass sie mir den Einstieg in das neue Arbeitsgebiet erleichtert haben, insbesondere Camelia für die Einweisungen in den Laboren.
Großer Dank gebührt meinen Bürokollegen Markus Schäfers und Dr. Frank Wittbracht, die entscheidend dazu beigetragen haben, dass ich mich von Anfang an sehr wohl in der neuen Umgebung gefühlt habe. Vielen Dank für die vielen wichtigen Gespräche sowie für das sorgfältige Korrekturlesen dieser Arbeit.
Auch Dr. Alexander Weddemann danke ich für seine Unterstützung, Anregungen und Vorschläge.
Für sein stets offenes Ohr bei kleineren und größeren Problemen möchte ich Niclas Teichert danken.
Thomas Rempel danke ich insbesondere für den Beitrag experimenteller Ergebnisse hinsichtlich der Partikel Superstrukturen in Agarosegelen im Rahmen seiner Masterarbeit.
Ich danke Dieter Akemeier und Annalena Wolff für die Aufnahmen und Hilfe an der FIB und Nadine Mill für die freundliche und kompetente Unterstützung im Chemielabor.
Ebenso gilt mein Dank Christiane Müller von der FH Bielefeld für die Herstellung der Silizium basierten Gele und C. Wang von der Johannes Gutenberg-Universität Mainz für die Herstellung der Heusler Nanopartikel.

Für die immer sehr freundliche Hilfe bei sämtlichen Verwaltungsfragen danke ich Aggi Windmann.
Herzlicher Dank geht an alle - auch an die nicht namentlich erwähnten - Kollegen auf D2, für eine sehr angenehme und kollegiale Arbeitsatmosphäre, die dazu beigetragen hat, dass mir meine Zeit hier in sehr schöner Erinnerung bleiben wird.
Zu guter Letzt gilt ganz besonderer Dank meinen Eltern für ihre unermüdliche Unterstützung und ihren Zuspruch sowie meinem Freund Lothar für sein kontinuierliches Interesse an meiner Arbeit, sein Verständnis, und dafür, dass er mich in schwierigen Situationen durch seinen Optimismus aufgemuntert und mir Mut gemacht hat.